

# Chapter 1

## Introduction

### 1.1 Introduction to low dimensional systems

During the past decade semiconductor-based low dimensional structures have become crucial model systems in the investigation of electrical conduction on the short length scales. The unprecedented purity and the crystalline perfection of semiconductor materials lead to the availability of the thin layer structures with high electron mobility. Such layer structure, called two dimensional electron gases (2DEG), could be formed in Si-inversion layers or heterostructure semiconductors, where only the motion of electrons along the plane of thin layer is allowed. Contrary to the thin metal films, the desired properties are found in semiconductor-based 2DEG, e.g. tunable electron density by electric field, large Fermi wave length ( $\sim 40$  nm) and large mean free path ( $\sim 10 \mu\text{m}$ ). Thus, the studies of the quantum transport could be easily arrived.

The phase coherence properties of quantum mechanical particles are the characteristics of a microscopic object. The possibility of the coherent length is hold up to several microns, which is classified as macroscopic regime. The physics of such systems are called mesoscopic physics. Quasi-one dimensional configurations can be readily realized by the lateral confinement on 2DEG.

The unique regime of the mesoscopic conductors is the ballistic regime, where the impurity scattering can be neglect. Similar to the transport in waveguides, the various transmission properties of transport are arrived by varying the geometries of the conductors. The discreteness of the propagating modes shown in Landauer-Büttiker

formula relates the conduction to the transmission. The physics of this regime could be called electron optics in the solid states. [1]

The macroscopic behavior can not be observed as large as 2.5 mm in the quantum Hall regime. A magnetic field perpendicularly applied to 2DEG results in the quantization of the energy in a series of Landau levels. A remarkable feature of this regime is the quantized Hall resistance. [2] The magnetic length  $\sqrt{\hbar/eB}$  ( $\sim 10\text{nm}$  at  $B=5\text{T}$ ) thus takes the role of the wavelength. Electron would transport adiabatically as the potential landscape is adjusted smoothly to the scale of the magnetic length.

In this thesis, the studies of several low dimensional systems are shown. The motivation is not just because of the scientific interest. The decreasing scales of fabrication of conventional transistors lead to the break down of the theory based on the classical diffusive transport. The exploration of the novel transport regime in semiconductor nanostructures provides the development of the innovative future devices. In literature, some ambitious proposals envision the entire computers composed of arrays of quantum interference devices. [3]

## 1.2 Motivation

Phase coherence in solid state conductors is a property of fundamental interest. The prospect of solid state quantum information has also put the focus on possible applications based on phase coherence. With the advent of mesoscopic physics, it has become possible to experimentally investigate quantum phase coherent properties of electrons in solid state conductors in a controlled way. [4] In particular, in ballistic mesoscopic samples at low temperatures, electrons can propagate up to several microns

without losing phase information. This opens up the possibility to investigate electrical analogs of various optical phenomena and experiments. An investigation of such analogs is of fundamental interest. On the one hand, it allows one to establish similarities between the properties of photons and conduction electrons, a consequence of the wave nature of the quantum particles. On the other hand, it also allows one to investigate the differences between the two types of particles arising from the different quantum statistical properties of fermions and bosons. For many-particle properties, such as light intensity correlations or correspondingly electrical current correlations, noise, the quantum statistical properties are important. [5, 6] Both the wave-nature of the particles as well as their quantum statistics are displayed in a clearcut fashion in interferometer structures. In the first part of this thesis, we are concerned with the electrical analogs of two well known optical interferometers, the single-particle Mach-Zehnder (MZ) interferometer and the two-particle Hanbury Brown Twiss (HBT) interferometer.

The MZ-interferometer is a subject of most textbooks in optics. [7] In the framework of quantum optics, considering individual photons rather than classical beams of light, the interference arises due to the superposition of the amplitudes for two different possible paths of a single photon. This leads to an interference term in the light intensity. The MZ-interferometer is thus a prime example of a single particle interferometer. [8] The MZI experiments [9-11, 61] were all implemented in a conductor in the integer quantum Hall regime, where the electrons propagate along unidirectional, quantum mechanical edge states and quantum point contacts (QPCs) act as beam splitters. In the experiments [9-11, 61] the visibility of the conductance oscillations as a function of flux  $\Phi$  were reduced below the ideal value, a signature of dephasing of the electrons propagating along the edges. Dephasing in the MZI was investigated in several theoretical works. Originally, Seelig and Büttiker [12]

investigated the effect of dephasing on the conductance oscillations due to Nyquist noise. Following the experiment in Ref. [9], where also the shot noise was measured, a number of works investigated the effect of dephasing on the current and the noise. The dephasing was introduced via fluctuating classical potentials [13-15] and by coupling the MZI to a quantum bath [16] as well as to a voltage probe. [13, 14, 17] Recently these studies were extended to the full distribution of the transferred charge, both for a fluctuating classical potential [15] as well as a voltage probe [18, 19] as a source of dephasing.

Taken together, these theoretical investigations have provided a qualitative picture of the effect of dephasing on transport properties in the MZI. The experimental situation is however not conclusive. In the very recent work by Litvin *et al.* [11] the observed temperature and voltage dependence of the visibility of the conductance oscillations are in good agreement with the noninteracting theory of Ref. [17]. In particular, the effect of the interferometer arm asymmetry is clearly manifested. The overall visibility is however low, a couple of percent. In contrast, in the recent work by Neder *et al.* [10] and Roulleau *et al.* [61] the visibility is high, but the voltage dependence of the conductance visibility was found to be insensitive to arm asymmetry, however showing a clear lobe structure. A possible explanation for the findings of Ref. [10] was also suggested, invoking interactions between electrons at different edge states. [20] The experimental situation thus motivates further investigations of the coherent transport properties of the MZI.

The HBT-interferometer [21-23] was originally invented for stellar astronomy, to measure the angular diameter of stars. It is an intensity, or two-particle, [8] interferometer. The interference arises from the superposition of the amplitudes for two different two-particle processes. Importantly, there is no single particle interference in the HBT-interferometer. Consequently, in contrast to the MZ-interferometer there is no

interference in the light intensity, the interference instead appears in the intensity-intensity correlations. Moreover, the intensity-intensity correlations also display the effect of quantum statistics. Photons originating from thermal sources tend to bunch, giving rise to positive intensity cross correlations. For the electronic analog of the HBT-interferometer, it was the corresponding anti-bunching of electrons that originally attracted interest. It was predicted [5] that the electrical current cross correlations in mesoscopic conductors would be manifestly negative, i.e. display anti-bunching, as a consequence of the fermionic statistics of the electrons. Negative current cross correlations were subsequently observed in two independent experiments. [24, 25] Recently, anti-bunching for field emitted electrons in vacuum was also demonstrated. [26] The two-particle interference in the HBT-experiment has received much less attention. We emphasize that while the bunching of the photons was necessary for obtaining a finite, positive cross correlation signal, it was the two-particle effect that was of main importance to HBT since the angular diameter of the star was determined from the two-particle interference pattern. In electrical conductors, two-particle effects in AB-interferometers were investigated theoretically in Refs. [27-29]. Only very recently two of the authors and Sukhorukov [30] proposed a direct electronic analog of the optical HBT-interferometer which permits to demonstrate two-particle interference in an unambiguous way.

In the beginning of this thesis, we investigate and compare in detail the current and zero-frequency noise in electronic MZ and HBT interferometers.

Next, we propose to investigate the properties of the currents and the shot noises in a pump driven MZI. In contrast to previous work, both experimental and theoretical, all electronic reservoirs are kept at the same potential. The current is instead created via the quantum pump effect, [31-35] by varying periodically the transparencies of the two QPCs. Working in the adiabatic, low pump frequency limit, the system is kept

close to equilibrium. This minimizes the effect of inelastic dephasing and hence allows for a more detailed investigation of the coherence properties.

Theoretically, a large number of investigations of various aspects of quantum pumping have been carried out, a representative collection can be found in Refs. [31-50]. However, only a few experiments aimed at investigating quantum pumping of electrical currents have been performed. [51, 52] In the MZI the current is a true quantum interference effect. In addition, the elementary structure of the MZI and the fact that the potential applied at the QPC control both the pump effect and the scattering properties of the QPCs makes the MZI a promising candidate for a quantum pump. Previous studies of pumping in mesoscopic interferometers have concerned Aharonov-Bohm, [45, 53, 54] double slit-quantum dot [44] and two-particle [55] interferometers, however, to the best of our knowledge, not MZIs.

Original proposal of QCP, in the adiabatic regime, was due to Thouless. [31] He considered the current generated by a slowly varying traveling wave in an isolated one-dimensional system. The number of electrons transported per period was found to be quantized if the Fermi energy lies in a gap of the spectrum of the instantaneous Hamiltonian. Aiming at this quantized pumped charge nature of the adiabatic pumping, Niu proposed various one-dimensional periodic potentials for the adiabatic quantum pumping (AQP), [49] and pointed out the importance of the quantized charge pumping in utilizing it for a direct-current standard. [49]

An experimental effort in generating AQP involves surface acoustic wave (SAW). [56-60] Generated by an interdigitated SAW transducer located deep on an end-region of a narrow channel, the SAW propagates to the other end-region of the narrow channel while inducing a wave of electrostatic potential inside the channel. Electrons trapped in the potential minima are thus transported along the narrow channel. Both Mott-Hubbard electron-electron repulsion in each such trap and the adiabaticity in the

transport are needed to give rise to quantization in the pumped current. [57] As such, the channel has to be operated in the pinch-off regime. [58]

In the last part of this thesis, we propose to study another experimental configuration for QCP in a narrow channel. The proposed configuration consists of a pair of *finite* finger gate array (FGA), with the number  $N$  of finger gates (FG's) in each FGA being kept to a small number. In contrast to the SAW configuration, the FGA pair sits on top of the narrow channel, rather than locating at a distance far away from it; and the most significant QCP occurs in regimes other than the pinch-off regime. Pumping potential can be generated by ac biasing the FGA pairs with the same frequency but maintaining a phase difference  $\phi$  between them. Since the wave of electrostatic potential induced in the narrow channel is directly from the FG's, rather than via the SAW, our proposed structure has the obvious advantage that the working frequency is not restricted to the frequency of the SAW,  $\omega_S = 2\pi v_S/d$ . Here  $v_S$  is the phase velocity of the SAW, and  $d$  is the pitch in the FGA. Furthermore, when the working frequency is different from  $\omega_S$ , the contribution from SAW to the pumped current will be negligible. As the number of the FG's larger than two, the dominated mechanism is due to the time-dependent Bragg reflection, not the photon-assisted interferences.

### 1.3 Thesis Outline

The outline of the thesis is as follows.

Chapter 1 introduces the low dimensional systems, their applications and the motivation of this thesis.

Chapter 2 is shown the analysis and the comparison of the voltage driven electronic MZ and HBT interferometers in detail. The characteristics of currents and the shot noises are studied as a function of the voltage, the temperature and the dephasing rate.

Chapter 3 presents the investigation of the quantum pump driven electronic MZ interferometers. Instead of the conventional driving source, the quantum pumping effects are used to drive the electronic MZ interferometer. The pumped currents and the shot noises are studied subject to the pump frequency, the temperature and the effects of decoherence.

Chapter 4 shows another experimental achievable configuration, a finger gate array pump. The arrays of the time-dependent oscillations of gate potentials generate the pump currents which are related to the mechanism of the time dependent Bragg reflection. In contrast, for a pump modulated by two gates the mechanism is as a result of the photon-assisted interferences.

In Chapter 5, we make the conclusions of the thesis.



## References

- [1] H. van Houten and C.W.J. Beenakker, in *Analogies in Optics and Microelectronics* (W. van Haeringen and D. Lenstra, eds.). Kluwer Academic, Dordrecht, 1990.
- [2] K. von Klitzing, G. Dorda and M. Pepper, “New method for high-accuracy determination of the fine-structure constant based on quantized resistance,” *Phys. Rev. Lett.*, vol. 45, pp. 494–497, Aug. 1980.
- [3] R. T. Bate, *Sci. Am.*, vol. 258, pp. 78, 1988.
- [4] C.W.J. Beenakker and H. van Houten, “Quantum transport in semiconductor nanostructures,” *Solid State Physics*, vol. 44, pp. 1–228, 1991.
- [5] M. Büttiker, “Scattering theory of current and intensity noise correlations in conductors and wave guides,” *Phys. Rev. B*, vol. 46, pp. 12485–12507, Nov. 1992.
- [6] Ya. M. Blanter and M. Büttiker, “Shot noise in mesoscopic conductors,” *Phys. Rep.*, vol. 336, pp. 1–166, Sep. 2000.
- [7] M. Born and E. Wolf, *Principles of Optics*, 7th ed. (Cambridge University press, UK, 1999).
- [8] L. Mandel, “Quantum effects in one-photon and two-photon interference,” *Rev. Mod. Phys.*, vol. 71, pp. S274–S282, Mar. 1999.
- [9] Y. Ji, Y. Chung, D. Sprinzak, M. Heiblum, D. Mahalu, and H. Shtrikman, “An electronic Mach–Zehnder interferometer,” *Nature*, vol. 422, pp. 415–418, Mar. 2003.
- [10] I. Neder, M. Heiblum, Y. Levinson, D. Mahalu, and V. Umansky, “Unexpected Behavior in a Two-Path Electron Interferometer,” *Phys. Rev. Lett.*, vol. 96, pp. 016804–016807, Jan. 2006.
- [11] L. V. Litvin, H.-P. Tranitz, W. Wegscheider, and C. Strunk, “Decoherence and

- single electron charging in an electronic Mach-Zehnder interferometer,” *Phys. Rev. B*, vol. 75, pp. 033315–033318, Jan. 2007.
- [12] G. Seelig and M. Büttiker, “Charge-fluctuation-induced dephasing in a gated mesoscopic interferometer,” *Phys. Rev. B*, vol. 64, pp. 245313–245325, Dec. 2001.
- [13] F. Marquardt and C. Bruder, “Influence of Dephasing on Shot Noise in an Electronic Mach-Zehnder Interferometer,” *Phys. Rev. Lett.*, vol. 92, pp. 56805–56808, Feb. 2004.
- [14] F. Marquardt and C. Bruder, “Effects of dephasing on shot noise in an electronic Mach-Zehnder interferometer,” *Phys. Rev. B*, vol. 70, pp. 125305–125320, Sep. 2004.
- [15] H. Förster, S. Pilgram, and M. Büttiker, “Decoherence and full counting statistics in a Mach-Zehnder interferometer,” *Phys. Rev. B*, vol. 72, pp. 075301–075310, Aug. 2005.
- [16] F. Marquardt, “Fermionic Mach-Zehnder interferometer subject to a quantum bath,” *Europhys. Lett.*, vol. 72, pp. 788–794, Dec. 2005.
- [17] V. S.-W. Chung, P. Samuelsson, and M. Büttiker, “Visibility of current and shot noise in electrical Mach-Zehnder and Hanbury Brown Twiss interferometers,” *Phys. Rev. B*, vol. 72, pp. 125320–125332, Sep. 2005.
- [18] S. Pilgram, P. Samuelsson, H. Förster, and M. Büttiker, “Full-Counting Statistics for Voltage and Dephasing Probes,” *Phys. Rev. Lett.*, vol. 97, pp. 066801–066804, Aug. 2006.
- [19] H. Förster, P. Samuelsson, S. Pilgram, and M. Büttiker, “Voltage and dephasing probes: a full counting statistics discussion,” cond-mat/0609544, Sep. 2006.
- [20] E.V. Sukhorukov and V.V. Cheianov, “Resonant dephasing of the electronic Mach-Zehnder interferometer,” cond-mat/0609288, Sep. 2006.

- [21] R. Hanbury Brown and R.Q. Twiss, *Philos. Mag. Ser.*, vol. 45, pp. 663, 1954.
- [22] R. Hanbury Brown and R.Q. Twiss, “Correlation between Photons in two Coherent Beams of Light,” *Nature (London)*, vol. 177, pp. 27–29, Jan. 1956.
- [23] R. Hanbury Brown and R.Q. Twiss, “A Test of a New Type of Stellar Interferometer on Sirius,” *Nature (London)*, vol. 178, pp. 1046–1048, Nov. 1956.
- [24] M. Henny, S. Oberholzer, C. Strunk, T. Heinzel, K. Ensslin, M. Holland and C. Schenberger, “The Fermionic Hanbury Brown and Twiss Experiment,” *Science*, vol. 284, pp. 296–298, Apr. 1999.
- [25] W.D. Oliver, J. Kim, R.C. Liu, and Y. Yamamoto, “Hanbury Brown and Twiss-Type Experiment with Electrons,” *Science*, vol. 284, pp. 299–301, Apr. 1999.
- [26] H. Kiesel, A. Renz, and F. Hasselbach, “Observation of Hanbury Brown–Twiss anticorrelations for free electrons,” *Nature (London)*, vol. 418, pp. 392–394, Jul. 2002.
- [27] M. Büttiker, “The quantum phase of flux correlations in waveguides,” *Physica B*, vol. 175, pp. 199–212, Dec. 1991.
- [28] M. Büttiker, “Flux-sensitive correlations of mutually incoherent quantum channels,” *Phys. Rev. Lett.*, vol. 68, pp. 843–846, Feb. 1992.
- [29] D. Loss and E.V. Sukhorukov, “Probing Entanglement and Nonlocality of Electrons in a Double-Dot via Transport and Noise,” *Phys. Rev. Lett.*, vol. 84, pp. 1035–1038, Jan. 2000.
- [30] P. Samuelsson, E.V. Sukhorukov, and M. Büttiker, “Two-Particle Aharonov-Bohm Effect and Entanglement in the Electronic Hanbury Brown–Twiss Setup,” *Phys. Rev. Lett.*, vol. 92, pp. 26805–26808, Jan. 2004.
- [31] D. J. Thouless, “Quantization of particle transport,” *Phys. Rev. B*, vol. 27, pp.

6083–6087, May 1983.

- [32] M. Büttiker, H. Thomas, and A. Prêtre, “Current partition in multiprobe conductors in the presence of slowly oscillating external potentials,” *Z. Phys. B: Condens. Matter*, vol. 94, pp. 133–137, Mar. 1994.
- [33] B. Spivak, F. Zhou, and M. T. Beal Monod, “Mesoscopic mechanisms of the photovoltaic effect and microwave absorption in granular metals,” *Phys. Rev. B*, vol. 51, pp. 13226–13230, May 1995.
- [34] P. W. Brouwer, “Scattering approach to parametric pumping,” *Phys. Rev. B*, vol. 58, pp. R10135–R10138, Oct. 1998.
- [35] F. Zhou, B. Spivak, and B. Altshuler, “Mesoscopic Mechanism of Adiabatic Charge Transport,” *Phys. Rev. Lett.*, vol. 82, pp. 608–611, Jan. 1999.
- [36] T. A. Shutenko, I. L. Aleiner, and B. L. Altshuler, “Mesoscopic fluctuations of adiabatic charge pumping in quantum dots,” *Phys. Rev. B*, vol. 61, pp. 10366–10375, Apr. 2000.
- [37] J. E. Avron, A. Elgart, G. M. Graf, and L. Sadun, “Geometry, statistics, and asymptotics of quantum pumps,” *Phys. Rev. B*, vol. 62, pp. R10618–R10621, Oct. 2000.
- [38] M. G. Vavilov, V. Ambegaokar, and I. L. Aleiner, “Charge pumping and photovoltaic effect in open quantum dots,” *Phys. Rev. B*, vol. 63, pp. 195313–195324, Apr. 2001.
- [39] B. Wang, J. Wang, and H. Guo, “Parametric pumping at finite frequency,” *Phys. Rev. B*, vol. 65, pp. 073306–073309, Jan. 2002.
- [40] M. Moskalets and M. Büttiker, “Dissipation and noise in adiabatic quantum pumps,” *Phys. Rev. B*, vol. 66, pp. 035306–035314, Jul. 2002.
- [41] M. L. Polianski and P. W. Brouwer, “Scattering matrix ensemble for time-dependent transport through a chaotic quantum dot,” *J. Phys. A: Math.*

- Gen.*, vol. 36, pp. 3215–3236, Mar. 2003.
- [42] J. E. Avron, A. Elgart, G. M. Graf, and L. Sadun, “Transport and Dissipation in Quantum Pumps,” *J. Stat. Phys.*, vol. 116, pp. 425–473, Aug. 2004.
- [43] M. Martinez-Mares, C. H. Lewenkopf, and E. R. Mucciolo, “Statistical fluctuations of pumping and rectification currents in quantum dots,” *Phys. Rev. B*, vol. 69, pp. 085301–085312, Feb. 2004.
- [44] H.-Q. Zhou, U. Lundin, S. Y. Cho, and R. H. McKenzie, “Measuring geometric phases of scattering states in nanoscale electronic devices,” *Phys. Rev. B*, vol. 69, pp. 113308–113311, Mar. 2004.
- [45] D. Shin and J. Hong, “Electron transport in the Aharonov-Bohm pump,” *Phys. Rev. B*, vol. 70, pp. 073301–073304, Aug. 2004.
- [46] S.W. Chung, C.S. Tang, C.S. Chu, and C.Y. Chang, “Finger-gate array quantum pumps: Pumping characteristics and mechanisms,” *Phys. Rev. B*, vol. 70, pp. 085315–085321, Aug. 2004.
- [47] M. Governale, F. Taddei, R. Fazio and F.W.J. Hekking, “Adiabatic Pumping in a Superconductor-Normal-Superconductor Weak Link,” *Phys. Rev. Lett.*, vol. 95, pp. 256801–256804, Dec. 2005.
- [48] D. Cohen, T. Kottos, and H. Schanz, “Quantum pumping: The charge transported due to a translation of a scatterer,” *Phys. Rev. E*, vol. 71, pp. 035202(R)–035205(R), Mar. 2005.
- [49] Q. Niu, “Towards a quantum pump of electric charges,” *Phys. Rev. Lett.*, vol. 64, pp. 1812–1815, Apr. 1990.
- [50] C. Benjamin, “Detecting a true quantum pump effect,” *Eur. Phys. J. B*, vol. 52, pp. 403–410, Jul. 2006.
- [51] M. Switkes, C. M. Marcus, K. Campman, and A. C. Gossard, “An Adiabatic Quantum Electron Pump,” *Science*, vol. 283, pp. 1905–1908, Mar. 1999.

- [52] L. DiCarlo, C.M. Marcus, and J.S. Harris, Jr, “Photocurrent, Rectification, and Magnetic Field Symmetry of Induced Current through Quantum Dots,” *Phys. Rev. Lett.*, vol. 91, pp. 246804–246807, Dec. 2003.
- [53] R. Citro and F. Romeo, “Pumping in a mesoscopic ring with Aharonov-Casher effect,” *Phys. Rev. B*, vol. 73, pp. 233304–233307, Jun. 2006.
- [54] S.K. Kim, K.K. Das, and A. Mizel, “Adiabatic quantum pumping in an Aharonov-Bohm loop and in a Si-like nanowire: interference in real space and in k-space,” cond-mat/0609601, Sep. 2006.
- [55] P. Samuelsson and M. Büttiker, “Dynamic generation of orbital quasiparticle entanglement in mesoscopic conductors,” *Phys. Rev. B*, vol. 71, pp. 245317–245321, Jun. 2005.
- [56] J. M. Shilton, V. I. Talyanskii, M. Pepper, D. A. Ritchie, J. E. F. Frost, C. J. B. Ford, C. G. Smith, and G. A. C. Jones, “High-frequency single-electron transport in a quasi-one-dimensional GaAs channel induced by surface acoustic waves,” *J. Phys.: Condens. Matter*, vol. 8, pp. L531–L540, Sep. 1996; J. M. Shilton, D. R. Mace, V. I. Talyanskii, Yu. Galperin, M. Y. Simmons, M. Pepper, and D. A. Ritchie, “On the acoustoelectric current in a one-dimensional channel,” *J. Phys.: Condens. Matter*, vol. 8, pp. L337–L344, Jun. 1996
- [57] V. I. Talyanskii, J. M. Shilton, M. Pepper, C. G. Smith, C. J. B. Ford, E. H. Linfield, D. A. Ritchie, and G. A. C. Jones, “Single-electron transport in a one-dimensional channel by high-frequency surface acoustic waves,” *Phys. Rev. B*, vol. 56, pp. 15180–15184, Dec. 1997.
- [58] Y. Levinson, O. Entin-Wohlman, P. Wölfle, “Acoustoelectric Current and Pumping in a Ballistic Quantum Point Contact,” *Phys. Rev. Lett.*, vol. 85, pp. 634–637, Jul. 2000.

- [59] O. Entin-Wohlman, Y. Levinson, P. Wölfle, “Acoustoelectric pumping through a ballistic point contact in the presence of magnetic fields,” *Phys. Rev. B*, vol. 64, pp. 195308–195314, Oct. 2001.
- [60] A. Aharony and O. Entin-Wohlman, “Quantized pumped charge due to surface acoustic waves in a one-dimensional channel,” *Phys. Rev. B*, vol. 65, pp. 241401(R)–241404(R), May 2002.
- [61] Preden Roulleau, F. Portier, D. C. Glattli, P. Roche G. Gaini, U. Gennser, D. Maily,” High visibility in an electronic Mach-Zehnder interferometer with random phase fluctuations,” cond-mat\0704.0746, April, 2007.

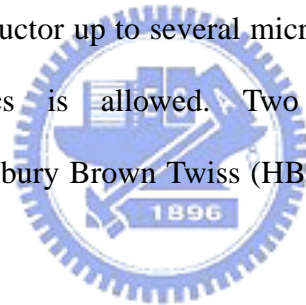


## Chapter 2

# Visibility of current and shot noise in electrical Mach-Zehnder and Hanbury Brown Twiss interferometers

### 2.1 Introduction of electrical Mach-Zehnder and Hanbury Brown Twiss interferometers

The progress of mesoscopic physics gives rise to the phase coherence length of electrons in a solid state conductor up to several microns. Thus, the possibility of the electrical analog of optics is allowed. Two well-known interferometers, Mach-Zehnder (MZ) and Hanbury Brown Twiss (HBT) interferometers, are explored in this chapter.



A schematic of the MZ-interferometer is shown in Fig. 2.1. An incident beam of light from source 1 is divided in two parts at the semitransparent beam splitter A. The two partial beams are reflected at mirrors and later joined at the second beam splitter B. Beams of light going out from B are detected in 3 and 4. The amplitude of the light in an outgoing beam is the sum of the amplitudes for the two partial beams,  $A = A_1 \exp(i\phi_1) + A_2 \exp(i\phi_2)$ . This gives an intensity  $|A|^2 = |A_1|^2 + |A_2|^2 + 2\text{Re}\{A_1 A_2^* \exp(i[\phi_1 - \phi_2])\}$ . The interference term  $2\text{Re}\{A_1 A_2^* \exp(i[\phi_1 - \phi_2])\}$  thus contains the difference between the geometrical phases,  $\phi_1 - \phi_2$ . Importantly, the four terminal geometry together with the reflectionless beam splitters lead to that the incident beam traverses the interferometer only once. This is a defining property of the MZ-interferometer.



We then turn to the electric analog of the MZ-interferometer, shown in Fig. 2.2. As pointed out in chapter 1, several results for the current and noise are available in the literature. [1-6] Here we analyze the most general situation possible, with finite voltage, temperature and interferometer arm asymmetry as well as different beam splitters  $A$  and  $B$  with arbitrary transparency. When we consider limiting cases for e.g. small temperature, bias or asymmetry, known results are recovered. This detailed analysis of the MZ-interferometer is of importance when comparing to the HBT-interferometer below.

The HBT-interferometer is less well known than the MZ-interferometer and deserves some additional comments. [7] The HBT-interferometer was invented as a tool to measure the angular diameter of stars. The first measurement [8] was carried out on a radio star in 1954. Compared to existing schemes based on Michelson interferometers, the HBT-interferometer proved to be less sensitive to atmospheric scintillations, which allowed for a more accurate determination of the angular diameter. After having demonstrated a table-top version of the interferometer in the visual range, [9] the angular diameter of the visual star Sirius was determined. [10]

The experimental results, both the two-particle interference and the positive intensity cross correlations, were successfully explained within a semi-classical framework. Soon after the experiments, it was however shown by Purcell [11] that the positive cross correlations could be explained in terms of bunching of individual photons, emerging from the star, a thermal source of light. This bunching was also demonstrated explicitly in subsequent photon counting experiments. [12, 13] The HBT experiment thus laid the foundations for quantum statistical methods in quantum optics. [14] The HBT approach has also been of importance in experimental particle physics. [15] It is interesting to note that positive intensity cross correlations between beams of light emerging from a thermal source, according to some contemporary [16,

17] "would call for a major revision of some fundamental concepts in quantum mechanics". Purcell, [11] however, providing an elegant explanation of the bunching phenomena, pointed out that "the Hanbury Brown Twiss effect, far from requiring a revision of quantum mechanics, is an instructive illustration of its elementary principles".

An optical table-top version [18, 19] of the HBT-interferometer is shown in Fig. 2.7. A beam of light is emitted from each one of the sources 2 and 3, completely uncorrelated with each other. The beams are split in two partial beams at the semitransparent beam splitters C and D respectively. The partial beams acquire phases  $\phi_1$  to  $\phi_4$  before scattering at the second pair of beam splitters A and B. The resulting beams are collected in detectors at ports 5 to 8.

Importantly, there is no interference pattern in the intensities at the detectors 5 to 8, instead the interference occurs only in the cross correlations between intensities at 5,6 and 7,8. The intensity cross correlations are sensitive to the two-particle amplitudes: the interference is thus between two different two-particle scattering events, e.g. (i) one particle from 2 scatters to 5 and one particle from 3 scatters to 8, with an amplitude  $A_1 \exp(i[\phi_1 + \phi_2])$  and (ii) one particle from 2 scatters to 8 and one particle from 3 scatters to 5, with an amplitude  $A_2 \exp(i[\phi_3 + \phi_4])$ . The amplitude to detect one particle in 5 and one in 8 is then the sum of the two two-particle amplitudes. This is the case since both scattering processes have the same initial and final states and can not be distinguished. The (reducible) cross correlation between intensities in 5 and 8 is directly related to the corresponding two-particle probability. The interference term  $2\text{Re}\{A_1 A_2^* \exp(i[\phi_1 + \phi_2 - \phi_3 - \phi_4])\}$  contains the four geometrical phases  $\phi_1$

to  $\phi_4$ . The HBT-interferometer is thus, in contrast to the MZ-interferometer, a two-particle interferometer.

The electrical analog of the HBT-interferometer, presented in Ref. [33], is shown in Fig. 2.8. It consists of a (rectangular) conductor with a hole in the middle, a Corbino geometry. Similar to the MZ-interferometer, the electrons propagate along single edge states. Scattering between the edge states takes place only at the beam splitters  $A$  to  $D$ .

In this chapter, the investigation and the comparison of the current and zero-frequency noise in electronic MZ and HBT interferometers are shown in detail. We consider interferometers implemented in mesoscopic conductors in the integer Quantum Hall regime, where the transport takes place along single edge states and Quantum Point Contacts (QPC's) serve as controllable beam splitters. The effect of finite temperature, applied bias and asymmetry, i.e. unequal length of the interferometer arms, is investigated. The strength of the interference contribution is quantified via the visibility of the phase oscillations. The dependence of the visibility on the beam splitter transparencies as well as on the temperature, voltage and asymmetry is discussed in detail. Of interest is the comparison of visibility of the shot-noise correlation of the MZ-interferometer and the HBT-intensity interferometer. Shot noise correlations in the MZ-interferometer exhibit two contributions, one with the fundamental period of  $h/e$  and a second harmonic with period  $h/2e$ . The shot noise correlations in the HBT-interferometer, even though they are due to two particle processes, are periodic with period  $h/e$ . Thus the Aharonov-Bohm period can not be used to identify the two particle processes which give rise to the HBT effect. It is therefore interesting to ask whether the HBT two-particle processes have any other signature, for instance in the temperature or voltage dependence of the visibility of the shot-noise correlation. We find that this is not the case. To the contrary,

we find that the shot noise correlations in the HBT intensity interferometer behave qualitatively similar to the  $h/e$  shot noise correlation in the MZ-interferometer. In contrast the  $h/2e$  contribution in the shot noise of the MZ-interferometer decreases more rapidly with increasing temperature, voltage or dephasing rate than the  $h/e$  oscillation in the MZ- or HBT-interferometer.

We investigate dephasing of the electrons propagating along the edge states by connecting one of the interferometer arms to a fictitious, dephasing voltage probe. In all cases, the current and noise of the MZ-interferometer as well as the noise in the HBT-interferometer, the effect of the voltage probe is equivalent to the effect of a slowly fluctuating phase.

## 2.2 Model and Theory



### 2.2.1 Optical analogs in the Quantum Hall regime

In this chapter we consider implementations of the MZ and HBT interferometers in mesoscopic conductors is considered in strong magnetic fields, in the integer Quantum Hall regime. [20] The typical system is a two-dimensional electron gas in a semiconductor heterostructure, with the lateral confinement of the electron gas controllable via electrostatic gating. The transport between reservoirs [21] connected to the conductor takes place along edge states. [22] The edge states, quantum analogs of classical skipping orbits, are chiral. The transport along an edge state is unidirectional. Scattering between edge states is suppressed everywhere in the conductor except at electrostatically controllable constrictions, QPC's. [23, 24] For a magnetic field that does not break the spin degeneracy of the edge states, each edge state supplies two conduction modes, one per spin.

These properties make conductors in the integer quantum Hall regime ideal for realizing analogs of optical experiments. First, the edge states correspond to single mode waveguides for the light. The unidirectional motion along the edge states allows for "beams" of electrons to be realized. Second, the QPC's work as electronic beam splitters with controllable transparency. Moreover, due to chirality the beamsplitters are reflectionless, a property essential for the MZ and HBT interferometers but difficult to achieve for beam splitters in conductors in weak (or zero) magnetic fields. [25, 26] These properties of conductors in the quantum Hall regime have been demonstrated experimentally in a number of works, see e.g. [27], [28] and [29].

Theoretically, several works have been concerned with the conductance and noise properties of beam splitters and interferometers in Quantum Hall systems, for recent reviews see e.g. Refs. [30] and [31]. Recently, it was proposed to use these appealing properties of edge states in the context of orbital [32] quasi-particle entanglement in static [33-35] and dynamic [36, 37] systems as well as for quantum state transfer. [38]

It is interesting to note that the edge state description also hold for conductors at even higher magnetic fields, in the fractional Quantum Hall regime. As examples, the fractional charge has been determined in shot-noise experiments [39, 40] and the quantum statistical properties of the fractionally charged quasi-particles have been investigated theoretically in beam-splitter [41] and HBT [42] geometries. Various interferometer structures have also been considered. [43-45] Very recently, a MZ-interferometer in the fractional Quantum Hall regime was proposed. [46] Here we however consider only the integer Quantum Hall effect, where the quasi-particles are noninteracting and the electrical analogs to optical experiments can be directly realized.

## 2.2.2 Scattering approach to current and noise

This discussion leads us to consider single mode, multi-terminal conductors with noninteracting electrons. The principal aim of this chapter is a comparison of the MZ and HBT-interferometers. In reality in both interferometers interactions (screening) play a role both for the voltage and temperature dependence. A non-interacting scattering approach is not gauge invariant but requires a treatment of screening. [47] However, these effects are expected to be similar in the two interferometers and will not affect the main conclusions of this chapter. Therefore, below we treat non-interacting quasi-particle interferometers. The conductors are connected to several electronic reservoirs, biased at a voltage  $eV$  or grounded. The current [48] and the noise [49, 50] are calculated within the scattering approach for multi-terminal conductors. We first introduce the creation and annihilation operators for ingoing,  $\hat{a}_\alpha^\dagger(E)$  and  $\hat{a}_\alpha(E)$ , and outgoing,  $\hat{b}_\alpha^\dagger(E)$  and  $\hat{b}_\alpha(E)$ , particles, at energy  $E$  in terminal  $\alpha$ . For simplicity we suppress spin notation. Considering a conductor with  $N$  terminals, the in- and out-going annihilation operators are related via the  $N \times N$  scattering matrix, as

$$\hat{b}_\alpha(E) = \sum_{\beta=1}^N s_{\alpha\beta}(E) \hat{a}_\beta(E), \quad (2.1)$$

where  $s_{\alpha\beta}(E)$  is the amplitude to scatter from terminal  $\beta$  to terminal  $\alpha$ .

The current operator in the lead  $\alpha$  has the form [48]

$$\begin{aligned} \hat{I}_\alpha(t) &= \frac{e}{h} \sum_{\beta\gamma} \int dE dE' (i[E - E']t/\hbar) \\ &\times A_{\beta\gamma}^\alpha(E, E') \hat{a}_\beta^\dagger(E) \hat{a}_\gamma(E'), \end{aligned} \quad (2.2)$$

with the notation

$$A_{\beta\gamma}^\alpha(E, E') = \delta_{\alpha\beta} \delta_{\alpha\gamma} - s_{\alpha\beta}^*(E) s_{\alpha\gamma}(E'). \quad (2.3)$$

The average current is given by [48]

$$\langle I_\alpha \rangle = \int dE j_\alpha(E), \quad (2.4)$$

where the spectral current density is

$$j_\alpha(E) = \frac{1}{e} \sum_{\beta} G_{\alpha\beta}(E) f_{\beta}(E). \quad (2.5)$$

Here  $f_{\beta}(E) = 1/(1 + \exp[(E - eV_{\beta})/k_B T])$  is the Fermi Dirac distribution of terminal  $\beta$ , with  $V_{\beta}$  the corresponding applied voltage. The spectral conductance  $G_{\alpha\beta}(E)$  is given by

$$G_{\alpha\beta}(E) = \frac{e^2}{h} A_{\beta\beta}^{\alpha}(E, E). \quad (2.6)$$

The zero frequency correlator between current fluctuations in terminals  $\alpha$  and  $\beta$  is defined as

$$S_{\alpha\beta} = \int dt \langle \Delta \hat{I}_{\alpha}(0) \Delta \hat{I}_{\beta}(t) + \Delta \hat{I}_{\beta}(t) \Delta \hat{I}_{\alpha}(0) \rangle, \quad (2.7)$$

where  $\Delta \hat{I}_{\alpha}(t) = \hat{I}_{\alpha}(t) - \langle \hat{I}_{\alpha}(t) \rangle$ . The current correlator is given by [49, 50]

$$S_{\alpha\beta} = \int dE S_{\alpha\beta}(E), \quad (2.8)$$

where

$$S_{\alpha\beta}(E) = \frac{2e^2}{h} \sum_{\gamma\delta} A_{\gamma\delta}^{\alpha}(E, E) A_{\delta\gamma}^{\beta}(E, E) \times f_{\gamma}(E) [1 - f_{\delta}(E)] \quad (2.9)$$

is the spectral current correlator.

### 2.2.3 Dephasing voltage probe model

There are several physical mechanisms that might lead to dephasing of the electrons propagating along the edge states (see e.g. the discussion in Ref. [27]). In this work we are not interested in any particular mechanism for dephasing but

consider instead a phenomenological model, a dephasing voltage probe. The idea of using a voltage probe to induce dephasing was introduced in Refs. [51] and [52]. A voltage probe connected to a mesoscopic sample was considered, leading to a suppression of coherent transport due to inelastic scattering. The probe model, originally considered for the average current, was extended to treat the effect of inelastic scattering on shot noise by Büttiker and Beenakker [53] by considering a conservation of current fluctuations at the probe as well. Later De Jong and Beenakker [54] extended the voltage probe concept and introduced a (fictitious) voltage probe which breaks phase but does not dissipate energy. Scattering in the voltage probe is (quasi-)elastic. This is achieved with the help of a distribution function in the voltage probe which conserves not only total current like a real voltage probe, but conserves current in every small energy interval. Such a probe provides a model of pure dephasing. The different probe models have been used as qualitative models in a number of works, see Refs. [30] and [55] for a review. For an application to quantum Hall systems, see Ref. [56].

In this chapter we consider the dephasing voltage probe model, which conserves the current at each energy. The model is based on the assumption that the current is conserved on a time scale  $\tau_C$ , much shorter than the time of the measurement but much longer than the time between injections of individual electrons, here of the order of  $\hbar/eV$ . One could however consider a more general voltage probe model that takes into account a more complicated dynamics of the probe. A detailed discussion of such a general model in the light of recent work [3, 4, 57, 58] is however deferred to a later work. [65,66] Here we only note that below we find that the voltage probe in both the MZ and HBT-interferometers only gives rise to a suppression of the phase dependent terms in conductance and noise, just as one would naively expect to be the effect of pure dephasing.



The condition of zero current into the fictitious probe  $\gamma$  at each energy is fulfilled by considering a time dependent distribution function of the probe

$$f_\gamma(E, t) = \bar{f}_\gamma(E) + \delta f_\gamma(E, t), \quad (2.10)$$

where  $\delta f_\gamma(E, t)$  fluctuates to conserve current on the timescale  $\tau_C$ . As a consequence, the spectral current density at each energy in lead  $\alpha$  fluctuates in time as

$$j_\alpha(E, t) = j_\alpha(E) + \Delta j_\alpha(E, t), \quad (2.11)$$

where the fluctuations  $\Delta j_\alpha(E, t) = \delta j_\alpha(E, t) + (1/e)G_{\alpha\gamma}(E)\delta f_\gamma(E, t)$  consist of two parts, the intrinsic fluctuations  $\delta j_\alpha(E, t)$  and the additional fluctuations due to  $\delta f_\gamma(E, t)$ . The requirement of zero average current into the probe,  $j_\gamma(E) = 0$ ,

leads to the averaged distribution function at the probe reservoir  $\gamma$

$$\bar{f}_\gamma(E) = -\sum_{\alpha \neq \gamma} \frac{G_{\gamma\alpha}(E)}{G_{\gamma\gamma}(E)} f_\alpha(E). \quad (2.12)$$

The average spectral current density  $j_\alpha^{dp}(E)$  is then found from Eq. (2.5).

The fluctuating part of the distribution function,  $\delta f_\gamma(E, t)$ , is obtained from the requirement of zero current fluctuations into the probe,  $\Delta j_\gamma(E, t) = \delta j_\gamma(E, t) + (1/e)G_{\gamma\gamma}(E)\delta f_\gamma(E, t) = 0$ . The total current density fluctuation is then given by

$$\Delta j_\alpha(E, t) = \delta j_\alpha(E, t) - \frac{G_{\alpha\gamma}(E)}{G_{\gamma\gamma}(E)} \delta j_\gamma(E, t). \quad (2.13)$$

As a result, in the presence of dephasing the total spectral current correlation

$S_{\alpha\beta}^{dp}(E)$  is

$$\begin{aligned}
S_{\alpha\beta}^{dp}(E) &= S_{\alpha\beta}(E) - \frac{G_{\alpha\gamma}(E)}{G_{\gamma\gamma}(E)} S_{\beta\gamma}(E) - \frac{G_{\beta\gamma}(E)}{G_{\gamma\gamma}(E)} S_{\alpha\gamma}(E) \\
&+ \frac{G_{\alpha\gamma}(E)G_{\beta\gamma}(E)}{G_{\gamma\gamma}^2(E)} S_{\gamma\gamma}(E),
\end{aligned} \tag{2.14}$$

where  $S_{\alpha\beta}(E)$  is the correlation function between the intrinsic current fluctuations,  $\delta j_\alpha$  and  $\delta j_\beta$ , of contact  $\alpha$  and  $\beta$ , given by Eq. (2.9), and  $G_{\alpha\beta}(E)$  is the conductance, given by Eq. (2.6).

### 2.3 Mach-Zehnder interferometers

The discussion of a fully coherent MZ interferometer is first shown; the effect of dephasing is investigated below. An electric potential  $eV$  is applied at terminal 1, all other terminals are kept at zero potential. The injected electrons propagate along single edge states. Scattering between the edge states can take place only at the two QPC's, acting as beam splitters with controllable transparency. The beam splitters  $j = A, B$  are characterized by the scattering matrices

$$\begin{pmatrix} i\sqrt{R_j} & \sqrt{T_j} \\ \sqrt{T_j} & i\sqrt{R_j} \end{pmatrix}, \tag{2.15}$$

where  $T_j$  and  $R_j = 1 - T_j$  are the transmission and reflection probabilities, respectively. We note that any additional phases of the beam splitters just give rise to a constant phase shift of the oscillations in the interference terms and are therefore not considered. In a typical system, where Fermi energy is not small, the energy dependence of transport amplitude would not give significant influence and could be neglect.

Propagating along the edge states, the electrons pick up geometrical phases  $\phi_1$  and  $\phi_2$  as well as phases  $\psi_1$  and  $\psi_2$  due to the AB-flux  $\Phi$  through

the center of the interferometer. For example, the amplitude for scattering from terminal 1 to 4 is given by

$$s_{41} = i\sqrt{T_B R_A} e^{i(\phi_1 + \psi_1)} + i\sqrt{T_A R_B} e^{i(\phi_2 - \psi_2)} . \quad (2.16)$$

For the geometrical phases, to be specific we consider the case when the potential landscape  $eU(x,y)$  of the conductor in Fig. 2.2 is varying smoothly on the scale of the magnetic length  $l_B = (\hbar/e|B|)^{1/2}$ , with  $B\hat{z}$  the applied magnetic field perpendicular to the plane in Fig. 2.2 (the effect of self-consistency of the potential [59] is neglected). This allows for a semi-classical treatment. [60] In a high magnetic field the edge states at Fermi energy  $E_F$  follow equipotential lines determined by  $eU(x,y) = E_F - \hbar\omega_c(n + 1/2)$  where  $\omega_c = eB/m$  is the cyclotron frequency and  $m$  the effective electron mass. We are concerned here with the case where there is only one edge state and thus  $n = 0$ . Suppose the  $x$ -axis is a line intersecting QPC's  $A$  and  $B$  in Fig. 2.2. Excluding self-intersections we can express the edge state in terms of functions  $y_1(x)$  and  $y_2(x)$  for the left and right path of the interferometer. Working in the symmetric gauge, the geometric phases can be written [60]  $\phi_i = -l_B^{-2} \int_{x_A}^{x_B} dx y_i(x)$ , where  $x_A$  and  $x_B$  are the locations of the QPC's. Importantly,  $\phi_1 - \phi_2$  corresponds to the total area  $A$  enclosed by these two paths divided by the magnetic length squared, or  $\phi_1 - \phi_2 = 2\pi BA/\Phi_0$  where  $BA$  is the total flux through the enclosed area and  $\Phi_0 = h/e$  the elementary flux quantum. Note that the Aharonov-Bohm flux  $\Phi$  adds an additional phase  $\psi_1$  and  $\psi_2$ , with  $\psi_1 + \psi_2 = 2\pi\Phi/\Phi_0$ , to each of the paths.

For the discussion of the temperature and voltage dependence of the current and the noise, we also need to know the energy dependence of the phases. First, instead of parameterizing the edge state through  $x$  we introduce the parameter  $s$  which

measures directly the path length, i.e.  $x(s)$ ,  $y(s)$ . In addition at  $s$  we introduce local coordinates  $s_{\parallel}$  along and  $s_{\perp}$  perpendicular to the equipotential line. In these coordinates, an edge state that follows the equipotential line at a small energy  $E$  away from  $E_F$  acquires the additional phase  $\Delta\phi = -l_B^{-2} \int ds \Delta s_{\perp}$  with  $e(dU/ds_{\perp})\Delta s_{\perp} = E$ . The potential gradient  $dU/ds_{\perp}$  determines the local electric field  $F(s) = -dU/ds_{\perp}$  at  $s$ . But  $eF(s)l_B = \hbar v_D(s)$  where  $v_D(s) = F(s)/B$  is the drift velocity of the guiding center of the cyclotron orbit at point  $s$  of the edge state. Thus a small increase in energy leads to a phase increment given by  $\Delta\phi_i = \int ds [1/\hbar v_D(s_i)] E$ . A rough estimate using a drift velocity which is constant along the edge gives  $\Delta\phi_i \approx (L_i/\hbar v_D) E$  with  $L_i$  the length of the edge state  $i$ . For the phase-difference of the two interfering paths we have

$$\phi_1(E) - \phi_2(E) = \Delta\phi(E_F) + E/E_c \quad (2.17)$$

with  $\Delta\phi(E_F) = \phi_1(E_F) - \phi_2(E_F)$  the equilibrium phase difference. Formally, higher order terms in energy can be neglected for characteristic energies  $k_B T$  and  $eV$  much smaller than  $(dU/ds_{\perp})^2/[d^2U/ds_{\perp}^2]$ . The asymmetry of the two edges thus gives rise to an energy scale  $E_c = \left\{ \int ds [1/\hbar v_D(s_1)] - \int ds [1/\hbar v_D(s_2)] \right\}^{-1}$  which is due to the mismatch of the edge state path lengths, i.e.  $E_c \approx \hbar v_D/(\Delta L)$  with  $\Delta L = L_1 - L_2$ . In principle, for a completely symmetric interferometer one has  $E_c \rightarrow \infty$ .

Given the scattering amplitudes  $S_{\alpha\beta}$ , the spectral current density is found from Eqs. (2.3), (2.5) and (2.6). For e.g. terminal 4, one gets

$$j_4(E) = (e/h)[f(E) - f_0(E)][T_A R_B + T_B R_A + 2\sqrt{T_A T_B R_A R_B} \cos(E/E_c + \Theta)], \quad (2.18)$$

where we introduce the total, energy independent phase  $\Theta = \Delta\phi(E_F) + 2\pi\Phi/\Phi_0$ . Here  $f_0(E)$  is the distribution functions of the grounded terminals 2, 3 and 4 and  $f(E) = f_0(E - eV)$  is the distribution function of terminal 1. The current is then given from Eq. (2.4), as

$$I_4 = \frac{e}{h} \left[ (\mathcal{T}_A R_B + \mathcal{T}_B R_A) eV + \sqrt{\mathcal{T}_A \mathcal{T}_B R_A R_B} \times 4\pi k_B T \operatorname{csch}\left(\frac{k_B T \pi}{E_c}\right) \sin\left(\frac{eV}{2E_c}\right) \cos\left(\frac{eV}{2E_c} + \Theta\right) \right]. \quad (2.19)$$

Current conservation gives  $I_3 = (e^2/h)V - I_4$ . The current consists of two physically distinct parts. The first term in Eq. (2.19) is the phase independent, incoherent part, the current in the absence of interference, while the second, phase dependent term is the interference contribution. We note that a bias  $eV$  of the order of the asymmetry energy  $E_c$  leads to the phase shifts of the oscillation. The strength of the interference can conveniently be quantified via the visibility as

$$v_I = \frac{I_{\max} - I_{\min}}{I_{\max} + I_{\min}} = \frac{\operatorname{amp}[I]}{\langle I \rangle}, \quad (2.20)$$

which gives for the current in the MZ-interferometer

$$v_{I,MZ} = \frac{\sqrt{\mathcal{T}_A \mathcal{T}_B R_A R_B}}{\mathcal{T}_A R_B + \mathcal{T}_B R_A} \times \frac{4\pi k_B T}{eV} \operatorname{csch}\left(\frac{k_B T \pi}{E_c}\right) \left| \sin\left(\frac{eV}{2E_c}\right) \right|. \quad (2.21)$$

The visibility is a product of a term containing the QPC scattering probabilities and a function depending on the energy scales  $k_B T$ ,  $eV$  and  $E_c$ . The scattering probability term is maximum for identical QPC's,  $\mathcal{T}_A = \mathcal{T}_B$ . The energy scale dependence is shown in Fig. 2.3 where the visibility for identical point contacts is plotted as a function of the normalized temperature,  $k_B T/E_c$ . We note several interesting features from Fig. 2.3 and Eq. (2.21). (i) The visibility shows decaying

oscillations as a function of voltage  $v_{I,MZ} \propto |\sin(eV/2E_c)|/eV$  for arbitrary temperature. (ii) A symmetric MZ-interferometer,  $E_c \gg k_B T$ ,  $eV$ , has unity visibility (for  $T_A = T_B$ ), i.e. shows perfect interference. (iii) The visibility decays monotonically with increasing temperature. For large temperatures,  $k_B T \gg E_c$ , the visibility decays exponentially with the temperature as  $v_{I,MZ} \propto k_B T \exp(-\pi k_B T/E_c)$ .

It is interesting to compare the calculated visibility to the experimentally measured one in Ref. [27]. As already shown in Ref. [27], the measured scattering probability dependence of  $v_{I,MZ}$  is well reproduced by Eq. (2.21). For the energy scale dependence, no information about the drift velocity  $v_D$  or the asymmetry  $\Delta L$  needed to determine  $E_c$  is provided in Ref. [27]. However, to obtain the order of magnitude of  $E_c$ , considering as a rough estimate a typical drift velocity [61]  $v_D \sim 10^4$  m/s at a magnetic field  $B \sim 1T$  and an asymmetry  $\Delta L \sim 0.1\mu$  m gives an  $E_c$  corresponding to an applied bias  $\sim 10\mu V$  or a temperature  $\sim 100mK$ . These values are typically of the same order of magnitude as the ones considered in the experiment. As a first approximation, one would thus expect asymmetry effects to be of importance. The observed temperature dependence, a strong decrease of the visibility for increased temperature, is also qualitatively described by Eq. (2.21) with an  $E_c/k_B \sim 50$  mK. This is however not the case with the voltage dependence. Ji et al. find a differential visibility, i.e. the visibility of  $dI(V)/dV$ , which decays strongly with applied voltage, while Eq. (2.19) predicts a constant, voltage independent differential visibility. There are several possible explanations to why the voltage dependence in contrast to the temperature dependence is not reproduced by the theory. Ji et al. themselves point out two voltage dependent dephasing mechanisms: low frequency noise of  $1/f$  type due to moving impurities, induced by a higher current and fast fluctuations of the potential

landscape (and hence of the phase via the enclosed area) caused by screening of the additional charges injected at higher current. Screening might also, for the nonlinear current-voltage characteristics predicted by Eq. (2.19), lead to a voltage dependent renormalization of the transmission probabilities, introducing a voltage dependence in the differential visibility. [47, 62] We note that in the model of Ref. [5], inducing dephasing by coupling the MZ-interferometer to a quantum bath, gives a dephasing rate that increases with increasing voltage. Latter MZI experiments in Ref. [63- 65, 67] give no conclusive results for the theoretical predictions. Clearly, further investigations are needed to clarify the origin of the dephasing.

Turning to the noise, we focus on the cross correlator between currents flowing in terminals 3 and 4 (the auto-correlator can be obtained analogously). This allows for a straightforward comparison to the result of the HBT-interferometer, for which the cross correlator was investigated in Ref. [33]. From Eqs. (2.8) and (2.9) and the expressions for the scattering amplitudes, we arrive at the noise spectral density

$$S_{34}(E) = \frac{-2e^2}{h} [f(E) - f_0(E)]^2 \times \left\{ c_0 + c_\Theta \cos\left(\frac{E}{E_c} + \Theta\right) + c_{2\Theta} \cos\left(2\left[\frac{E}{E_c} + \Theta\right]\right) \right\}, \quad (2.22)$$

with coefficients

$$\begin{aligned} c_0 &= T_A R_A + T_B R_B - 6T_A R_A T_B R_B, \\ c_\Theta &= 2(T_A - R_A)(T_B - R_B) \sqrt{T_A T_B R_A R_B}, \\ c_{2\Theta} &= 2T_A T_B R_A R_B. \end{aligned} \quad (2.23)$$

Performing the energy integrals in Eq. (2.8) we find for the cross correlator

$$S_{34} = -\frac{2e^2}{h} \left\{ c_0 \bar{S}_0 + c_\Theta \bar{S}_\Theta \cos\left(\frac{eV}{2E_c} + \Theta\right) + c_{2\Theta} \bar{S}_{2\Theta} \cos\left[2\left(\frac{eV}{2E_c} + \Theta\right)\right] \right\} \quad (2.24)$$

where we introduce the functions

$$\bar{S}_0 = eV \coth \frac{eV}{2k_B T} - 2k_B T, \quad (2.25)$$

and

$$\begin{aligned} \bar{S}_{m\Theta} = & 2\pi k_B T \operatorname{csc} h \left( \frac{m\pi k_B T}{E_c} \right) \left[ \coth \left( \frac{eV}{2k_B T} \right) \right. \\ & \left. \times \sin \left( \frac{meV}{E_c} \right) - \frac{mk_B T}{E_c} \cos \left( \frac{meV}{E_c} \right) \right]. \end{aligned} \quad (2.26)$$

containing the dependence on the energy scales  $eV$ ,  $k_B T$  and  $E_c$ .

Just as the current in Eq. (2.19), the noise consists of a phase independent, incoherent part and a phase dependent, interference part. However, in contrast to the current, the phase dependent part of the noise contains two terms with different periods in  $\Theta$ , corresponding to oscillations periodic in  $h/e$  and  $h/2e$ . These terms result from two-particle scattering processes which enclose the AB-flux one and two times respectively. Similarly to the current, the phases of the oscillations are shifted for a bias  $eV$  of the order of the asymmetry energy  $E_c$ .

It is important to note that in the MZ (in contrast to the HBT) interferometer, two particle and higher order scattering processes are just products of single particle scattering processes. The full distribution of current fluctuations [6] is thus a function of single particle scattering probabilities only. In particular, the noise spectral density  $S_{34}(E)$  in Eq. (2.22) is proportional to  $-|s_{41}|^2 |s_{31}|^2$ , i.e. partition noise [50] with phase dependent scattering probabilities. As a consequence, the phase independent, incoherent part of the noise can not be understood as partition noise from incoherent single particle processes, i.e.  $\langle |s_{41}|^2 \rangle_{inc} \langle |s_{31}|^2 \rangle_{inc} \neq \langle |s_{41}|^2 |s_{31}|^2 \rangle_{inc}$ . This is formally clear since the term proportional to  $\cos^2 \Theta = [1 + \cos(2\Theta)]/2$ , from two coherent scattering processes; it obviously contributes to the phase independent part of the noise. As a consequence, as shown by Marquardt and Bruder, [3, 4] a model [30] with

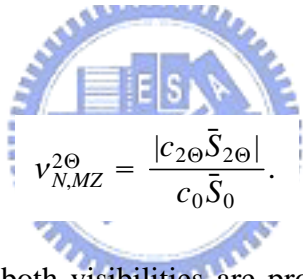


a filled stream of classical particles injected from reservoir 1 correctly reproduce the incoherent part of the current but fails to reproduce the incoherent part of the noise. In contrast, as found in Ref. [4] and further discussed below, the completely dephasing voltage probe model correctly reproduces the incoherent part of both the current and the noise.

To quantify the strength of the oscillations we introduce two separate quantities,  $v_{N,MZ}^\ominus$  and  $v_{N,MZ}^{2\ominus}$ , here simply called visibilities, which in close analogy to the current visibility in Eq. (2.21) are defined as the ratio of the amplitudes of the noise oscillations and the average noise. They become

$$v_{N,MZ}^\ominus = \frac{|c_\ominus \bar{S}_\ominus|}{c_0 \bar{S}_0} \quad (2.27)$$

and



$$v_{N,MZ}^{2\ominus} = \frac{|c_{2\ominus} \bar{S}_{2\ominus}|}{c_0 \bar{S}_0}. \quad (2.28)$$

Similarly to the current, both visibilities are products of a term containing the scattering probabilities and a function of the energy scales  $eV$ ,  $k_B T$  and  $E_c$ . We first focus on the scattering probability dependent term by considering the visibility in the limit of a symmetric interferometer,  $E_c \gg eV$ ,  $k_B T$ , where the energy-scale dependent terms are unity. This gives

$$v_{N,MZ}^\ominus = \frac{2|(\mathcal{T}_A - \mathcal{R}_A)(\mathcal{T}_B - \mathcal{R}_B)|\sqrt{\mathcal{T}_A \mathcal{T}_B \mathcal{R}_A \mathcal{R}_B}}{\mathcal{T}_A \mathcal{R}_A + \mathcal{T}_B \mathcal{R}_B - 6\mathcal{T}_A \mathcal{R}_A \mathcal{T}_B \mathcal{R}_B} \quad (2.29)$$

and

$$v_{N,MZ}^{2\ominus} = \frac{2\mathcal{T}_A \mathcal{T}_B \mathcal{R}_A \mathcal{R}_B}{\mathcal{T}_A \mathcal{R}_A + \mathcal{T}_B \mathcal{R}_B - 6\mathcal{T}_A \mathcal{R}_A \mathcal{T}_B \mathcal{R}_B}. \quad (2.30)$$

The two visibilities are plotted in Fig. 2.4. Both visibilities are symmetric under the substitutions  $\mathcal{T}_A \leftrightarrow \mathcal{R}_A$  and  $\mathcal{T}_B \leftrightarrow \mathcal{R}_B$ . The visibility  $v_{N,MZ}^\ominus$  is zero for

$\mathcal{T}_A = R_A = 1/2$  , i.e. for a symmetric setting of any of the QPC's. The visibility increases for increasing QPC asymmetry, reaching a maximum for  $0 < \mathcal{T}_A < 0.5$  and  $0 < \mathcal{T}_B < 0.5$  (unity only in the limit  $\mathcal{T}_A, \mathcal{T}_B \ll 1$  ) and then decreases again toward zero at  $\mathcal{T}_A = 0$  or  $\mathcal{T}_B = 0$  . Interestingly, the visibility  $v_{N,MZ}^{2\Theta}$  shows an opposite behavior. It is maximum, equal to unity, at  $\mathcal{T}_A = \mathcal{T}_B = 1/2$  and then decreases monotonically for increasing QPC asymmetry, reaching zero at  $\mathcal{T}_A = 0$  or  $\mathcal{T}_B = 0$  . This different dependence on the scattering probabilities makes it possible to investigate the two oscillations independently by modulating the QPC transparencies.

Turning to the energy scale behavior, we consider for simplicity  $v_{N,MZ}^{\Theta}$  in the limit  $\mathcal{T}_A, \mathcal{T}_B \ll 1$  and  $v_{N,MZ}^{2\Theta}$  in the limit  $\mathcal{T}_A = \mathcal{T}_B = 1/2$  where respective scattering probability terms are unity. For a symmetric interferometer, i. e.  $E_c \gg eV, k_B T$  , both visibilities are unity. Considering the situation when the temperature is comparable to the asymmetry energy scale  $E_c$  but the voltage is small  $eV \ll k_B T, E_c$  , we get the visibilities (m=1, 2)

$$v_{N,MZ}^{m\Theta} = \frac{m\pi k_B T}{E_c} \operatorname{csc} h \left( \frac{m\pi k_B T}{E_c} \right) \left[ 1 + \left( \frac{mk_B T}{E_c} \right)^2 \right]. \quad (2.31)$$

The temperature dependences of the visibilities are shown in Fig. 2.5. Both visibilities decrease monotonically with increasing temperature. For large temperature  $k_B T \gg E_c$  , the visibilities decay exponentially as  $v_{N,MZ}^{\Theta} \propto (k_B T)^3 (-\pi k_B T / E_c)$  and  $v_{N,MZ}^{2\Theta} \propto (k_B T)^3 (-2\pi k_B T / E_c)$  . The visibility  $v_{N,MZ}^{2\Theta}$  is thus considerably more sensitivity to thermal smearing than  $v_{N,MZ}^{\Theta}$  . In the opposite limit, for a small temperature but a voltage comparable to  $E_c$  , i. e.  $k_B T \ll E_c, eV$  , we instead get the visibilities

$$v_{N,MZ}^{m\Theta} = \frac{2E_c}{meV} \left| \sin\left(\frac{meV}{2E_c}\right) \right| \quad (2.32)$$

The visibilities as a function of voltage are plotted in Fig. 2.5. Both visibilities show an oscillating behavior, decaying as a power law  $\propto 1/eV$  with increasing voltage. The period of oscillations, in  $eV$ , is  $2\pi E_c$  for  $v_{N,MZ}^\Theta$  but  $\pi E_c$  for  $v_{N,MZ}^{2\Theta}$ , half the value for  $v_{N,MZ}^\Theta$ . The different voltage dependence gives an additional possibility to investigate the two visibilities independently.

In the experiment of Ji et al. [9] the noise was measured in the high voltage regime, with the interference terms in both the current and noise completely suppressed. The dependence of the incoherent noise on the transparencies  $\mathcal{T}_A$  and  $\mathcal{T}_B$  was investigated ( $\mathcal{T}_A$  was kept at  $1/2$  and  $\mathcal{T}_B$  was varied). A good agreement was found with the first, incoherent term in Eq. (2.24). Taken the open questions on the effect of decoherence on the average current, a detailed experimental investigation on the phase dependent, interference part of the noise would be of great interest.

### 2.3.1 Effect of dephasing

Next we consider the effect of dephasing on the current and noise. As discussed above, dephasing is introduced by connecting one of the two arms of the interferometer to a fictitious, dephasing voltage probe. The interferometer with the probe, denoted terminal 5, is shown in Fig. 2.6. The dephasing probe is connected to the edge via a contact described by a scattering matrix

$$\begin{pmatrix} \sqrt{1-\varepsilon} & i\sqrt{\varepsilon} \\ i\sqrt{\varepsilon} & \sqrt{1-\varepsilon} \end{pmatrix}, \quad (2.33)$$

where the dephasing parameter  $\varepsilon$  varies between 0 (no dephasing, fully coherent transport) and 1 (complete dephasing, fully incoherent transport). The presence of the dephasing probe modifies the amplitudes for scattering between terminal 1, 2, 3 and 4. As an example, the scattering amplitude  $s_{41}$ , given in Eq. (2.16) in the absence of dephasing, now becomes

$$s_{41}(\varepsilon) = i\sqrt{\mathcal{T}_B R_A} e^{i(\phi_1 + \psi_1)} + i\sqrt{1 - \varepsilon} \sqrt{\mathcal{T}_A R_B} e^{i(\phi_2 - \psi_2)}. \quad (2.34)$$

In addition, amplitudes for scattering into and out from the probe terminal 5 have to be considered. The current is obtained from Eqs. (2.4), (2.5) and (2.12). For the current in terminal 4, we find

$$I_4^{dp} = \frac{e}{h} [(\mathcal{T}_A R_B + \mathcal{T}_B R_A) eV + \sqrt{1 - \varepsilon} \sqrt{\mathcal{T}_A \mathcal{T}_B R_A R_B} 4\pi k_B T \text{csch}\left(\frac{k_B T \pi}{E_c}\right) \times \sin\left(\frac{eV}{2E_c}\right) \cos\left(\frac{eV}{2E_c} + \Theta\right)]. \quad (2.35)$$

Comparison with the result in the absence of dephasing in Eq. (2.19) shows that the effect of the dephasing is to suppress the phase-dependent oscillations by multiplying the phase-dependent interference term with a factor  $\sqrt{1 - \varepsilon}$ . For complete dephasing  $\varepsilon = 1$ , the phase dependent term is completely suppressed. The effect of dephasing can thus be simply incorporated in the visibility as

$$v_{I,MZ}^{dp} = \sqrt{1 - \varepsilon} v_{I,MZ}, \quad (2.36)$$

where  $v_{I,MZ}$  is the visibility of the current oscillations in the absence of dephasing, given by Eq. (2.21). As is clear from the discussion above, to account for the experimental observations in Ref. [27], one would have to consider a voltage dependent dephasing parameter  $\varepsilon$ .

Turning to the noise, we obtain the cross correlator between currents in lead 3 and 4 in the presence of dephasing from Eqs. (2.8) and (2.14), giving

$$S_{34}^{dp} = -\frac{2e^2}{h} \left\{ c_0 \bar{S}_0 + c_\Theta \bar{S}_\Theta \sqrt{1-\varepsilon} \cos\left(\frac{eV}{2E_c} + \Theta\right) + c_{2\Theta} \bar{S}_{2\Theta} (1-\varepsilon) \cos\left[2\left(\frac{eV}{2E_c} + \Theta\right)\right] \right\}. \quad (2.37)$$

Here the terms  $c_0$ ,  $c_\Theta$ ,  $c_{2\Theta}$ ,  $\bar{S}_0$ ,  $\bar{S}_\Theta$  and  $\bar{S}_{2\Theta}$  are defined above in Eqs. (2.23) and (2.25). Similarly to the current, the effect of the dephasing is only to suppress the amplitude of the phase-dependent oscillations. That is what one would naively expect to be the consequence of pure dephasing. The two phase-dependent terms are however affected differently, the  $\cos\Theta$  term is suppressed by a factor  $\sqrt{1-\varepsilon}$  while the  $\cos 2\Theta$  term is suppressed by  $(1-\varepsilon)$ . The  $\cos 2\Theta$  oscillations are thus more strongly suppressed. The visibilities of the two oscillations in the presence of dephasing can simply be written

$$v_{N,MZ}^{\Theta,dp} = \sqrt{1-\varepsilon} v_{N,MZ}^\Theta \quad (2.38)$$

and

$$v_{N,MZ}^{2\Theta,dp} = (1-\varepsilon) v_{N,MZ}^{2\Theta}, \quad (2.39)$$

where  $v_{N,MZ}^\Theta$  and  $v_{N,MZ}^{2\Theta}$  are the visibilities for the noise oscillations in the absence of dephasing, given by Eqs. (2.27) and (2.28), respectively.

Importantly, both oscillating terms are fully suppressed for complete dephasing,  $\varepsilon = 1$ . Complete dephasing within the voltage probe model thus gives a noise expression that only consists of the phase independent, incoherent term in Eq. (2.22). We note already here that the same result is found below for the HBT-interferometer. Since quantum interference by definition is excluded from the model, i.e. all scattering phases are neglected, the completely dephasing voltage probe thus constitutes a classical model that correctly reproduces the incoherent part of the noise. As pointed out above, a more detailed discussion of the physics of the voltage probe and a comparison with Refs. [3], [4] and [57] is deferred to a later work [65, 66].

It is interesting to note that the effect of dephasing introduced with the voltage probe, both for the current and the noise, is for arbitrary dephasing strength identical to a phase averaging. The results in Eqs. (2.38) and (2.39) can be obtained by averaging the fully coherent expressions in Eqs. (2.27) and (2.28) with respect to a Lorentzian distribution  $\rho(\Theta)$  of slow fluctuations of the phase  $\Theta$  around the average value  $\Theta_0$ , as

$$\int d\Theta \rho(\Theta) \cos(n\Theta) = (1 - \varepsilon)^{n/2} \cos(n\Theta_0) \quad (2.40)$$

with the Lorentzian distribution

$$\rho(\Theta) = \frac{a/\pi}{(\Theta - \Theta_0)^2 + a^2}, \quad a = -(1/2)\ln(1 - \varepsilon). \quad (2.41)$$

We note that, as pointed out in Ref. [4], a Gaussian distribution of the phase fluctuations gives a different result, not consistent with the dephasing voltage probe approach for arbitrary dephasing strength.

We emphasize that the results above are independent on to which edge the probe is connected. Moreover, we also point out that the effect of the voltage probes, for arbitrary  $\varepsilon$ , is multiplicative, i.e. attaching  $n$  voltage probes at arbitrary places along the arms can be described by renormalizing  $1 - \varepsilon \rightarrow (1 - \varepsilon)^n$ . Writing  $(1 - \varepsilon)^n = \exp(n \ln[1 - \varepsilon]) = \exp(-L/L_\phi)$ , with  $L_\phi = -d/\ln[1 - \varepsilon]$  and  $L = nd$  with  $d$  the distance between two probes, we can quite naturally incorporate the effect of a uniform distribution of probes into a dephasing length  $L_\phi$ . The suppression of the visibilities of the  $h/e$  and  $h/2e$  oscillations due to dephasing in Eqs. (2.38) and (2.39) are then modified as  $(1 - \varepsilon)^{1/2} \rightarrow \exp(-L/2L_\phi)$  and  $(1 - \varepsilon) \rightarrow \exp(-L/L_\phi)$ .

## 2.4 Hanbury Brown Twiss interferometers

Similar to the discussion for MZ interferometer, we first consider the fully coherent case, then the effects of the dephasing. The beam splitters of HBT interferometers are described by scattering matrices given by Eq. (2.15). In contrast to the MZ-interferometer, the scattering amplitudes contain the phases  $\phi_i$  and  $\psi_i$  only via multiplicative phase factors. As an example, the amplitude to scatter from terminal 2 to terminal 5 is given by

$$s_{52} = \sqrt{\mathcal{T}_A \mathcal{T}_C} e^{i(\phi_1 - \psi_1)}. \quad (2.42)$$

As a consequence, the average currents which depend only on the modulus squared of the scattering amplitudes [see Eqs. (2.4) and (2.6)] do not contain any scattering phases. We get the currents at terminals 5 to 8 as

$$\begin{aligned} I_5 &= (e^2/h)V (\mathcal{T}_A \mathcal{T}_C + R_A R_D), \\ I_6 &= (e^2/h)V (\mathcal{T}_A R_D + R_A \mathcal{T}_C), \\ I_7 &= (e^2/h)V (\mathcal{T}_B R_C + R_B \mathcal{T}_D), \\ I_8 &= (e^2/h)V (\mathcal{T}_B \mathcal{T}_D + R_B R_C). \end{aligned} \quad (2.43)$$

Turning to the current noise, the correlation between currents in terminals 5,6 and 7,8 is given by Eq. (2.9). We find the spectral density for the correlators between terminals 5 and 8

$$\begin{aligned} S_{58}(E) &= \frac{-2e^2}{h} [f(E) - f_0(E)]^2 \\ &\quad \times \{c_{0,58} + \bar{c}_\Theta \cos(E/E_c + \Theta)\} \end{aligned} \quad (2.44)$$

with the coefficients

$$\begin{aligned} c_{0,58} &= \mathcal{T}_A R_B \mathcal{T}_C R_C + \mathcal{T}_B R_A \mathcal{T}_D R_D; \\ \bar{c}_\Theta &= 2 \prod_{j=A,B,C,D} \sqrt{\mathcal{T}_j R_j}, \end{aligned} \quad (2.45)$$

and for the correlator between terminal 5 and 7

$$S_{57}(E) = \frac{-2e^2}{h} [f(E) - f_0(E)]^2 \times \{c_{0,57} + \bar{c}_\Theta \cos(E/E_c + \Theta)\} \quad (2.46)$$

with the coefficient

$$c_{0,57} = T_A T_B T_C R_C + R_A R_B T_D R_D. \quad (2.47)$$

Performing the energy integrals in Eq. (2.9), we obtain the corresponding current cross correlators

$$S_{58} = \frac{-2e^2}{h} \left[ c_{0,58} \bar{S}_0 + \bar{c}_\Theta \bar{S}_\Theta \cos\left(\frac{eV}{2E_c} + \Theta\right) \right] \quad (2.48)$$

and

$$S_{57} = \frac{-2e^2}{h} \left[ c_{0,57} \bar{S}_0 + \bar{c}_\Theta \bar{S}_\Theta \cos\left(\frac{eV}{2E_c} + \Theta\right) \right]. \quad (2.49)$$

Here  $\bar{S}_0$  and  $\bar{S}_\Theta$  are given by Eqs. (2.25) and (2.26). The other two correlators  $S_{67}$  and  $S_{68}$  are given by the substitutions  $S_{67} = S_{58}(\mathcal{T}_C \leftrightarrow \mathcal{T}_D)$  and  $S_{68} = S_{57}(\mathcal{T}_C \leftrightarrow \mathcal{T}_D)$ . Here, as for the MZ-interferometer we have  $\Theta = \Delta\phi(E_F) + 2\pi\Phi/\Phi_0$  with  $\Delta\phi = \phi_1 + \phi_2 - \phi_3 - \phi_4$  and  $\sum_{i=1}^4 \psi_i = 2\pi\Phi/\Phi_0$ .

Several observations can be made from the results above, put in comparison with the result for the noise correlations for the MZ-interferometer in Eq. (2.24). Just as for the MZ-interferometer, the noise consists of an incoherent, phase independent part, and a coherent, interference part. The phase dependent part of the noise in Eqs. (2.48) and (2.49) however contains only one term. The amplitude of the oscillating term is a product of a scattering probability term and an energy-scale dependent function, just as for the MZ-interferometer. This phase dependent term has the same dependence on the phase  $\Theta$ , the same voltage dependent phase shift as well as the same energy-scale dependence as the second term in Eq. (2.24). This is the case since they both arise from processes which enclose the AB-flux once. Despite the fact that in the



HBT interferometer the AB-effect results from two-particle processes, the periodicity is determined by the single electron flux quantum  $h/e$ . The dependence on the scattering probabilities is however different, a consequence of the MZ and HBT interferometer geometries being different. Importantly, there is no term in the noise in Eqs. (2.48) and (2.49) that corresponds to the last term in Eq. (2.24), describing processes which enclose the AB-flux twice. We note that the elementary scattering processes in the HBT-interferometer, in contrast to the MZ-interferometer, are two-particle processes. An important consequence of this is that the incoherent, phase independent noise term in Eqs. (2.48) and (2.49) can directly be reproduced by a model with filled streams of classical particles incident from reservoirs 2 and 3.

Since there is only one phase-dependent term, the visibility of the phase-dependent oscillations can again be directly defined, giving for  $\alpha = 5, 6$  and  $\beta = 7, 8$

$$v_{N,HBT}^{\ominus,\alpha\beta} = \frac{|\bar{c}_\ominus \bar{S}_\ominus|}{c_{0,\alpha\beta} \bar{S}_0}. \quad (2.50)$$

Since the energy-scale dependence of the visibilities is identical to  $v_{N,MZ}^\ominus$  for the MZ-interferometer in Eq. (2.27), shown in Fig. 2.5, we focus here only on the scattering probability terms. We thus consider the limit of a symmetric interferometer,  $E_c \gg k_B T, eV$  for which the energy-scale dependent part is unity. Several symmetries exist, e.g. all visibilities  $v_{N,HBT}^{\ominus,\alpha\beta}$  are unchanged by the substitutions  $R_C \leftrightarrow T_C$  and  $R_D \leftrightarrow T_D$ . The visibility  $v_{N,HBT}^{\ominus,58}$  is unity for scattering probabilities obeying  $T_A R_B R_C T_C = T_B R_A R_D T_D$  and similar relations hold for the other visibilities. All visibilities go to zero for any of the transmission probabilities

approaching either zero or unity. Focusing on the case with  $T_C = T_D$  (or equivalently  $T_C = R_D$ ), the visibilities are given by

$$v_{N,HBT}^{\Theta,58} = v_{N,HBT}^{\Theta,67} = \frac{2\sqrt{\mathcal{T}_A R_A \mathcal{T}_B R_B}}{\mathcal{T}_A R_B + \mathcal{T}_B R_A} \quad (2.51)$$

and

$$v_{N,HBT}^{\Theta,57} = v_{N,HBT}^{\Theta,68} = \frac{2\sqrt{\mathcal{T}_A R_A \mathcal{T}_B R_B}}{\mathcal{T}_A \mathcal{T}_B + R_A R_B}. \quad (2.52)$$

The two different visibilities are plotted in Fig. 2.9 as a function of  $\mathcal{T}_A$  for different  $\mathcal{T}_B$ . The visibility  $v_{N,HBT}^{\Theta,58}$  has a maximum equal to unity for  $\mathcal{T}_A = \mathcal{T}_B$ , while  $v_{N,HBT}^{\Theta,57}$  instead has a maximum equal to unity for  $\mathcal{T}_A = R_B$ .

### 2.4.1 The effect of dephasing

Just as in the MZ-interferometer, the dephasing in the HBT-interferometer is introduced by connecting a fictitious voltage probe to an edge between any of the two point contacts. The HBT-interferometer with the probe, denoted 9, is shown in Fig. 2.10. Here the probe is connected to the edge between contacts C and A, we emphasize that the results discussed below do not depend on to which edge-state the probe is connected.

The presence of the probe modifies the amplitudes for scattering from terminals 2, 3 to terminals 5 to 8. As an example, the scattering amplitude in Eq. (2.42) is modified

$$s_{52} = \sqrt{1 - \varepsilon} \sqrt{\mathcal{T}_A \mathcal{T}_C} e^{i(\phi_1 - \psi_1)}. \quad (2.53)$$

In addition, we also have to consider amplitudes for scattering into and out from the probe terminal 9. The average currents in the presence of dephasing, given from Eqs. (2.4)-(2.6) and (2.12), turn out to be given by the same equations as in the absence of dephasing, i.e. Eq. (2.43). This is what one expects, i.e. that dephasing affects only the phase-dependent parts of the observables.

Turning to the current correlators, given from Eqs. (2.8), (2.9) and (2.14), we find for the correlators between terminals 5 and 8

$$S_{58}^{dp} = \frac{-2e^2}{h} \left[ c_{0,58} \bar{S}_0 + \bar{c}_\Theta \bar{S}_\Theta \sqrt{1-\varepsilon} \cos\left(\frac{eV}{2E_c} + \Theta\right) \right] \quad (2.54)$$

and for the correlators between terminals 5 and 7

$$S_{57}^{dp} = \frac{-2e^2}{h} \left[ c_{0,57} \bar{S}_0 + \bar{c}_\Theta \bar{S}_\Theta \sqrt{1-\varepsilon} \cos\left(\frac{eV}{2E_c} + \Theta\right) \right]. \quad (2.55)$$

The two remaining correlators are again given by the substitutions  $S_{67} = S_{58}(\mathcal{T}_C \leftrightarrow \mathcal{T}_D)$  and  $S_{68} = S_{57}(\mathcal{T}_C \leftrightarrow \mathcal{T}_D)$ . We see from Eqs. (2.54) and (2.55) that just as for the MZ-interferometer, the only effect of dephasing is to suppress the phase-dependent term. The suppression factor is  $\sqrt{1-\varepsilon}$ , just the same as for the  $\cos\Theta$  term in the noise for the MZ-interferometer in Eq. (2.24).

We can thus directly write the visibilities in the presence of dephasing as

$$v_{N,HBT}^{\Theta,\alpha\beta,dp} = \sqrt{1-\varepsilon} v_{N,HBT}^{\Theta,\alpha\beta}. \quad (2.56)$$

This leads to the conclusion that the voltage probe for the HBT-interferometer, just as for the MZ-interferometer, just has the same effect as dephasing due to slow fluctuations of the phase  $\Theta$ , with the distribution of the phase fluctuations obeying the relation in Eq. (2.40). Moreover, the voltage probes have the same multiplicative property as for the MZ-interferometer, allowing one to describe the effect of a continuum of probes along the edges (of total length  $L = L_1 + L_2 + L_3 + L_4$ ) with a dephasing length  $L_\phi$ . The suppression of the visibilities of the  $h/e$

oscillations due to dephasing are then modified as  $(1 - \varepsilon)^{1/2} \rightarrow \exp(-L/2L_\phi)$ , just as for the  $h/e$  oscillations of the MZ-interferometer.

## 2.5 Summary

The MZ-interferometer is an amplitude interferometer: it exhibits a visibility in the average current with period  $h/e$  and exhibits a visibility in the shot noise with periods of both  $h/e$  and  $h/2e$ . In contrast, the HBT interferometer is an intensity interferometer; it exhibits no AB-effect in the current and exhibits only an  $h/e$ -effect in the shot noise correlations. Interestingly, our investigation shows that the shot noise visibility of the HBT interferometer as a function of temperature, voltage and dephasing rate, is qualitatively similar to that of the  $h/e$ -component of the shot noise of the MZ-interferometer. This is contrary to the naive expectation that the visibility of the two particle processes which lead to the HBT effect should be similar to the visibility of the two particle processes in the MZ-interferometer, that is the  $h/2e$  component of the shot noise. Instead it is the number of times the AB-flux is enclosed which determines the behavior of the visibility.

In this chapter we have shown the investigation and comparison in detail the voltage, temperature and asymmetry dependence for the current and noise visibilities in the MZ and HBT-interferometers. The experimental realization of the HBT-interferometer is of large importance since it allows for an unambiguous demonstration of two-particle interference effects with electrons, to date not demonstrated. Moreover, a successful realization of the HBT-interferometer would also enable a first demonstration of orbital entanglement in electrical conductors, a fundamentally important result. The results presented in this work should prove useful for the experimental work aiming to detect the HBT effect in electrical conductors.

## References

- [1] G. Seelig and M. Büttiker, “Charge-fluctuation-induced dephasing in a gated mesoscopic interferometer,” *Phys. Rev. B*, vol. 64, pp. 245313–245326, Dec. 2001.
- [2] G. Seelig, S. Pilgram, A.N. Jordan and M. Büttiker, “Probe-configuration-dependent dephasing in a mesoscopic interferometer,” *Phys. Rev. B*, vol. 68, pp. R161310–161314, Oct. 2003.
- [3] F. Marquardt and C. Bruder, “Influence of Dephasing on Shot Noise in an Electronic Mach-Zehnder Interferometer,” *Phys. Rev. Lett.*, vol. 92, pp. 56805–56809, Feb. 2004.
- [4] F. Marquardt and C. Bruder, “Effects of dephasing on shot noise in an electronic Mach-Zehnder interferometer,” *Phys. Rev. B*, vol. 70, pp. 125305–125320, Sep. 2004.
- [5] F. Marquardt, “Fermionic Mach-Zehnder interferometer subject to a quantum bath,” *Europhys. Lett.*, vol. 72, pp. 788–794, Dec. 2005.
- [6] H. Förster, S. Pilgram and M. Büttiker, “Decoherence and Full Counting Statistics in a Mach-Zehnder Interferometer,” *Phys. Rev. B*, vol. 72, pp. 075301–075310, Aug. 2005.
- [7] For an interesting historical account, see R. Hanbury Brown, *The Intensity Interferometer* (London: Taylor and Francis) 1974.
- [8] R. Hanbury Brown and R.Q. Twiss, *Philos. Mag. Ser.*, vol. 45, pp. 663, 1954.
- [9] R. Hanbury Brown and R.Q. Twiss, “Correlation between Photons in two Coherent Beams of Light,” *Nature (London)*, vol. 177, pp. 27–29, Jan. 1956.
- [10] R. Hanbury Brown and R.Q. Twiss, “A Test of a New Type of Stellar Interferometer on Sirius,” *Nature (London)*, vol. 178, pp. 1046–1048, Nov. 1956.

- [11] E.M. Purcell, “The Question of Correlation between Photons in Coherent Light Rays,” *Nature*, vol. 178, pp. 1449–1450, Dec. 1956.
- [12] R.Q. Twiss, A.G. Little, and R. Hanbury Brown, “Correlation Between Photons, in Coherent Beams of Light, Detected by a Coincidence Counting Technique,” *Nature (London)*, vol. 180, pp. 324–326, Aug. 1957.
- [13] G.A. Rebka, and R.V. Pound, “Time-Correlated Photons,” *Nature (London)*, vol. 180, pp. 1035–1036, Nov. 1957.
- [14] See e.g. R. Loudon, “Non-classical effects in the statistical properties of light,” *Rep. Prog. Phys.*, vol. 43, pp. 913–949, Jul. 1980.
- [15] G. Baym, “The Physics of Hanbury Brown--Twiss Intensity Interferometry: from Stars to Nuclear Collisions,” *Acta Phys. Pol. B*, vol. 29, pp. 1839–1884, Jul. 1998.
- [16] E. Brannen and H.I.S. Ferguson, “The Question of Correlation between Photons in Coherent Light Rays,” *Nature (London)*, vol. 178, pp. 481–482, Sep. 1956.
- [17] R. Hanbury Brown and R.Q. Twiss, “The Question of Correlation between Photons in Coherent Light Rays,” *Nature (London)*, vol. 178, pp. 1447–1448, Dec. 1956.
- [18] B. Yurke and D. Stoler, “Einstein-Podolsky-Rosen effects from independent particle sources,” *Phys. Rev. Lett.*, vol. 68, pp. 1251–1254, Mar. 1992.
- [19] B. Yurke and D. Stoler, “Bell’s-inequality experiments using independent-particle sources,” *Phys. Rev. A*, vol. 46, pp. 2229–2234, Sep. 1992.
- [20] K. v. Klitzing, G. Dorda, M. Pepper, “New Method for High-Accuracy Determination of the Fine-Structure Constant Based on Quantized Hall Resistance,” *Phys. Rev. Lett.*, vol. 45, pp. 494–497, Aug. 1980.
- [21] M. Büttiker, “Absence of backscattering in the quantum Hall effect in multiprobe conductors,” *Phys. Rev. B*, vol. 38, pp. 9375–9389, Nov. 1988.

- [22] B. I. Halperin, “Quantized Hall conductance, current-carrying edge states, and the existence of extended states in a two-dimensional disordered potential,” *Phys. Rev. B*, vol. 25, pp. 2185–2190, Feb. 1982.
- [23] B. J. van Wees, H. van Houten, C. W. J. Beenakker, J. G. Williamson, L. P. Kouwenhoven, D. van der Marel, and C. T. Foxon, “Quantized conductance of point contacts in a two-dimensional electron gas,” *Phys. Rev. Lett.*, vol. 60, pp. 848–850, Feb. 1988.
- [24] D. A. Wharam, T. J. Thornton, R. Newbury, M. Pepper, H. Ahmed, J. E. F. Frost, D. G. Hasko, D. C. Peacock, D. A. Ritchie and G. A. C. Jones, “One-dimensional transport and the quantisation of the ballistic resistance,” *J. Phys. C: Solid State Phys.*, vol. 21, pp. L209–L214, Mar. 1988.
- [25] W.D. Oliver, J. Kim, R.C. Liu, and Y. Yamamoto, “Hanbury Brown and Twiss-Type Experiment with Electrons,” *Science*, vol. 284, pp. 299–301, Apr. 1999.
- [26] H. Kiesel, A. Renz, and F. Hasselbach, “Observation of Hanbury Brown–Twiss anticorrelations for free electrons,” *Nature (London)*, vol. 418, pp. 392–394, Jul. 2002.
- [27] Y. Ji, Y. Chung, D. Sprinzak, M. Heiblum, D. Mahalu, and H. Shtrikman, “An electronic Mach–Zehnder interferometer,” *Nature*, vol. 422, pp. 415–418, Mar. 2003.
- [28] M. Henny, S. Oberholzer, C. Strunk, T. Heinzel, K. Ensslin, M. Holland and C. Schonenberger, “The Fermionic Hanbury Brown and Twiss Experiment,” *Science*, vol. 284, pp. 296–298, Apr. 1999.
- [29] S. Oberholzer, M. Henny, C. Strunk, C. Schonenberger, T. Heinzel, K. Ensslin, M. Holland, “The Hanbury Brown and Twiss experiment with fermions,” *Physica E*, vol. 6, pp. 314–317, Feb. 2000.

- [30] Ya. M. Blanter and M. Büttiker, “Shot noise in mesoscopic conductors ,” *Phys. Rep.*, vol. 336, pp. 1–166, Sep. 2000.
- [31] M. Büttiker, P. Samuelsson, E.V. Sukhorukov, “Entangled Hanbury Brown Twiss effects with edge states ,” *Physica E*, vol. 20, pp. 33–42, Dec. 2003.
- [32] P. Samuelsson, E.V. Sukhorukov, and M. Büttiker, “Orbital Entanglement and Violation of Bell Inequalities in Mesoscopic Conductors,” *Phys. Rev. Lett.*, vol. 91, pp. 157002–157005, Oct. 2003.
- [33] P. Samuelsson, E.V. Sukhorukov, and M. Büttiker, “Two-Particle Aharonov-Bohm Effect and Entanglement in the Electronic Hanbury Brown–Twiss Setup,” *Phys. Rev. Lett.*, vol. 92, pp. 26805–26808, Jan. 2004.
- [34] C.W.J. Beenakker, C. Emary, M. Kindermann, and J.L. van Velsen, “Proposal for Production and Detection of Entangled Electron-Hole Pairs in a Degenerate Electron Gas,” *Phys. Rev. Lett.*, vol. 91, pp. 147901–147904, Oct. 2003.
- [35] C.W.J. Beenakker, and M. Kindermann, “Quantum Teleportation by Particle-Hole Annihilation in the Fermi Sea,” *Phys. Rev. Lett.*, vol. 92, pp. 056801–056804, Feb. 2004.
- [36] P. Samuelsson, and M. Büttiker, “Dynamic generation of orbital quasiparticle entanglement in mesoscopic conductors,” *Phys. Rev. B*, vol. 71, pp. 245317–245321, Jun. 2005.
- [37] See also related work by C.W.J. Beenakker, M. Titov, B. Trauzettel, “Optimal Spin-Entangled Electron-Hole Pair Pump,” *Phys. Rev. Lett.*, vol. 94, pp. 186804–186807, May 2005; A. V. Lebedev, G. B. Lesovik, G. Blatter, “Generating spin-entangled electron pairs in normal conductors using voltage pulses,” *Phys. Rev. B*, vol. 72, pp. 245314–245321, Dec. 2005
- [38] T. M. Stace, C. H. W. Barnes, and G. J. Milburn, “Mesoscopic One-Way Channels for Quantum State Transfer via the Quantum Hall Effect,” *Phys. Rev.*



- Lett.*, vol. 93, pp. 126804–126807, Sep. 2004.
- [39] L. Saminadayar, D. C. Glattli, Y. Jin and B. Etienne, “Observation of the  $e/3$  Fractionally Charged Laughlin Quasiparticle,” *Phys. Rev. Lett.*, vol. 79, pp. 2526–2529, Sep. 1997.
- [40] R. de-Picciotto, M. Reznikov, M. Heiblum, V. Umansky, G. Bunin, D. Mahalu, “Direct observation of a fractional charge,” *Nature*, vol. 389, pp. 162–164, Sep. 1997.
- [41] I. Safi, P. Devillard, and T. Martin, “Partition Noise and Statistics in the Fractional Quantum Hall Effect,” *Phys. Rev. Lett.*, vol. 86, pp. 4628–4631, May 2001.
- [42] S. Vishveshwara, “Revisiting the Hanbury Brown–Twiss Setup for Fractional Statistics,” *Phys. Rev. Lett.*, vol. 91, pp. 196803–196806, Nov. 2003.
- [43] S.A. Kivelson and V.L. Pokrovsky, “Methods to measure the charge of the quasiparticles in the fractional quantum Hall effect,” *Phys. Rev. B*, vol. 40, pp. R1373–R1376, Jul. 1989.
- [44] C. de C. Chamon, D.E. Freed, S.A. Kivelson, S.L. Sondhi and X.G. Wen, “Two point-contact interferometer for quantum Hall systems,” *Phys. Rev. B*, vol. 55, pp. 2331–2343, Jan. 1997.
- [45] M.R. Geller and D. Loss, “Aharonov-Bohm effect in the chiral Luttinger liquid,” *Phys. Rev. B*, vol. 56, pp. 9692–9706, Oct. 1997.
- [46] T. Jonckheere, P. Devillard, A. Crepieux, Th. Martin, “Electronic Mach-Zehnder interferometer in the fractional quantum Hall effect,” *Phys. Rev. B*, vol. 72, pp. R201305–R201308, Nov. 2005.
- [47] T. Christen and M. Büttiker, “Gauge-invariant nonlinear electric transport in mesoscopic conductors,” *Europhys. Lett.*, vol. 35, pp. 523–528, Sep. 1996; M. Büttiker, “Capacitance, admittance, and rectification properties of small

- conductors,” *J. Phys.: Condensed Matter*, vol. 5, pp. 9361–9378, Dec. 1993.
- [48] M. Büttiker, “Four-Terminal Phase-Coherent Conductance,” *Phys. Rev. Lett.*, vol. 57, pp. 1761–1764, Oct. 1986.
- [49] M. Büttiker, “Scattering theory of thermal and excess noise in open conductors,” *Phys. Rev. Lett.*, vol. 65, pp. 2901–2904, Dec. 1990.
- [50] M. Büttiker, “Scattering theory of current and intensity noise correlations in conductors and wave guides,” *Phys. Rev. B*, vol. 46, pp. 12485–12507, Nov. 1992.
- [51] M. Büttiker, “Role of quantum coherence in series resistors,” *Phys. Rev. B*, vol. 33, pp. 3020–3026, Mar. 1986.
- [52] M. Büttiker, “Coherent and sequential tunneling in series barriers,” *IBM J. Res. Dev.*, vol. 32, pp. 63–75, Jan. 1988.
- [53] C.W.J. Beenakker, and M. Büttiker, “Suppression of shot noise in metallic diffusive conductors,” *Phys. Rev. B*, vol. 46, pp. 1889–1892, Jul. 1992.
- [54] M. J. M. de Jong, and C. W. J. Beenakker, “Semiclassical theory of shot noise in mesoscopic conductors,” *Physica A*, vol. 230, pp. 219–248, Aug. 1996.
- [55] S. A. van Langen, and M. Büttiker, “Quantum-statistical current correlations in multilead chaotic cavities,” *Phys. Rev. B*, vol. 56, pp. R1680–R1683, Jul. 1997.
- [56] C. Texier and M. Büttiker, “Effect of incoherent scattering on shot noise correlations in the quantum Hall regime,” *Phys. Rev. B*, vol. 62, pp. 7454–7458, Sep. 2000.
- [57] A.A. Clerk and A.D. Stone, “Noise and measurement efficiency of a partially coherent mesoscopic detector,” *Phys. Rev. B*, vol. 69, pp. 245303–245316, Jun. 2004.
- [58] C.W.J. Beenakker and B. Michaelis, “Stub model for dephasing in a quantum dot,” *J. Phys. A: Math. Gen.*, vol. 38, pp. 10639–10646, Dec. 2005.

- [59] D. B. Chklovskii, B. I. Shklovskii and L. I. Glazman, “Electrostatics of edge channels,” *Phys. Rev. B*, vol. 46, pp. 4026–4034, Aug. 1992; N. R. Cooper and J. T. Chalker, “Coulomb interactions and the integer quantum Hall effect: Screening and transport,” *Phys. Rev. B*, vol. 48, pp. 4530–4544, Aug. 1993.
- [60] H. A. Fertig, “Semiclassical description of a two-dimensional electron in a strong magnetic field and an external potential,” *Phys. Rev. B*, vol. 38, pp. 996–1015, Jul. 1988.
- [61] See e.g. the discussion in N. C. van der Vaart, M. P. de Ruyter van Steveninck, L. P. Kouwenhoven, A. T. Johnson, Y. V. Nazarov, C. J. P. M. Harmans, and C. T. Foxon, “Time-Resolved Tunneling of Single Electrons between Landau Levels in a Quantum Dot,” *Phys. Rev. Lett.*, vol. 73, pp. 320–323, Jul. 1994, and references therein.
- [62] D. Sanchez and M. Büttiker, “Magnetic-Field Asymmetry of Nonlinear Mesoscopic Transport,” *Phys. Rev. Lett.*, vol. 93, pp. 106802–106805, Sep. 2004; T. Christen and M. Büttiker, “Low-frequency admittance of quantized Hall conductors,” *Phys. Rev. B*, vol. 53, pp. 2064–2072, Jan. 1996.
- [63] I. Neder, M. Heiblum, Y. Levinson, D. Mahalu, and V. Umansky, “Unexpected Behavior in a Two-Path Electron Interferometer,” *Phys. Rev. Lett.*, vol. 96, pp. 016804–016807, Jan. 2006.
- [64] L. V. Litvin, H.-P. Tranitz, W. Wegscheider, and C. Strunk, “Decoherence and single electron charging in an electronic Mach-Zehnder interferometer,” *Phys. Rev. B*, vol. 75, pp. 033315–033318, Jan. 2007.
- [65] S. Pilgram, P. Samuelsson, H. Förster, and M. Büttiker, “Full-Counting Statistics for Voltage and Dephasing Probes,” *Phys. Rev. Lett.*, vol. 97, pp. 066801–066804, Aug. 2006.
- [66] H. Förster, P. Samuelsson, S. Pilgram, and M. Büttiker, “Voltage and dephasing

probes: a full counting statistics discussion,” *Phys. Rev. B*, vol. 75, pp. 035340–035456, Jan. 2007.

- [67] Preden Roulleau, F. Portier, D. C. Glattli, P. Roche G. Gaini, U. Gennser, D. Maily,” High visibility in an electronic Mach-Zehnder interferometer with random phase fluctuations,” cond-mat\0704.0746, April, 2007.



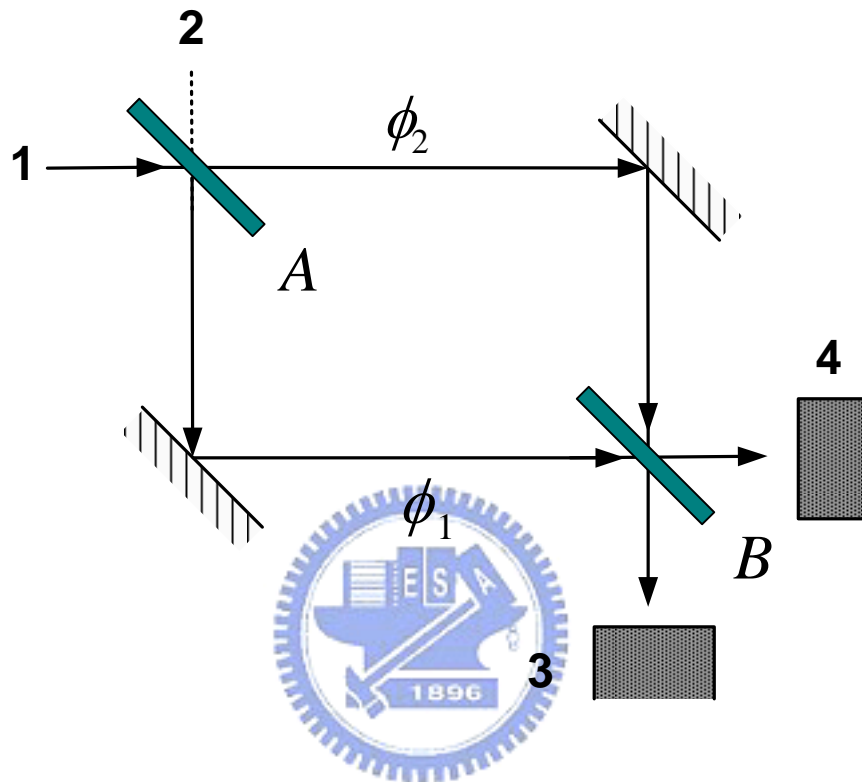


Fig. 2.1 An optical Mach-Zehnder interferometer. A beam of light incident from 1 is split in two partial beams at the semitransparent beam splitter A. The two partial beams acquire geometrical phases  $\phi_1$  and  $\phi_2$  respectively and are rejoined at the second beam splitter B. The light intensity is measured in detectors 3 and 4.

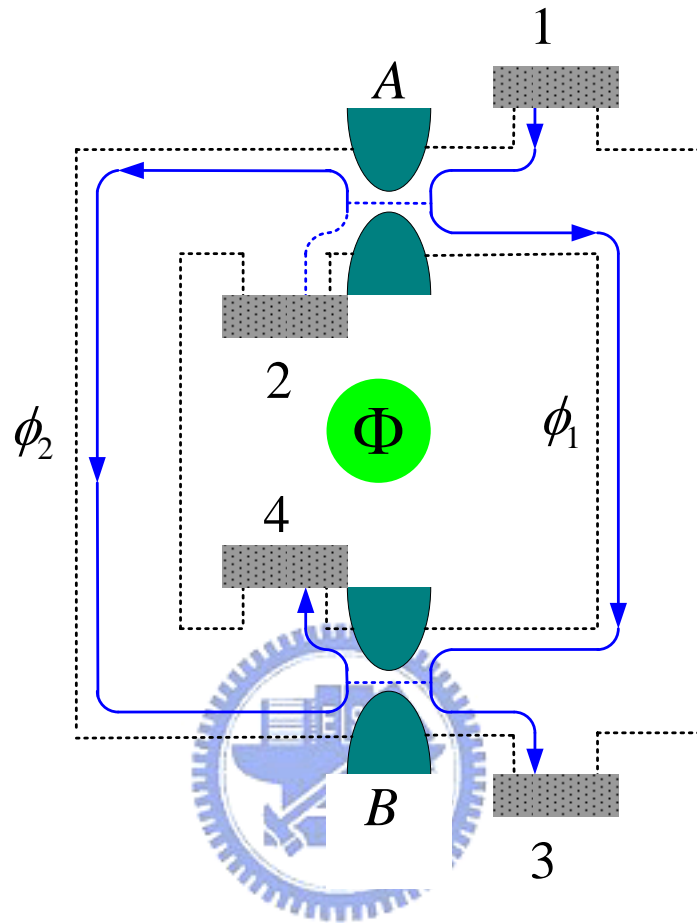


Fig. 2.2 The electronic analog of the MZ-interferometer, implemented by Ji et al. [27] in a conductor in the Quantum Hall regime. The electronic reservoir 1 is biased at  $eV$  and reservoirs 2 to 4 are kept at ground. The edge states (solid lines) have a direction of transport indicated by arrows. The QPC's  $A$  and  $B$  play the role of the beam splitters in Fig. 2.1. Geometrical phases  $\phi_1$  and  $\phi_2$  and the AB-flux  $\Phi$  are shown.

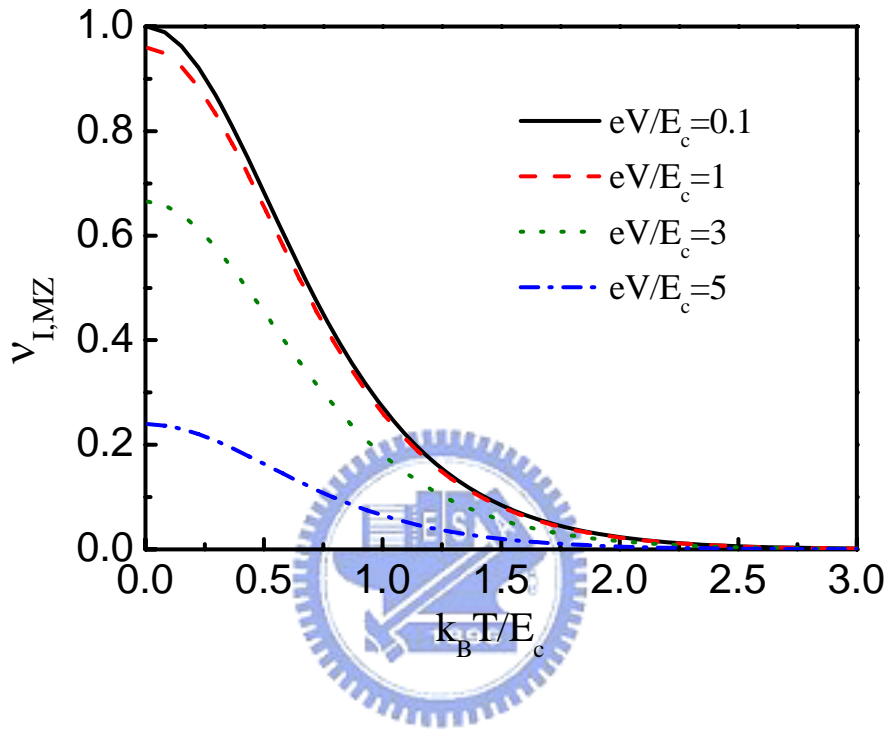


Fig. 2.3 Current visibility of the Mach-Zehnder interferometer  $V_{I,MZ}$  versus normalized temperature  $k_B T / E_c$  for  $\mathcal{T}_A = \mathcal{T}_B$ .

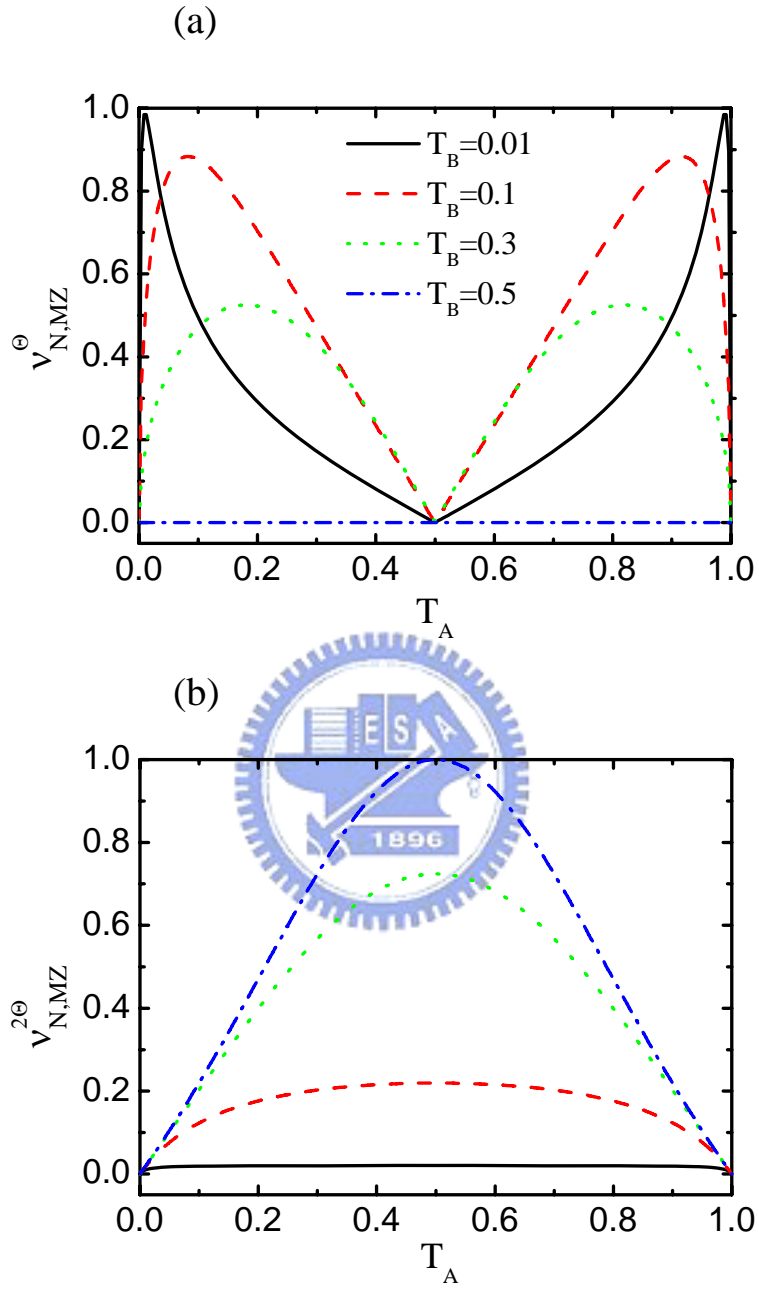


Fig. 2.4 Noise visibility  $v_{N,MZ}^{\Theta}$  [figure (a)] of the  $h/e$  and  $v_{N,MZ}^{2\Theta}$  [figure (b)] of the  $h/2e$  oscillations in the shot noise of the Mach-Zehnder interferometer versus transmission  $T_A$  of beam splitter A for  $E_c \gg k_B T, eV$  for various transmission probabilities  $T_B$  of beam splitter B .



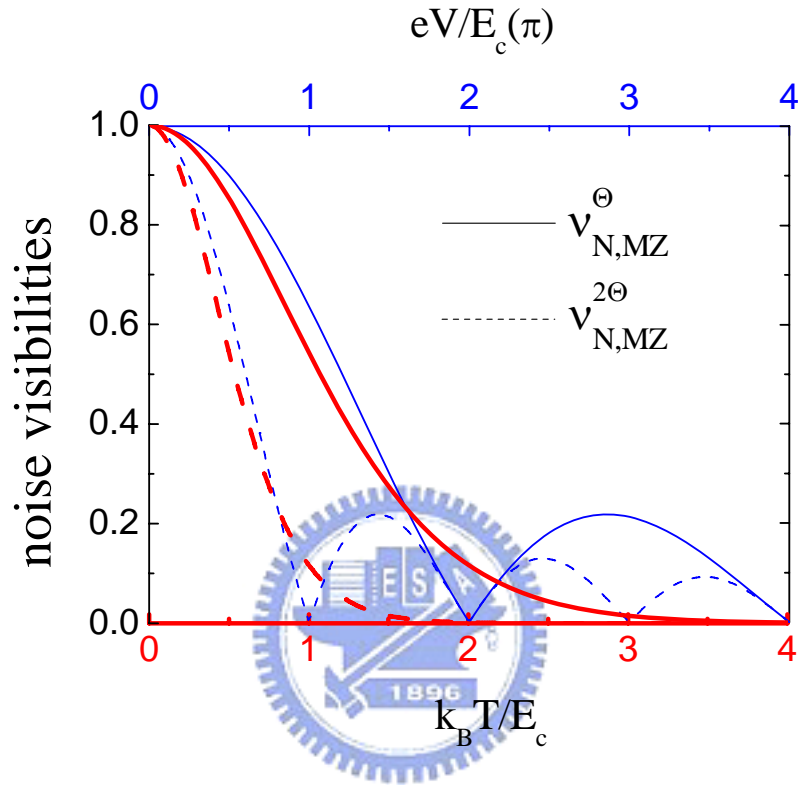


Fig. 2.5 Noise visibilities  $v_{N,MZ}^{\Theta}$  (for  $T_A, T_B \ll 1$ ) of the  $h/e$  and  $v_{N,MZ}^{2\Theta}$  of the  $h/2e$  oscillations in the shot noise correlation of a Mach-Zehnder interferometer for  $T_A = T_B = 1/2$  versus  $k_B T/E_c$  for  $eV \ll k_B T, E_c$  (red, thick curve) and versus  $eV/E_c$  for  $k_B T \ll E_c$ ,  $eV$  (blue, thin curve).

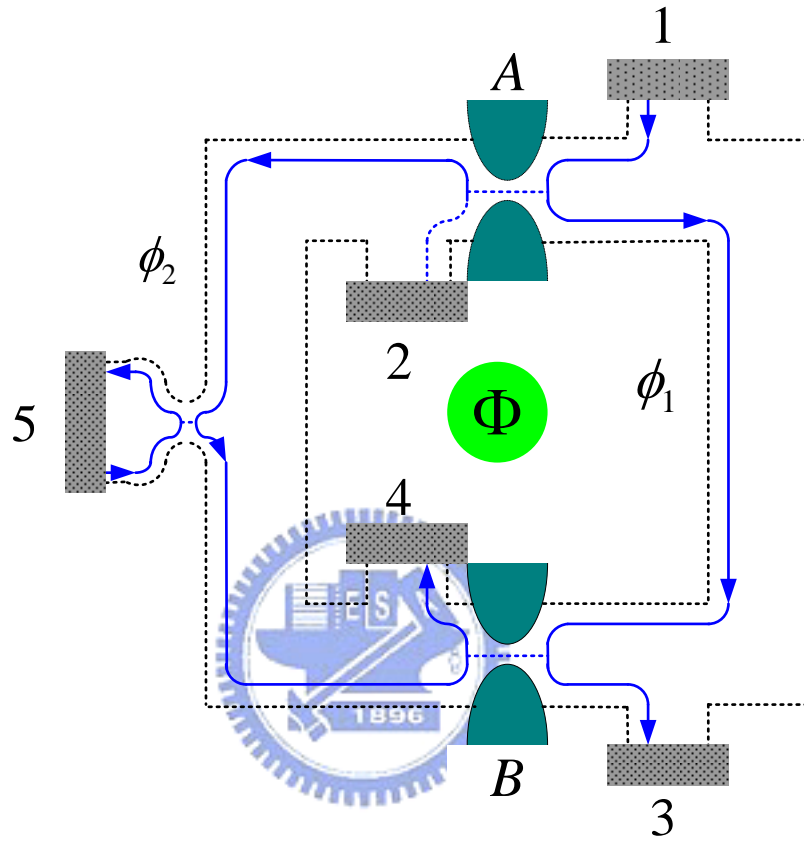


Fig. 2.6 The electrical MZ-interferometer, Fig. 2.2, with a dephasing voltage probe, 5, attached along one edge.

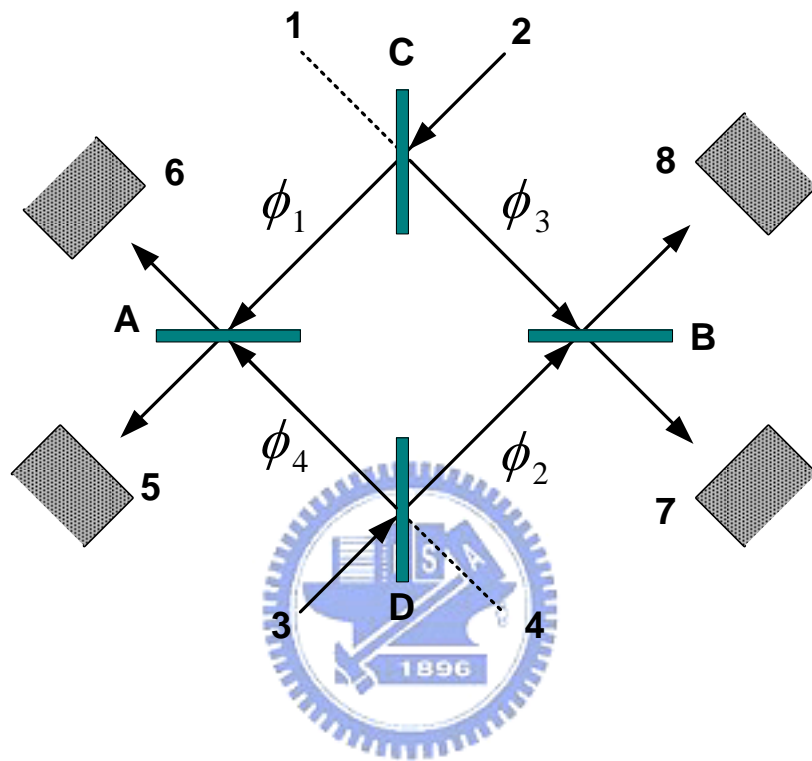


Fig. 2.7 Two-source, four-detector optical Hanbury Brown Twiss geometry proposed in Ref. [33]. Two beams of light incident from 2 and 3 are split in partial beams at the semitransparent beam splitters C and D. The partial beams acquire geometrical phases  $\phi_1$  to  $\phi_4$  and are rejoined in the beam splitters A and B. The light intensity is measured in detectors 5 to 8

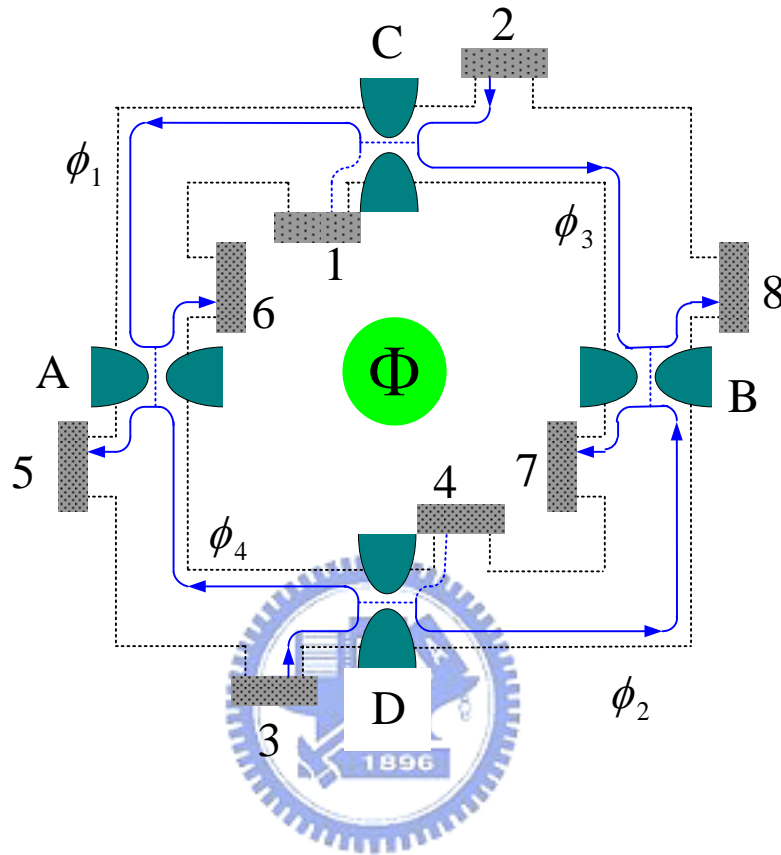


Fig. 2.8 Two-source, four-detector electrical Hanbury Brown Twiss geometry implemented in a conductor in the Quantum Hall regime. The electronic reservoirs 2 and 3 biased at  $eV$  and reservoirs 1 and 4 to 8 are kept at ground. The edge states (solid lines) have a direction of transport indicated by arrows. The QPC's  $A$  and  $B$  play the role of the beam splitters in Fig. 2.7. Geometrical phases  $\phi_1$  to  $\phi_4$  and the AB-flux  $\Phi$  are shown.

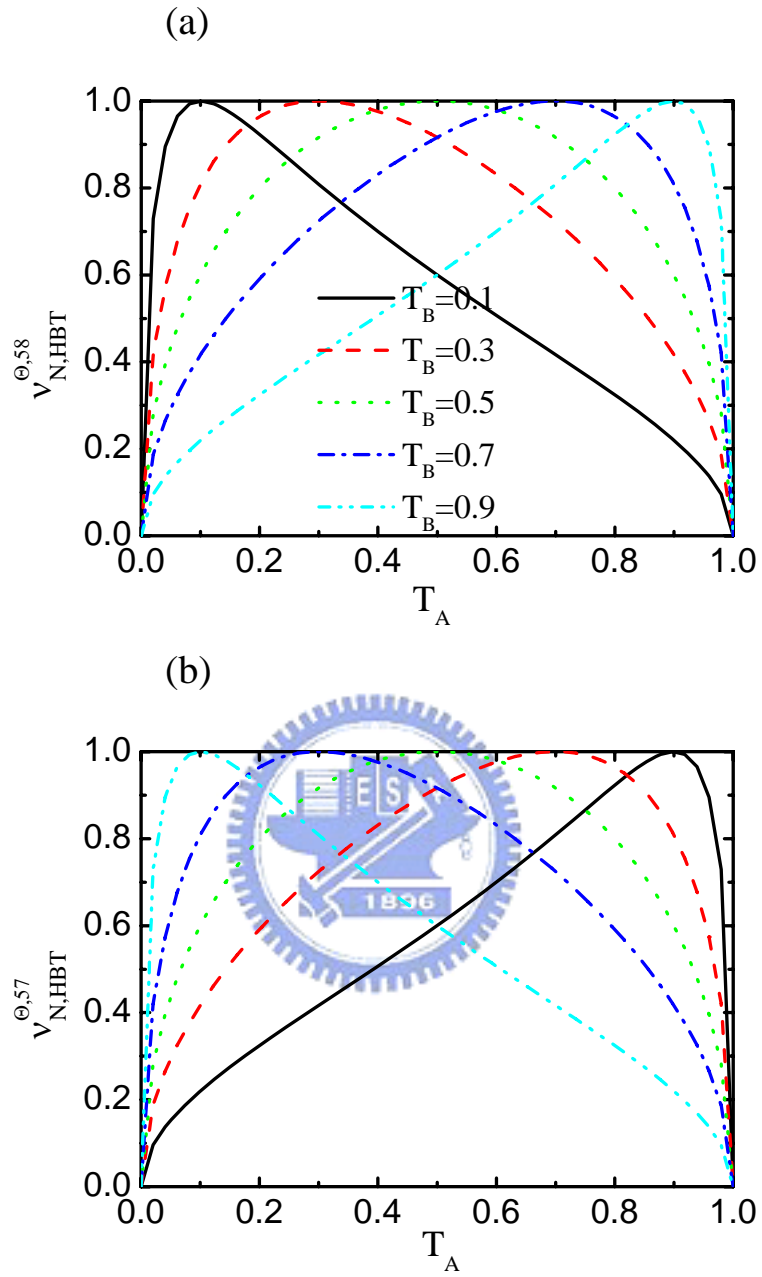


Fig. 2.9 Noise visibilities  $v_{N,HBT}^{\Theta,58}$  and  $v_{N,HBT}^{\Theta,57}$  of shot noise correlations in the HBT geometry versus transmission probability  $T_A$  for various values of  $T_B$ . A symmetric geometry,  $E_c \gg kT, eV$ , and identical QPC's C and D are considered.

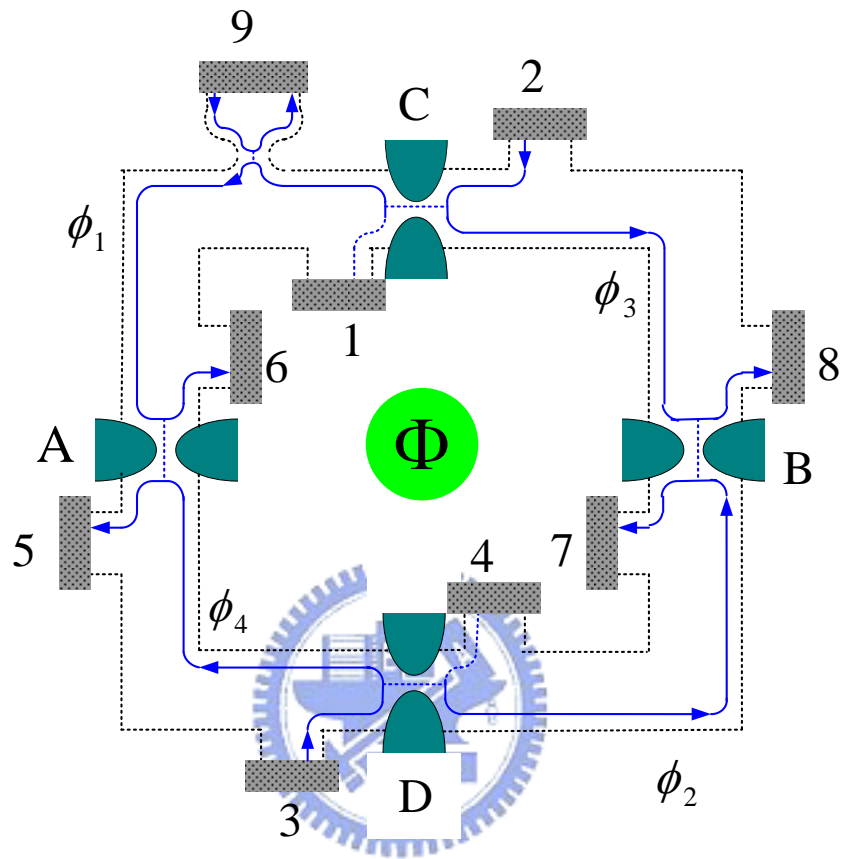


Fig. 2.10 The electrical HBT-interferometer, Fig. 2.8, with a dephasing voltage probe,  $9$ , attached along one edge.

## Chapter 3

# Quantum pump driven fermionic Mach-Zehnder interferometer

### 3.1 Introduction of quantum pump effects

The quantum pump effects have been caught a lot of attentions since the first experiment was realized by Switkes et al. [1]. The quantum pump effects indicate the currents are generated in a conductor without bias but perturbed by some external time-dependent potentials. In Ref. [1], a grounded quantum dot patterned in two dimensional electron gases (2DEG) by metal gates were modulated by two AC gates, which were kept the same frequency but differed by a constant phase  $\phi$ . Thus, the shape of the quantum dot was alternated adiabatically by time. The generated dc potential drops between two reservoirs were measured instead of detecting dc currents. The sinusoidal behavior of the potential drops with the phase  $\phi$  was qualitatively similar to the prediction of theory by Brouwer [2].

After that, the various investigations of theoretical aspects in quantum pumping were carried out, a representative collection found in Refs. [3-20]. However, contrary to the even magnetic field symmetry of the measurements of Ref. [1], the results of theoretical studies revealed no definite magnetic field symmetry for the pumped currents. The possible modifications resulted from rectification effects were suggested by Brouwer [21]. Soon, DiCarlo et al. [22] show indeed the rectification effects could dominate in the adiabatic regime, while the pure pumping effects were obviously given in the non-adiabatic regime.

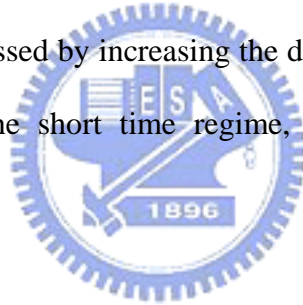
In this chapter, the investigations are shown the properties of the currents in a pump driven MZI. In contrast to the voltage driven setup, the currents are created via the quantum pump effects. Working in the adiabatic, low frequency regime, the system is kept close to equilibrium and the effects of the dephasing are minimized. The true quantum effects of the currents and the elementary structure of the MZI make it a promising candidate for a quantum pump. Previous studies of pumping in mesoscopic interferometers have concerned Aharonov-Bohm, [16, 23, 24] double slit-quantum dot [15] and two-particle [25] interferometers, however, to the best of our knowledge, not MZIs.

We use a Floquet scattering approach to the quantum pump problem. [26-28] This allows us to calculate the currents in the MZI for arbitrary pumping strength, frequency and temperature. In the Floquet picture, currents arise due to photon assisted interference. It is found that the pumped current contains both an Aharonov Bohm flux dependent part  $I^{(\Phi)}$ , due to interfering paths enclosing the flux, and a flux independent part  $I^{(0)}$ . Both current parts depend linearly on the pump frequency in the low frequency, adiabatic regime and show oscillations as a function of frequency in the high frequency, non-adiabatic regime. The oscillations in the non-adiabatic regime occur on two different frequency scales, governed by the interferometer arm length difference and the mean arm length respectively. For the flux dependent current  $I^{(\Phi)}$ , the oscillations have a constant amplitude while the amplitude of the  $I^{(0)}$  oscillations increases linearly with frequency. The two current parts also display a different dependence on temperature; the flux independent part is insensitive to temperature while the flux dependent part is monotonically suppressed with increasing temperature.

In the experiments in Refs. [1, 22] rectification effects made it difficult to distinguish the pumped current. Importantly, in the MZI it is found that in the regime



of low amplitude, adiabatic pumping, rectification effects [21] are absent for semitransparent beam-splitters. In order to investigate the effect of dephasing on the pumped current, we consider one of the interferometer arms connected to a voltage probe. Electrons injected into the probe scatter inelastically and hence lose phase coherence before being emitted out of the probe again. Two limiting regimes of the charge relaxation, or RC, time of the voltage probe compared to the pump period are considered; the long relaxation time regime, where the potential of the probe is constant during the measurement, and the short relaxation time regime where the potential of the probe adjusts instantaneously in order to keep zero time dependent current at the probe. In the long time regime the flux dependent current  $I^{(\Phi)}$  as well as the part of the flux independent  $I^{(0)}$  flowing in the arm connected to the probe are successively suppressed by increasing the dephasing, i.e. the strength of the coupling to the probe. In the short time regime, only  $I^{(\Phi)}$  is suppressed by dephasing.



## 3.2 Theory and Model

### 3.2.1 Floquet scattering approach

For completeness we first briefly review the Floquet scattering approach to pumping in mesoscopic conductors. [26, 27] A mesoscopic system connected to  $N$  reservoirs via single channel leads is considered. The system is perturbed by some time-dependent parameters which all vary with the same frequency  $\omega$ . The current flowing in the system in response to the time-periodic perturbation is periodic in time. Expanding the current  $I_\alpha(t)$  at reservoir  $\alpha$  into a Fourier series, we have

$$\begin{aligned}
I_\alpha(t) &= \sum_{l=-\infty}^{\infty} \exp(-il\omega t) I_{\alpha,l}, \\
I_{\alpha,l} &= \int_0^T \frac{dt}{T} \exp(il\omega t) I_\alpha(t),
\end{aligned} \tag{3.1}$$

where  $T = 2\pi/\omega$  is the period of the oscillations. The Fourier component  $I_{\alpha,l}$  can be written [29]

$$I_{\alpha,l} = \frac{e}{h} \int_0^\infty dE \left[ \langle \hat{b}_\alpha^\dagger(E) \hat{b}_\alpha(E_l) \rangle - \langle \hat{a}_\alpha^\dagger(E) \hat{a}_\alpha(E_l) \rangle \right], \tag{3.2}$$

with  $\langle \dots \rangle$  denoting a quantum statistical average. Here  $E_l = E + l\hbar\omega$  and  $\hat{b}_\alpha(E)$  and  $\hat{a}_\alpha(E)$  are annihilation operators for particles coming into and going out from the reservoirs respectively. The operators  $\hat{b}_\alpha(E)$  and  $\hat{a}_\alpha(E)$  are related via the Floquet scattering matrix  $s_F$  as

$$\hat{b}_\alpha(E) = \sum_{\beta=1}^N \sum_{n=-\infty}^{\infty} s_{F,\alpha\beta}(E, E_n) \hat{a}_\beta(E_n), \tag{3.3}$$

where the element  $s_{F,\alpha\beta}(E, E_n)$  is the amplitude for scattering of an electron from reservoir  $\beta$  at energy  $E_n$  to reservoir  $\alpha$  and energy  $E$ . All the reservoirs are in thermal equilibrium, giving the average

$$\langle \hat{a}_\alpha^\dagger(E_n) \hat{a}_\beta(E_m) \rangle = f_\alpha(E_n) \delta_{\alpha\beta} \delta_{nm}, \tag{3.4}$$

where  $f_\alpha(E_n) = \{1 + \exp[E_n / k_B T_\alpha]\}^{-1}$  is the Fermi distribution function with  $T_\alpha$  the temperature of reservoir  $\alpha$  and  $k_B$  is the Boltzmann constant.

Substituting Eq. (3.3) into Eq. (3.2) and taking into account the unitarity of the Floquet scattering matrix, [27]

$$\sum_{\beta=1}^N \sum_{n=-\infty}^{\infty} s_{F,\alpha\beta}^*(E, E_n) s_{F,\gamma\beta}(E_l, E_n) = \delta_{l,0} \delta_{\alpha,\gamma}, \tag{3.5}$$

we can, with Eq. (3.4), rewrite Eq. (3.2) as

$$I_{\alpha,l} = \frac{e}{h} \int_{-\infty}^{\infty} dE \sum_{\beta=1}^N \sum_{n=-\infty}^{\infty} [f_{\beta}(E) - f_{\alpha}(E_n)] \times s_{F,\alpha\beta}^*(E_n, E) s_{F,\alpha\beta}(E_{n+l}, E). \quad (3.6)$$

Note that to get the above equation we have, compared to Eq. (3.3), made the shift  $E_n \rightarrow E$ . At  $l = 0$  the equation (3.6) defines a dc current

$$I_{\alpha,dc} = \frac{e}{h} \int_{-\infty}^{\infty} dE \sum_{\beta=1}^N \sum_{n=-\infty}^{\infty} |s_{F,\alpha\beta}(E_n, E)|^2 \times [f_{\beta}(E) - f_{\alpha}(E_n)]. \quad (3.7)$$

### 3.2.2 Mach Zehnder interferometer

We consider a pump-driven Mach-Zehnder interferometer (MZI) implemented in a conductor in the quantum Hall regime, as shown in Fig. 3.1. Transport takes place along a single edge state (filling factor one) and is unidirectional. Two electrostatic split gates  $A$  and  $B$ , defining quantum point contacts (QPCs)  $j = A, B$ , are subjected to time dependent potentials  $V_j(t, \phi_j) = V_{sj} + V_j \cos(\omega t + \phi_j)$  with  $\phi_j$  the pumping phase. The pumping potentials give rise to scattering of electrons between the edges as well as absorption or emission of one or several quanta of energy  $\hbar\omega$ . An Aharonov-Bohm flux  $\Phi$  penetrates the interior of the interferometer. The conductor is connected to four electronic reservoirs  $\alpha = 1$  to  $4$ . All four reservoirs are kept at the same potential (grounded) and temperature  $T_{\alpha} = T$ . Thus, the Fermi distribution functions for all the reservoirs are the same,  $f_{\alpha}(E) = f_0(E)$ , and in the absence of the pumping potentials there is no current flow.

The scattering at the QPCs A and B, taking place both in real space and in energy space, can be described by the Floquet scattering matrices

$$S_j(E_n, E_m) = \begin{pmatrix} r_j(E_n, E_m) & t'_j(E_n, E_m) \\ t_j(E_n, E_m) & r'_j(E_n, E_m) \end{pmatrix}, \quad (3.8)$$

with primed amplitudes for particles incident on the QPCs from left in Fig. 3.1. The QPCs thus act as inelastic beam splitters. We consider the scattering amplitudes to be independent on energy on the scale of the pump frequency. Consequently,  $S_j(E_n, E_m) \equiv S_{j,n-m}(E)$  can be expressed in terms of the Fourier coefficients for the corresponding frozen scattering matrix [30]  $S_j(E, t)$  as

$$S_{j,n-m}(E) = \int_0^T \frac{dt}{T} e^{i(n-m)\omega t} S_j(E, t). \quad (3.9)$$

Moreover, it is assumed that the scale of the energy dependence of the QPC scattering amplitudes is much larger than the thermal energy  $k_B T$ , allowing us to neglect the energy dependence of the Floquet scattering matrix of the QPCs all together,  $S_{j,n-m}(E) = S_{j,n-m}$ .

Propagating ballistically along the edges between the QPCs the electrons pick up a phase containing both a geometrical part  $k_m L_i$  and a part  $\psi_i$  due to the Aharonov-Bohm flux, with  $i = L, R$ . Here  $\psi_L + \psi_R = 2\pi\Phi/\Phi_0$  where  $\Phi_0 = h/e$  is the flux quantum. It is assumed that the wavenumber  $k_m = k(E_m)$  can be taken linear in energy, [31, 32]

$$k_m L_i = \zeta_i(\mu) + \frac{L_i}{\hbar v_D} (E + m\hbar\omega), \quad (3.10)$$

where  $\zeta_i(\mu)$  is the accumulated phase at the Fermi energy and  $v_D$  the drift velocity of the edge states. The lengths of the interferometer arms are  $L_L$  and  $L_R$  respectively, where we without loss of generality take  $L_L \geq L_R$ . The total Floquet scattering amplitude can thus be expressed in terms of the scattering amplitudes of the QPCs and the phases acquired along the interferometer arms. For scattering from energy  $E$  at reservoir 1 to energy  $E_n$  at reservoir 3 the amplitude is

$$s_{F,31}(E_n, E) = \sum_{m=-\infty}^{\infty} \left[ r_{B,n-m} e^{ik_m L_R - i\psi_R} r_{A,m} + t'_{B,n-m} e^{ik_m L_L + i\psi_L} t_{A,m} \right] \quad (3.11)$$

and similarly for the other amplitudes. Inserting these scattering amplitudes into Eq. (3.7) we arrive at the expression for the dc current.

To perform an analysis of the entire parameter space, in the plots we model for simplicity the QPC potentials with oscillating delta function potentials

$$V_j(t, \phi_j) = \delta(x)(V_{sj} + 2V_j \cos(\omega t + \phi_j)). \quad (3.12)$$

We note that this choice leads to completely symmetric scattering matrices,  $t_{j,n} = t'_{j,n}$  and  $r_{j,n} = r'_{j,n}$ . It is pointed out explicitly in the text below where this additional symmetry qualitatively affects the result. The frozen scattering amplitudes of the QPCs are given by

$$t_j(t, \phi_j) = \frac{1}{1 + im_e/(\hbar^2 k_\mu)[V_{sj} + 2V_j \cos(\omega t + \phi_j)]}, \quad (3.13)$$

and  $r_j(t, \phi_j) = t_j(t, \phi_j) - 1$ , with  $m_e$  the effective electron mass and  $k_\mu$  the wavenumber at the Fermi energy. Note that Eq. (3.13) is valid as the passing time of electrons at the QPCs are much smaller than the pump period. This gives from Eq.

(3.9) the Fourier coefficients

$$\begin{aligned} t_{j,n} &= \frac{e^{-in\phi_j}}{\sqrt{[1 + ia_j]^2 + b_j^2}} \\ &\times \left\{ \frac{i}{b_j} \left[ 1 + ia_j - \sqrt{(1 + ia_j)^2 + b_j^2} \right] \right\}^{|n|}, \\ r_{j,n} &= t_{j,n} - \delta_{n,0}, \end{aligned} \quad (3.14)$$

with  $a_j = V_{sj}m_e/(\hbar^2 k_\mu)$  and  $b_j = 2V_jm_e/(\hbar^2 k_\mu)$ .

### 3.3 Pumped current

In the Floquet scattering picture, the pumping current arises due to interference between different paths of the electrons in energy space, i.e. photon-assisted interference. [33] Due to the absence of closed orbits in the MZI, there are only two different types of interfering paths; the two paths either go along the same interferometer arm, L or R, or along different arms. The latter paths enclose the flux  $\Phi$  in and give rise to an Aharonov-Bohm effect in the pumped current. In Fig. 3.2 different interfering paths contributing to the current are shown. We note that an Aharonov-Bohm effect in the pumped current was also predicted for other interferometers. [15, 16, 23, 24]

It is thus natural to part the total current into a flux dependent and a flux independent part. Focusing on the current at reservoir 3, we write

$$I_{3,dc} = I_3^{(0)} + I_3^{(\Phi)}. \quad (3.15)$$

Inserting the scattering amplitudes in Eq. (3.11) into the current expression Eq. (3.7) and carrying out the energy integrals we arrive at the flux independent part

$$\begin{aligned} I_3^{(0)} = & \frac{e\omega}{2\pi} \sum_{n=-\infty}^{\infty} \sum_{m=-\infty}^{\infty} \sum_{p=-\infty}^{\infty} n \\ & \times \left\{ \left( r_{A,m} r_{A,p}^* + t_{A,m}' t_{A,p}'^* \right) t_{B,n-m}' t_{B,n-p}'^* \right. \\ & \times \exp \left[ i\omega(m-p) \left( \tau + \frac{\hbar}{2E_c} \right) \right] \\ & + \left( r_{A,m}' r_{A,p}^{l*} + t_{A,m} t_{A,p}^* \right) r_{B,n-m} r_{B,n-p}^* \\ & \left. \times \exp \left[ i\omega(m-p) \left( \tau - \frac{\hbar}{2E_c} \right) \right] \right\} \end{aligned} \quad (3.16)$$

and the flux dependent part

$$\begin{aligned}
I_3^{(\Phi)} &= \frac{2eE_c}{h} g(T) \sum_{n=-\infty}^{\infty} \sum_{m=-\infty}^{\infty} \sum_{p=-\infty}^{\infty} \sin\left(\frac{n\hbar\omega}{2E_c}\right) \\
&\times 2\Re \left\{ r_{B,n-m} t_{B,n-p}^{\prime*} \left( r_{A,m} t_{A,p}^* + t_{A,m}^{\prime} r_{A,p}^{\prime*} \right) \right. \\
&\times \left. \exp\left[ i\left( \psi_{LR} + \omega \left[ (m-p)\tau + (n-p-m)\frac{\hbar}{2E_c} \right] \right) \right] \right\},
\end{aligned} \tag{3.17}$$

where

$$g(T) = \frac{\pi k_B T}{E_c} \left( \frac{\pi k_B T}{E_c} \right), \tag{3.18}$$

the phase  $\psi_{LR} = \zeta_L(\mu) - \zeta_R(\mu) - 2\pi\Phi/\Phi_0$  and  $\Re$  denoting the real part.

In order to explicitly display the relevant energy and time scales we have introduced the asymmetry energy  $E_c = \hbar v_D/(L_L - L_R)$  and the average time  $\tau = (L_L + L_R)/(2v_D)$  for ballistic propagation between the QPCs. By definition  $\tau > \hbar/(2E_c)$ . There are thus three different, possible pumping regimes depending on the relation between the pump frequency  $\omega$  and the frequency scales  $E_c/\hbar$  and  $1/\tau$ : (i) For  $\omega \ll 1/\tau$  the pumping is adiabatic, the total scattering amplitudes of the MZI are independent on energy on the scale of the pumping frequency  $\omega$ . For non-adiabatic pumping there are in addition two regimes. (ii) In the intermediate frequency regime  $1/\tau \ll \omega \ll E_c/\hbar$  the pumped current is independent on the interferometer asymmetry but depends on the total time  $\tau$ . (iii) For  $E_c/\hbar \ll \omega$ , in the high frequency regime, the pumped current depends both on the asymmetry and the total time.

Several important observations can be made directly from the formal expressions in Eqs. (3.16) and (3.17). First, the flux independent current  $I_3^{(0)}$  is an incoherent sum of the currents pumped through the left and right arms. The two currents are denoted  $I_{3L}^{(0)}$  [upper term in Eq. (3.16)] and  $I_{3R}^{(0)}$  (lower term) respectively. Each current term,  $I_{3L}^{(0)}$  or  $I_{3R}^{(0)}$ , depends explicitly on the time for ballistic

propagation through the corresponding left or right arm,  $\tau + \hbar/(2E_c) = L_L/v_D$  and  $\tau - \hbar/(2E_c) = L_R/v_D$ . For the flux dependent current, no such partitioning into left and right arm currents is possible.

Second, while the flux independent current  $I_3^{(0)}$  is independent on the temperature, the flux dependent current  $I_3^{(\Phi)}$  is monotonically suppressed with increasing temperature. Despite the fact that both terms are of interference nature, they thus depend on temperature in very different ways. The energy scale of the decay of  $I_3^{(\Phi)}$  is set by the asymmetry energy  $E_c$ : the factor  $g(T)$  is equal to unity for  $k_B T \ll E_c$  and decays as  $\exp(-\pi k_B T/E_c)$  for  $k_B T \gg E_c$ . This is qualitatively similar to the voltage biased MZI [31] and can be understood as an effect of energy averaging. Notably, the temperature dependence of the current is affected neither by the pumping frequency  $\omega$  nor by the average time  $\tau$ .

Third, the qualitative behavior of the currents as a function of frequency can also be understood from Eqs. (3.16) and (3.17). It is clear that both currents  $I_3^{(0)}$  and  $I_3^{(\Phi)}$  show oscillations in the non-adiabatic regime as a function of  $\omega$ , on the scales  $E_c/\hbar$  and  $1/\tau$ . In the intermediate frequency regime (ii), for  $1/\tau \ll \omega \ll E_c/\hbar$ , the pumped current is however insensitive to the asymmetry and shows oscillations with the basic period  $\tau$  only. In regime (iii), for  $E_c/\hbar \ll \omega$ , the pumped current shows oscillations as a function of frequency on both the scales  $1/\tau$  and  $E_c/\hbar$ . For a small asymmetry,  $E_c \gg \hbar/\tau$ , the oscillations show a beating pattern with rapid oscillations on the scale  $1/\tau$  periodically modulated in amplitude on the scale  $E_c/\hbar$ . This is illustrated in the plots in Fig. 3.3. We point out that for the flux independent current  $I_3^{(0)}$  the beating pattern can simply be



understood as the effect of adding the two currents terms  $I_{3L}^{(0)}$  and  $I_{3R}^{(0)}$  with the two different time periods  $\tau \pm \hbar/(2E_c)$ .

Importantly, the amplitudes of the oscillations of  $I_3^{(0)}$  and  $I_3^{(\Phi)}$  show a different frequency dependence. As is clear from Eq. (3.16), in the high frequency regime,  $E_c/\hbar \ll \omega$ , the flux independent current is proportional to  $\omega$  while the flux dependent current has no frequency dependent prefactor. Plotting the currents divided by the elementary pumped current  $I_0 = e\omega/2\pi$ , the oscillations of the normalized current  $I_3^{(0)}/I_0$  have a constant amplitude as a function of frequency while the amplitude of  $I_3^{(\Phi)}/I_0$  decreases as  $1/\omega$ . This is illustrated in Fig. 3.3.

In the adiabatic regime,  $\omega \ll 1/\tau$ , both currents  $I_3^{(0)}$  and  $I_3^{(\Phi)}$  in general show a linear dependence in  $\omega$ . We however note that our choice of a spatially symmetric model potential for the QPCs leads to a flux independent part of the current proportional to  $\omega^2$ . This quadratic frequency dependence is not clearly visible in the plot in Fig. 3.3. This sensitivity of  $I_3^{(0)}$  to spatial symmetry is further discussed below.

### 3.3.1 Weak amplitude pumping

Several of the properties of the pumped current become more transparent in the limit of weak pumping, [26] where only one quantum of energy  $\hbar\omega$  can be absorbed or emitted when scattering through the MZI. This allows us to write the two current parts on the form

$$\begin{aligned}
I_3^{(0)} &= \frac{-2e\omega}{\pi} \Im \left\{ t'_B \delta t_B^{*'} (\delta t_A t_A^* + \delta r'_A r_A'^*) \right. \\
&\times \sin\left(\phi_A - \phi_B - \omega \left[ \tau + \frac{\hbar}{2E_c} \right] \right) \\
&+ r_B \delta r_B^* (\delta r_A r_A^* + \delta t'_A t_A'^*) \\
&\left. \times \sin\left(\phi_A - \phi_B - \omega \left[ \tau - \frac{\hbar}{2E_c} \right] \right) \right\} \quad (3.19)
\end{aligned}$$

with  $\Im$  the imaginary part and

$$\begin{aligned}
I_3^{(\Phi)} &= \frac{8eE_c}{h} g(T) \sin\left(\frac{\hbar\omega}{2E_c}\right) \Im \left\{ e^{i\psi_{LR}} \right. \\
&\times [(\delta r_B t_B'^* + r_B \delta t_B'^*) (r_A \delta t_A^* + \delta t'_A r_A'^*) \\
&\times \sin(\phi_A - \phi_B - \omega\tau) \\
&\left. + r_B t_B'^* [\delta r_A \delta t_A^* + \delta t'_A \delta r_A'^*] \sin\left(\frac{\hbar\omega}{2E_c}\right) \right\}. \quad (3.20)
\end{aligned}$$

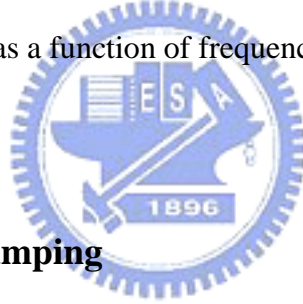
Here we introduced the notation  $r_{j,0} = r_j, r'_{j,0} = r'_j, t_{j,0} = t_j$  and  $t'_{j,0} = t'_j$  for the amplitudes to scatter elastically, without absorbing or emitting any energy quantum, and  $r_{j,\pm 1} = \delta r_j e^{\mp i\phi_j}, r'_{j,\pm 1} = \delta r_j^{*\mp i\phi_j}, t_{j,\pm 1} = \delta t_j e^{\mp i\phi_j}$  and  $t'_{j,\pm 1} = \delta t_j^{*\mp i\phi_j}$  for the amplitudes to emit (-) or absorb (+) a single energy quantum.

Importantly, the terms in the current expressions directly correspond to the first order scattering processes shown in Fig. 3.2. For  $I_3^{(0)}$ , the upper term in Eq. (3.19),  $I_{3L}^{(0)}$ , arises due to interference between electrons that propagate along the left arm and pick up or lose a quantum  $\hbar\omega$  at either  $A$  or  $B$ . These processes are shown at the top of panel (a) in Fig. 3.2. The lower term in Eq. (3.19),  $I_{3R}^{(0)}$ , arises from the corresponding processes for electrons propagating in the right interferometer arm.

For the flux dependent current  $I_3^{(\Phi)}$ , the interfering paths go along different interferometer arms  $L$  and  $R$ . The upper term in Eq. (3.20) arises from processes where electrons pick up or lose one quantum  $\hbar\omega$  at different QPCs  $A$  and  $B$ . These processes are depicted to the right in panel (b). The lower term in Eq.

(3.20) arises from processes where both electrons pick up or lose one quantum  $\hbar\omega$  at the same QPC,  $A$  or  $B$ , depicted to the left in panel (b). Importantly, electrons which scatter inelastically at the same QPC pick up the same information on the pumping phase. Consequently, the corresponding interference term is independent on the pumping phase, as seen in the lower term in Eq. (3.20).

The weak amplitude expressions for the current also clearly demonstrate the origin of the sign change of the current as a function of frequency, as shown in Fig. 3.3. In the low frequency, adiabatic limit the weak amplitude pumped current is always [2] proportional to  $\sin(\phi_A - \phi_B)$ , i.e. the sign of the current is determined by the pumping phase difference. In Eqs. (3.19) and (3.20) the frequency formally enters the current expressions as an additional pumping phase, thus leading to an oscillating sign of the current as a function of frequency.



### 3.3.2 Adiabatic, weak pumping

It is of particular importance to consider the weakly pumped currents in the adiabatic limit, where the effects of inelastic dephasing are minimized. In the adiabatic limit the current reduces to, using the unitarity relations in Eq. (3.5)

$$I_{3,ad}^{(0)} = \frac{ie\omega}{\pi} \sin(\phi_A - \phi_B) (r_B \delta r_B^* + r_B^* \delta r_B) \times (\delta t_A t_A^* - \delta t_A' t_A'^* - \delta r_A r_A^* + \delta r_A' r_A'^*) \quad (3.21)$$

and

$$I_{3,ad}^{(\Phi)} = \frac{2e\omega}{\pi} \sin(\phi_A - \phi_B) g(T) \Im \{ e^{i\psi_{LR}} \times (\delta r_B t_B^* + r_B \delta t_B^*) (r_A \delta t_A^* + \delta t_A' r_A'^*) \}. \quad (3.22)$$

Note that the second line in Eq. (3.21) is purely imaginary. From the expression of the

flux independent current  $I_{3,ad}^{(0)}$  we see explicitly the dependence on spatial

symmetry of QPC  $A$ . For a completely symmetric scattering potential, i.e. primed scattering amplitudes equal to unprimed, the adiabatic phase independent current is zero and the low frequency current is  $\propto \omega^2$ . We point out that the absence of a noticeable magnetic flux through the point contact area, i.e.  $t_A = t'_A$ , is not enough to suppress the adiabatic current. We also note that only the spatial symmetry of QPC  $A$  is relevant, a consequence of the chiral transport. That is, reversing the sign of the quantum Hall magnetic field, the pumped currents, now at reservoirs 1 and 2, would be sensitive to the symmetry of QPC  $B$  only.

From the dependence of  $I_{3,ad}^{(\Phi)}$  on  $\psi_{LR}$ , as well as the fact that  $\psi_{LR}$  depends both on the Aharonov-Bohm flux as well as phases picked up propagating along the edges [see definition below Eq. (3.18)], we can conclude that the flux dependent part has no definite magnetic field symmetry. We also note that in the adiabatic expression for the flux dependent current, the lower term in Eq. (3.20), independent on the pumping phases, does not contribute.

### 3.3.3 Rectification effects

For mesoscopic conductors, an unavoidable feature is stray capacitances between the various circuit elements, i.e. the electronic reservoirs, the electrostatic gates and the mesoscopic sample itself. A capacitive coupling between the pumped QPC gates and the electronic reservoirs induces an ac potential at the reservoirs (for nonzero impedance of the current measurement circuit). This gives rise to a rectification current which can obscure the pumped current. [1, 14, 21, 22, 27] In the MZI, for weak, adiabatic pumping, the rectified dc-current is in the most general situation given by [21]

$$\begin{aligned}
I_{3,rect} = & c_{A1} \frac{\partial G_{31}}{\partial V_A} + c_{B1} \frac{\partial G_{31}}{\partial V_B} \\
& + c_{A2} \frac{\partial G_{32}}{\partial V_A} + c_{B2} \frac{\partial G_{32}}{\partial V_B},
\end{aligned} \tag{3.23}$$

where the constants  $c_{ja}$  depend on the capacitive couplings, the impedance of the measurement circuit, the pumping phases and the pumping amplitudes and  $G_{\alpha\beta} = dI_{\alpha}/dV_{\beta}$  is the conductance. From the theory for the conductance of the MZI in Ref. [31] we have

$$\begin{aligned}
\frac{\partial G_{31}}{\partial V_A} = & \frac{\partial T_A}{\partial V_A} \frac{\partial G_{31}}{\partial T_A} = \frac{\partial T_A}{\partial V_A} \frac{2e^2}{h} \\
& \times \left( T_B - R_B + H \frac{R_B T_B (R_A - T_A)}{2\sqrt{R_A T_A R_B T_B}} \right)
\end{aligned} \tag{3.24}$$

and similarly for the other conductance derivatives. Here  $T_A = 1 - R_A = |t_A|^2 = |t'_A|^2$  is the transmission probability of the static QPC  $A$  and similarly for QPC  $B$  and  $H = H(k_B T, E_c, \Phi)$  a function dependent on the different energy scales  $k_B T$  and  $E_c$  and the enclosed flux  $\Phi$ . The rectification current and the pumped current thus depend differently on the scattering parameters, the magnetic flux and the energy scales, allowing one to distinguish experimentally between the two currents. In particular, from Eq. (3.24) it is clear that working with semitransparent beam splitters  $T_A = R_A = 1/2$  and  $T_B = R_B = 1/2$  the rectification currents are zero. This holds independently on the values of the individual couplings  $c_{ja}$ .

We also emphasize that induced ac-potentials at the reservoirs do not simply lead to a rectification current which is incoherently added to the pumped current; there is in general also a current due to interference between processes responsible for the pumped current and the rectification current. [27] However, the induced ac-potential is proportional to [21]  $dV_A/dt, dV_B/dt \sim \omega$  and in the weak amplitude, adiabatic limit the interference current is consequently  $\propto \omega^2$ .

A related issue is the effect of the temporary charging of the MZI itself due to the pumping. In the calculations and discussions of the pumped current above we have neglected this effect, i.e we have considered noninteracting electrons. An interacting theory should also take into account screening at the edges and the effect of capacitive couplings of the edges to e.g. each other and to the electrostatic gates. This would require a self-consistent determination of the time dependent edge state potentials. [34, 35] Such an interacting theory however goes beyond the scope of this work.

### 3.4 Dephasing

An important problem in the study of interference phenomena in mesoscopic conductors is decoherence. Phase information of the electrons propagating in the MZI is lost. Various approaches to dephasing in the voltage biased MZI were discussed in last chapter. Here we introduce dephasing in the MZI by coupling one of the arms of the interferometer to a voltage probe as shown in Fig. 3.4. A voltage probe is an additional electronic reservoir with the potential left floating. Electrons entering the voltage probe are incoherently fed back into the interferometer arm, thereby suppressing phase coherence. Voltage probes as means to introduce incoherent, inelastic scattering was proposed by Büttiker. [36, 37] The concept has thereafter been extended and applied to a large number of mesoscopic conductors, both theoretically and experimentally. A recent account of this development was given in Ref. [38].

For our purposes, in quantum Hall systems the theory of current and noise in the presence of voltage probes was developed in Ref. [39] and applied to a voltage biased MZI in Refs. [31, 40, 41]. We point out that the very recent experiments by Oberholzer *et al.*, [42] investigating the current cross correlations in a quantum Hall

geometry coupled to a voltage probe, were in excellent agreement with the theory of Ref. [39]. Moreover, dephasing of the pumped current via voltage probes was considered in Refs. [43-45].

The elastic scattering matrix of the contact to the probe is given by

$$\begin{pmatrix} \sqrt{1-\epsilon} & i\sqrt{\epsilon} \\ i\sqrt{\epsilon} & \sqrt{1-\epsilon} \end{pmatrix}. \quad (3.25)$$

Here  $\epsilon$  governs the strength of the dephasing. For  $\epsilon = 1$  the dephasing is complete, i.e. the probe is fully coupled to the MZI and all electrons propagating along the interferometer arm enter the probe. For  $\epsilon = 0$  the transport is fully coherent, the probe is decoupled from the MZI.

An important property of the voltage probe is the charge relaxation time of the voltage probe, [46, 47] i.e. the time scale on which the probe is charged or discharged. The charge relaxation time determines the dynamics of the potential  $V_\varphi(t)$  of the probe and consequently the response to the injected, time dependent charge. The charge relaxation time is given by the RC-time  $\tau_{RC} = RC$ , with  $R$  the charge relaxation resistance and  $C$  the capacitance (see Fig. 3.4). Büttiker and one of the authors [43] considered adiabatic pumping in a conductor connected to a voltage probe, assuming instantaneous charge conservation at the probe, i.e. a relaxation time much shorter than the pump period. Cremers and Brouwer [44] investigated the pumped current in a chaotic quantum dot in the same short relaxation time limit. Considering the experimental setup of Ref. [1], Polianski and Brouwer [48] investigated the adiabatic dynamics of the floating potential of reservoirs. They considered the two limiting cases of long and short relaxation time compared to the pump period. Here we will consider the same limiting cases of short and long relaxation time for the voltage probe, without the restriction to adiabatic pumping.

### 3.4.1 Long charge relaxation time $\tau_{RC} \gg \mathcal{T}$

First, the case with long relaxation time is considered, where the potential of the probe does not react on the injected charge on the time scale of the pumping period,  $\tau_{RC} \gg \mathcal{T}$ . In this situation the potential of the probe is constant during the measurement. Since the particles entering the probe have scattered at the adiabatically pumped QPC A only, there is no dc-current flow into the probe and the potential of the probe  $V_\phi$  stays at the same potential as the four reservoirs of the MZI. We thus have an extended pumping problem with five instead of four equipotential reservoirs, which can be treated along the same lines as above.

First, the coupling of the MZI to the probe leads to a modification of the scattering amplitudes in Eq. (3.11), as  $S_{F,\alpha\beta} \rightarrow \tilde{S}_{F,\alpha\beta}$ , with e.g.

$$\tilde{S}_{F,31}(E_n, E) = \sum_{m=-\infty}^{\infty} \left[ r_{B,n-m} e^{ik_m L_R - i\psi_R} r_{A,m} + \sqrt{1-\epsilon} t'_{B,n-m} e^{ik_m L_L + i\psi_L} t_{A,m} \right] \quad (3.26)$$

and similar for the other amplitudes to scatter from reservoirs 1 and 2 to 3 and 4. Moreover, there are now the amplitudes to scatter to and from the probe, as e.g. from  $\phi$  to 3

$$\tilde{S}_{F,3\phi}(E_n, E) = i\sqrt{\epsilon} t'_{B,n} e^{ik_0 L_{L2} + i\psi_{L2}}, \quad (3.27)$$

where  $L_{L2}$  is the length along the left edge between the probe and QPC B (see Fig. 3.4). Inserting the scattering amplitudes  $\tilde{S}_{F,\alpha\beta}$  into the formula for the dc-current, Eq. (3.7), we arrive at the result that the coherent current is modified as

$$\begin{aligned} I_{3L}^{(0)} &\rightarrow (1-\epsilon)I_{3L}^{(0)}, \\ I_3^{(\Phi)} &\rightarrow \sqrt{1-\epsilon}I_3^{(\Phi)}. \end{aligned} \quad (3.28)$$

The flux independent current in the arm to which the probe is coupled,  $I_{3L}^{(0)}$ , is successively suppressed for increasing coupling  $\epsilon$  to the probe. For perfect



coupling,  $\epsilon = 1$ , the current  $I_{3L}^{(0)}$  is zero. The pumped current flowing through the arm not connected to the probe is however unaffected by the coupling to the probe. In contrast, the entire flux independent current  $I_3^{(\Phi)}$  is suppressed for increasing coupling to the probe, down to zero for perfect coupling.

### 3.4.2 Short charge relaxation time $\tau_{RC} \ll \mathcal{T}$

In the limit of a response time much shorter than the pumping period,  $\tau_{RC} \ll \mathcal{T}$ , the potential of the probe  $V_\varphi(t)$  adjusts instantaneously, in order to keep the time dependent current at the probe zero,  $I_\varphi(t) = 0$ . This corresponds to that all frequency components of the current [see Eq. (3.1)] are zero,

$$I_{\varphi,l} = 0. \quad (3.29)$$

Since the electrons entering the voltage probe are rapidly thermalized, the electrons in the probe can be considered in the same way as electrons in a reservoir with oscillating potential, i.e. in dynamical equilibrium. The oscillating potential gives rise to a nonequilibrium distribution of the electrons leaving the probe. Formally, assuming a uniform potential of the probe, we follow the scattering approach in Ref. [35] and introduce annihilation operators for the electrons emitted from the probe as

$$\hat{a}'_\varphi(E) = \sum_{n=-\infty}^{\infty} L_{-n} \hat{a}_\varphi(E_n). \quad (3.30)$$

Here the operators  $\hat{a}_\varphi(E)$  describe equilibrium electrons:  $\langle \hat{a}_\varphi^\dagger(E_n) \hat{a}_\varphi(E_m) \rangle = f_0(E_n) \delta_{n,m}$ . The amplitudes  $L_n$  are defined as

$$L_n = \int_0^{\mathcal{T}} \frac{dt}{\mathcal{T}} \exp(in\omega t) \exp\left(-i \int dt e V_\varphi(t)/\hbar\right). \quad (3.31)$$

The annihilation operators for particles injected into the probe can then be written as

$$\hat{b}_\varphi(E) = \sum_{n=-\infty}^{\infty} \left[ \bar{s}_{F,\varphi 1}(E, E_n) \hat{a}_1(E_n) + \bar{s}_{F,\varphi 2}(E, E_n) \hat{a}_2(E_n) + \sqrt{1-\varepsilon} L_{-n} \hat{a}_\varphi(E_n) \right] \quad (3.32)$$

Importantly, the amplitudes  $L_n$  in Eq. (3.30) effectively describe forward, inelastic scattering from the probe out into the MZI. We can consequently combine the amplitudes  $L_n$  for excitation of the electrons in the probe and the amplitudes  $\tilde{s}_{F,\alpha\beta}$  for scattering in the MZI with zero probe potential into a new, unitary Floquet scattering matrix  $\bar{s}_{F,\alpha\beta}$ . This gives  $\bar{s}_{F,\alpha\beta}(E, E_n) = \tilde{s}_{F,\alpha\beta}(E, E_n)$  for  $\beta \neq \varphi$  and  $\bar{s}_{F,\varphi\varphi}(E, E_n) = \sqrt{1-\varepsilon} L_{-n}$  and similarly for  $\bar{s}_{F,3\varphi}$  and  $\bar{s}_{F,4\varphi}$ . It is then possible to proceed as above and insert the scattering amplitudes  $\bar{s}_{F,\alpha\beta}$  into the formula for the Fourier components of the current, Eq. (3.1). This gives

$$I_{\varphi,l} = \frac{e}{h} \int_0^\infty dE \sum_{m=-\infty}^{\infty} [f_0(E_m) - f_0(E)] \times \sum_{\beta} \bar{s}_{F,\varphi\beta}^*(E, E_m) \bar{s}_{F,\varphi\beta}(E_l, E_m), \quad (3.33)$$

where  $\beta$  runs over 1, 2 and  $\varphi$ . The requirement of instantaneous current conservation, Eq. (3.29), then directly gives

$$\sum_{\beta} \bar{s}_{F,\varphi\beta}^*(E, E_m) \bar{s}_{F,\varphi\beta}(E_l, E_m) = 0, \quad (3.34)$$

which in terms of the amplitudes  $L_n$  can be written

$$L_m^* L_{m+l} = \frac{1}{\varepsilon} \sum_{\beta=1,2} \bar{s}_{F,\varphi\beta}^*(E, E_{-m}) \bar{s}_{F,\varphi\beta}(E_l, E_{-m}). \quad (3.35)$$

We will then use Eq. (3.35) to calculate the dc-current at reservoir 3. The dc-current is given by Eq. (3.7), now with the scattering amplitudes  $\bar{s}_{F,3\beta}$ . Via the amplitude  $\bar{s}_{F,3\varphi}$  the current depends on the product  $L_m^* L_{m+l}$ . Inserting the

expression for  $L_m^* L_{m+l}$  from Eq. (3.35) we arrive at the result for the flux dependent part of the current

$$I_3^{(\Phi)} \rightarrow \sqrt{1 - \epsilon} I_3^{(\Phi)}, \quad (3.36)$$

while in contrast to the long relaxation time result in Eq. (3.28), the current part  $I_3^{(0)}$  is unaffected by the dephasing.

Importantly, the different dephasing behaviors in the two regimes of probe relaxation time are clearly manifested in the pumped current. In the long time regime the suppression of the current in the left arm  $I_{3L}^{(0)}$  leads to that the measured current only depends on the time for ballistic propagation in the right arm, see Eq. (3.16). As a consequence, the beating pattern in the frequency dependence of the pumped current (see Fig. 3.3) is suppressed on increasing dephasing. In the short time regime there is no such suppression.



### 3.5 Summary

We have investigated the pumped currents in a MZI implemented in a conductor in the quantum Hall regime. The motivation for our investigation was twofold. First, a MZI is the most elementary interferometer, due to the absence of closed electronic orbits. In our proposal the pumped current in the MZI is moreover operated solely by modulating the potential at the two QPCs. This makes pumping in the MZI both fundamentally important and experimentally achievable. Second, recent experiments [49-51, 67] on transport in a voltage biased MZI has demonstrated the relevance of dephasing and raised a number of questions on the coherence properties of MZIs.

Working in the adiabatic pumping regime makes it possible to investigate these coherence properties close to equilibrium, keeping dephasing at a minimum.

The dependence of the current on pumping frequency, pumping strength, temperature and lengths of the arms of the MZI were investigated. The two parts of the current, the flux dependent and the flux independent ones, were demonstrated to depend in a qualitatively different way on frequency and temperature. The two current parts also showed a different sensitivity to dephasing, introduced by coupling a voltage probe to one of the interferometer arms. The flux dependent current was successively suppressed for increasing coupling, while only the part of the flux independent current flowing in the arm connected to the probe was sensitive to dephasing in the limit of long charge relaxation time of the probe. We also demonstrated that rectification effects, preventing an unambiguous demonstration of quantum pumping of current, are absent in the MZI when working with semitransparent beam splitters in the adiabatic, weak pumping regime.

In a broader perspective, a better understanding and control of coherence properties of edge state transport is important for a successful realization of two-particle Hanbury Brown Twiss interferometers,[52] entanglement production [52, 53] and quantum state transfer [54] in quantum Hall systems. In the context of entanglement, an unambiguous demonstration of quantum pumping in the MZI also opens up for schemes for entanglement generation based on quantum pump effects. [25, 55-58]

### 3.6 Appendix A: Oscillating Barriers

In this appendix, we determine the Floquet scattering matrix of a system varying periodically with time [59]. In such system, the time-dependent Schrödinger equation for an electron wave function  $\Psi(x, t)$  reads

$$i\hbar \frac{\partial \Psi(x, t)}{\partial t} = H(x, t) \Psi(x, t),$$

$$H(x, t) = -\frac{\hbar^2}{2m} \frac{\partial^2}{\partial x^2} + V(x, t). \quad (\text{A.1})$$

$V(x, t) = V(x, t + \mathcal{T})$  is the potential form with time period  $\mathcal{T}$ . Since the Hamiltonian  $H(x, t)$  depends on time, the system has no stationary eigenstates. However, the Floquet theorem tells us that because the Hamiltonian is periodic in time the eigenstates of Eq. (A.1) can be represented as a superposition of wave functions with energies shifted by  $n\hbar\omega$ :

$$\Psi_E(x, t) = e^{-iEt/\hbar} \sum_{n=-\infty}^{\infty} \psi_n(x) e^{-in\omega t}. \quad (\text{A.2})$$

As electrons propagate along an open system, the system may be constituted of several different scattering areas. Each scattering area is described by the local Schrödinger equation. Away from the oscillating potentials, the functions  $\psi_n(x)$  are a superposition of plane waves

$$\psi_n(x) = a_n e^{ik_n x} + b_n e^{-ik_n x}, \quad (\text{A.3})$$

where the electron momentum

$$k_n = \sqrt{\frac{2m}{\hbar^2} (E + n\hbar\omega)}. \quad (\text{A.4})$$

The connections between electron wave functions of different areas are required to fulfill two boundary conditions: (i) the conservation of the currents (ii) the continuity of the wave functions. For simplicity, below the delta potential forms are used for discussion.

First, we discuss the condition of the system with only one oscillating barrier

[60]:

$$V(x, t) = \delta(x) [V_s + 2V_0 \cos(\omega t + \phi)]. \quad (\text{A.5})$$

In this case, the functions  $\psi_n(x)$  are

$$\begin{aligned} \psi_n(x < 0) &= \delta_{n,0} e^{ik_n x} + r_n e^{-ik_n x}, \\ \psi_n(0 < x) &= t_n e^{ik_n x}. \end{aligned} \quad (\text{A.6})$$

Here the coefficients  $r_n$  and  $t_n$  for propagating modes (for which  $E_n > 0$ ) are the amplitudes of reflection from and the transmission through the system absorbing ( $n > 0$ ) or emitting ( $n < 0$ ) an energy  $|n|\hbar\omega$ , respectively. From the boundary conditions, we get

$$\Psi_E(x = 0^-, t) = \Psi_E(x = 0^+, t),$$

$$\left. \frac{\partial \Psi_E(x, t)}{\partial x} \right|_{x=0^-} - \left. \frac{\partial \Psi_E(x, t)}{\partial x} \right|_{x=0^+} = V(t) \Psi_E(x = 0, t), \quad (\text{A.7})$$

where  $V(t) = 2m/\hbar^2 [V_s + 2V_0 \cos(\omega t + \phi)]$ . Inserting Eqs. (A.2) and (A.6) into (A.7), we get

$$ik_n (\delta_{n0} - r_n - t_n) = \frac{2m}{\hbar^2} (V_s t_n + V_0 t_{n+1} e^{i\phi} + V_0 t_{n-1} e^{-i\phi}). \quad (\text{A.8})$$

After simple matrix manipulations for Eq. (A.8), the coefficients  $r_n$  and  $t_n$  are found.

The transmission probabilities are expressed as  $|S_{LL}(E_n, E)|^2 = (k_n/k_0) |r_n|^2$  and

$|S_{RL}(E_n, E)|^2 = (k_n/k_0) |t_n|^2$ , where the indices  $L$  and  $R$  correspond to the left and right

reservoirs, respectively. To obtain the matrix elements  $S_{RR}$  and  $S_{LR}$  we need to solve the same problem with plane wave coming from the right.

Next, we consider the system with two oscillating barriers [26]:

$$V(x, t) = \delta\left(x + \frac{L}{2}\right) V_1(t) + \delta\left(x - \frac{L}{2}\right) V_2(t), \quad (\text{A.9})$$

with  $V_j(t) = 2m/\hbar^2 [V_{s,j} + 2V_{0,j} \cos(\omega t + \phi_j)]$ ,  $j = 1, 2$ . The functions  $\psi_n(x)$  are

$$\psi_n\left(x < -\frac{L}{2}\right) = \delta_{n,0} e^{ik_n x} + r_n e^{-ik_n x},$$

$$\begin{aligned}\psi_n\left(-L/2 < x < L/2\right) &= A_n e^{ik_n x} + B_n e^{-ik_n x}, \\ \psi_n\left(L/2 < x\right) &= t_n e^{ik_n x}.\end{aligned}\tag{A.10}$$

The boundary conditions give

$$\begin{aligned}\Psi_E\left(x = -L/2 + 0^-, t\right) &= \Psi_E\left(x = -L/2 + 0^+, t\right), \\ \Psi_E\left(x = L/2 + 0^-, t\right) &= \Psi_E\left(x = L/2 + 0^+, t\right), \\ \frac{\partial\Psi_E(x, t)}{\partial x}\Big|_{x=-L/2+0^-} - \frac{\partial\Psi_E(x, t)}{\partial x}\Big|_{x=-L/2+0^+} &= V_1(t)\Psi_E\left(x = -L/2, t\right), \\ \frac{\partial\Psi_E(x, t)}{\partial x}\Big|_{x=L/2+0^-} - \frac{\partial\Psi_E(x, t)}{\partial x}\Big|_{x=L/2+0^+} &= V_2(t)\Psi_E\left(x = L/2, t\right),\end{aligned}\tag{A.11}$$

where  $V_j(t) = 2m/\hbar^2 [V_{s,j} + 2V_{0,j} \cos(\omega t + \phi_j)]$ . Inserting Eqs. (A.2) and (A.10) into (A.11), we get

$$\begin{aligned}\delta_{n0} e^{-ik_n L/2} + r_n e^{ik_n L/2} &= A_n e^{-ik_n L/2} + B_n e^{ik_n L/2}, \\ A_n e^{ik_n L/2} + B_n e^{-ik_n L/2} &= t_n e^{ik_n L/2}, \\ ik_n e^{-ik_n L/2} (\delta_{n0} - A_n) - ik_n e^{ik_n L/2} (r_n - B_n) &= \frac{2m}{\hbar^2} \left[ V_{s1} (\delta_{n0} e^{-ik_n L/2} + r_n e^{ik_n L/2}) \right. \\ &\quad \left. + V_{01} e^{i\phi_1} (\delta_{n+1,0} e^{-ik_{n+1} L/2} + r_{n+1} e^{ik_{n+1} L/2}) + V_{01} e^{-i\phi_1} (\delta_{n-1,0} e^{-ik_{n-1} L/2} + r_{n-1} e^{ik_{n-1} L/2}) \right], \\ ik_n (A_n e^{ik_n L/2} - B_n e^{-ik_n L/2} - t_n e^{ik_n L/2}) &= \frac{2m}{\hbar^2} \left[ V_{s2} t_n e^{ik_n L/2} + V_{02} e^{i\phi_2} (t_{n+1} e^{ik_{n+1} L/2} + t_{n-1} e^{ik_{n-1} L/2}) \right].\end{aligned}\tag{A.12}$$

After the a lengthy matrix manipulations, Eq. (A.12) gives the coefficients  $t_n$ ,  $r_n$ ,  $A_n$  and  $B_n$ . The transmission probabilities are given by following the similar way as one barrier problem. For the systems with more barriers than two, the transmission and the reflection could be found by following the similar derivation shown above. In the next chapter, we will use this Floquet matrix method for a gate array system, where multiple time-dependent potentials are considered to pump currents and the instantaneous Bragg reflection are found to be the mechanism of transport.

### 3.7 Appendix B: Time Representation of Pumped Currents

Here we will show the equivalent expression of the pumped currents within the time representation. For specificity, the potentials of two beam splitters are assumed with spatial symmetry.

Following the similar line in the main body of chapter 3, the scattering amplitudes from lead 1 to lead 3 by substituting Eqs. (3.9) and Eq. (3.10) into Eq. (3.11) are given

$$s_{F,31}(E_n, E) = s_{31,n}(E) = \int_0^T \frac{dt}{T} e^{in\omega t} s_{31}(E, t) \quad (\text{B.1})$$

with

$$s_{31,n}(E) = \iint_0^T \frac{dt}{T} \frac{dt'}{T} e^{in\omega t} \sum_{m=-\infty}^{\infty} e^{-im\omega(t-t'-\tau_j)} \times \sum_{j=L,R} R_{31,j}(E, t, t') e^{i\theta_{31,j}(E, t, t') + iP_j(E)} \quad (\text{B.2})$$

and

$$s_{31}(E, t) = \sum_{j=L,R} R_{31,j}(E, t, t - \tau_j) e^{i\theta_{31,j}(E, t, t - \tau_j) + iP_j(E)}, \quad (\text{B.3})$$

where

$$R_{31,L}(E, t, t') e^{i\theta_{31,L}(E, t, t')} = t_2(E, t) t_1(E, t'),$$

$$R_{31,R}(E, t, t') e^{i\theta_{31,R}(E, t, t')} = r_2(E, t) r_1(E, t'),$$

$$P_L(E) = \zeta_L(\mu) + EL_L/\hbar v_D - \psi_L,$$

$$P_R(E) = \zeta_R(\mu) + EL_R/\hbar v_D + \psi_R. \quad (\text{B.4})$$



Eq. (B.3) is reduced from Eq. (B.2) by taking the summation over index  $m$ , which gives the Dirac delta-function. Therefore, the scattering matrix elements  $s_{F,\alpha\beta}$  are given

$$s_{F,\alpha\beta}(E_n, E) = s_{\alpha\beta,n}(E) = \int_0^T \frac{dt}{T} e^{in\omega t} s_{\alpha\beta}(E, t) \quad (\text{B.5})$$

with

$$s_{\alpha\beta}(E, t) = \sum_{j=L,R} R_{\alpha\beta,j}(E, t, t - \tau_j) e^{i\theta_{\alpha\beta,j}(E, t, t - \tau_j) + iP_j(E)}, \quad (\text{B.6})$$

where  $R_{\alpha\beta,j}$  and  $\theta_{\alpha\beta,j}$  are the norm and the phase of an amplitude corresponding to scattering from lead  $\beta$  to lead  $\alpha$  through the arm  $j$ , respectively. The presence of a delay time  $\tau_j$  in Eq. (B.6) defines the different regimes of pumping, adiabatic at  $\tau_L, \tau_R \ll T$  and non-adiabatic at  $\tau_L$  or  $\tau_R \gtrsim T$ .

The Fourier coefficients  $I_{\alpha,l}$  of the time-dependent current are calculated for the availability of the time-dependent currents. Using Eqs. (3.6), (B.5) and (B.6), we get

$$I_{\alpha,l} = \frac{e}{h} \iint_0^T \frac{dt}{T} \frac{dt'}{T} \int_{-\infty}^{\infty} dE \sum_{\beta=1,2} \sum_{n=-\infty}^{\infty} e^{il\omega t} e^{-in\omega(t'-t)} \times s_{\text{in},\alpha\beta}^*(E, t') s_{\text{in},\alpha\beta}(E, t) [f_0(E) - f_0(E_n)]. \quad (\text{B.7})$$

We split the current into two parts as

$$I_{\alpha,l} = \frac{e}{h} \iint_0^T \frac{dt}{T} \frac{dt'}{T} \int_{-\infty}^{\infty} dE \sum_{\beta=1,2} \sum_{n=-\infty}^{\infty} e^{il\omega t} e^{-in\omega(t'-t)} \times [F_{\alpha}^{(0)}(E, t, t') + F_{\alpha}^{(\Phi)}(E, t, t')] [f_0(E) - f_0(E_n)] \quad (\text{B.8})$$

with the flux-independent part

$$\begin{aligned}
F_{\alpha}^{(0)}(E, t, t') &= \sum_{\beta=1,2} \sum_{j=L,R} \\
&\times R_{\alpha\beta,j}(E, t, t - \tau_j) R_{\alpha\beta,j}(E, t', t' - \tau_j) \\
&\times e^{i\theta_{\alpha\beta,j}(E, t, t - \tau_j) - i\theta_{\alpha\beta,j}(E, t', t' - \tau_j)}
\end{aligned} \tag{B.9}$$

and the flux-dependent part

$$\begin{aligned}
F_{\alpha}^{(\Phi)}(E, t, t') &= \sum_{\beta=1,2} \left\{ R_{\alpha\beta,L}(E, t, t - \tau_L) R_{\alpha\beta,R}(E, t', t' - \tau_R) \right. \\
&\times e^{i(E/E_c) + i[\Theta_{\alpha\beta}(t, t') - 2\pi\Phi/\Phi_0]} \\
&+ R_{\alpha\beta,L}(E, t', t' - \tau_L) R_{\alpha\beta,R}(E, t, t - \tau_R) \\
&\left. \times e^{-i(E/E_c) - i[\Theta_{\alpha\beta}(t', t) - 2\pi\Phi/\Phi_0]} \right\}.
\end{aligned} \tag{B.10}$$

Here the phase  $\Theta_{\alpha\beta}$  reads as follows

$$\begin{aligned}
\Theta_{\alpha\beta}(E, t, t') &= \delta\zeta(\mu) + \theta_{\alpha\beta,L}(E, t, t - \tau_L) \\
&\quad - \theta_{\alpha\beta,R}(E, t', t' - \tau_R),
\end{aligned}$$

with  $\delta\zeta(\mu) = \zeta_L(\mu) - \zeta_R(\mu)$ .

In the energy integral, only energies of order  $\max(\hbar\omega, k_B T)$  away from  $\mu$  contribute, i.e.  $\hbar\omega, k_B T \ll \mu$ . Then the energy dependence of the scattering matrices of the point-like splitters could be neglected and take them at  $E = \mu$ .

Using the notations:  $R_{\alpha\beta,j}(\mu, t, t - \tau_j) = R_{\alpha\beta,j}(t, t - \tau_j)$  and

$\theta_{\alpha\beta,j}(\mu, t, t - \tau_j) = \theta_{\alpha\beta,j}(t, t - \tau_j)$ , and integrating over energy in Eq. (3.6), we get

$$\begin{aligned}
I_{\alpha,l} &= \frac{e}{2\pi} \sum_{n=-\infty}^{\infty} \iint_0^T \frac{dt}{T} \frac{dt'}{T} e^{i\ell\omega t} e^{-in\omega(t'-t)} \left[ n\omega F_{\alpha}^{(0)}(t; t') \right. \\
&\quad \left. + \frac{\pi k_B T}{E_c} \operatorname{csch}\left(\frac{\pi k_B T}{E_c}\right) F_{\alpha,n}^{(\Phi)}(t; t') \right]
\end{aligned} \tag{B.11}$$

with

$$\begin{aligned}
F_{\alpha,n}^{(\Phi)}(t;t') &= i \frac{E_c}{\hbar} \sum_{\beta=1,2} \left\{ R_{\alpha\beta,L}(t,t-\tau_L) R_{\alpha\beta,R}(t',t'-\tau_R) \right. \\
&\quad \times e^{i[\Theta_{\alpha\beta}(t,t')-2\pi\Phi/\Phi_0]} \left[ e^{-i\hbar\omega/E_c} - 1 \right] \\
&\quad + R_{\alpha\beta,L}(t',t'-\tau_L) R_{\alpha\beta,R}(t,t-\tau_R) \\
&\quad \left. \times e^{-i[\Theta_{\alpha\beta}(t',t)-2\pi\Phi/\Phi_0]} \left[ 1 - e^{i\hbar\omega/E_c} \right] \right\}
\end{aligned} \tag{B.12}$$

To find the time-dependent current  $I_\alpha(t)$ , we perform the inverse Fourier transformation of Eq. (3.6) and get:

$$I_\alpha(t) = -\frac{e}{2\pi} \left[ G_\alpha^{(0)}(t) + \frac{\pi k_B T}{E_c} \operatorname{csch}\left(\frac{\pi k_B T}{E_c}\right) G_\alpha^{(\Phi)}(t) \right] \tag{B.13}$$

with

$$G_\alpha^{(0)}(t) = \sum_{\beta=1,2} \sum_{j=L,R} R_{\alpha\beta,j}^2(t,t-\tau_j) \partial_t \theta_{\alpha\beta,j}(t,t-\tau_j) \tag{B.14}$$

and

$$\begin{aligned}
G_\alpha^{(\Phi)}(t) &= 2 \frac{E_c}{\hbar} \sum_{\beta=1,2} R_{\alpha\beta,L}(t,t-\tau_L) R_{\alpha\beta,R}(t,t-\tau_R) \\
&\quad \times \sin \left[ \frac{2\pi\Phi}{\Phi_0} - \Theta_{\alpha\beta}(t,t) \right].
\end{aligned} \tag{B.15}$$

Averaging Eqs. (B.13)-(B.15) over the pumping period  $\mathcal{T}$  gives a direct current. The effects of dephasing on the instantaneous currents under the long or the short relaxation time conditions are found the same as the discussions in the main text.

### 3.8 Appendix C: Shot Noise

Subjective to the analysis of shot noise, the cross correlation between leads 3 and 4 is observed due to the vanishment of the contribution of the thermal noise. The characteristics of the zero frequency shot noise in a pump driven MZI are shown here. The used method follows the same as Ref. [61]. Two beam splitters are modeled by

the form of the delta potentials, i.e. Eq. (3.12). Then, the shot noise (cross correlation) between leads 3 and 4 are given by

$$P_{34}^{(sh)} = P_{34}^{(0)} + P_{34}^{(\Phi)} + P_{34}^{(2\Phi)}. \quad (\text{C.1})$$

The flux-independent part is

$$P_{34}^{(0)} = \frac{e^2}{h} \sum_{n,m,p,m_1 \cdots m_4} T_{34;n,m,p,m_1 \cdots m_4}^{(0)} \times \left[ -2k_B T + (m-n)\hbar\omega \coth\left(\frac{(m-n)\hbar\omega}{2k_B T}\right) \right], \quad (\text{C.2})$$

with the scattering probability dependent function

$$T_{34;n,m,p,m_1 \cdots m_4}^{(0)} = \eta_{\tau_L; \tau_R}^{(1)} \lambda^{(1)} r_{B,-m_2} r_{B,p-m_4} r_{B,p-m_3}^* r_{B,-m_1}^* + \eta_{\tau_R; \tau_L}^{(1)} \lambda^{(1)} t_{B,-m_2} t_{B,p-m_4} t_{B,p-m_3}^* t_{B,-m_1}^* \quad (\text{C.3})$$

$$+ \eta_{\tau_L; \tau_R}^{(2)} \lambda^{(2)} r_{B,-m_2} r_{B,p-m_4} t_{B,p-m_3}^* t_{B,-m_1}^* + \eta_{\tau_R; \tau_L}^{(2)} \lambda^{(2)} t_{B,-m_2} t_{B,p-m_4} r_{B,p-m_3}^* r_{B,-m_1}^*$$

$$+ \eta_{\tau_L}^{(3)} \lambda^{(2)} t_{B,-m_2} r_{B,p-m_4} r_{B,p-m_3}^* t_{B,-m_1}^* + \eta_{\tau_R}^{(3)} \lambda^{(2)} r_{B,-m_2} t_{B,p-m_4} t_{B,p-m_3}^* r_{B,-m_1}^*,$$

$$\eta_{\tau_L; \tau_R}^{(1)} = e^{i\omega[(m_4-m_3)\tau_L + (m_2-m_1)\tau_R]}, \quad (\text{C.4})$$

$$\eta_{\tau_L; \tau_R}^{(2)} = e^{i\omega[(m_4-m_1)\tau_L + (m_2-m_3)\tau_R]}, \quad (\text{C.5})$$

$$\eta_{\tau_L}^{(3)} = e^{i\omega(-m_1 + m_2 - m_3 + m_4)\tau_L}. \quad (\text{C.6})$$

The flux-dependent parts corresponding to the contributions of  $\hbar/j e$  ( $j = 1, 2$ ) oscillations are

$$P_{34}^{(j\Phi)} = \frac{4e^2}{h} \sum_{n,m,p,m_1 \cdots m_4} T_{34;n,m,p,m_1 \cdots m_4}^{(j\Phi)} \times g_{n,m}(k_B T, \hbar\omega, E_c/j) \quad (\text{C.7})$$

with the energy dependent function

$$g_{n,m}(k_B T, \hbar\omega, E_c/j) = \pi k_B T \operatorname{csch}\left(\frac{\pi k_B T}{E_c}\right) \times \left[ -\frac{k_B T}{E_c} \cos\left(\frac{(m-n)\hbar\omega}{2E_c}\right) + \coth\left(\frac{(m-n)\hbar\omega}{2k_B T}\right) \sin\left(\frac{(m-n)\hbar\omega}{2E_c}\right) \right] \quad (\text{C.8})$$

and the  $\Phi$  dependent functions

$$\begin{aligned}
T_{34;n,m,p,m_1 \dots m_4}^{(\Phi)} = & \\
& \Re \left[ \chi^{(1)} \lambda^{(3)} r_{B,-m_2} r_{B,p-m_4} t_{B,p-m_3}^* r_{B,-m_1}^* \right] \\
& + \Re \left[ \chi^{(1)} \lambda^{(3)} t_{B,-m_4} t_{B,p-m_2} t_{B,p-m_1}^* r_{B,-m_3}^* \right] \\
& + \Re \left[ \chi^{(2)} \lambda^{(3)} t_{B,-m_2} r_{B,p-m_4} r_{B,p-m_3}^* r_{B,-m_1}^* \right] \\
& + \Re \left[ \chi^{(2)} \lambda^{(3)} t_{B,-m_4} r_{B,p-m_2} t_{B,p-m_1}^* t_{B,-m_3}^* \right], \tag{C.9}
\end{aligned}$$

$$\chi^{(1)} = e^{i\omega[m_4\tau_L + (-m_1+m_2-m_3)\tau_R]} e^{i\psi_{LR} - i(m+n)\hbar\omega/2E_c}, \tag{C.10}$$

$$\chi^{(2)} = e^{i\omega[(m_2-m_3+m_4)\tau_L - m_1\tau_R]} e^{i\psi_{LR} - i(m+n)\hbar\omega/2E_c}; \tag{C.11}$$

$$\begin{aligned}
T_{34;n,m,p,m_1 \dots m_4}^{(2\Phi)} = & \\
= & \Re \left[ e^{i\omega[(m_2+m_4)\tau_L - (m_1+m_3)\tau_R]} e^{i2\psi_{LR} - i(m+n)\hbar\omega/E_c} \right. \\
& \left. \times \lambda^{(1)} t_{B,-m_2} r_{B,p-m_4} t_{B,p-m_3}^* r_{B,-m_1}^* \right]. \tag{C.12}
\end{aligned}$$

Here we use

$$\begin{aligned}
\lambda^{(1)} = & \left( t_{A,m_3-m}^* r_{A,m_2-m} + r_{A,m_3-m}^* t_{A,m_2-m} \right) \\
& \times \left( t_{A,m_1-n}^* r_{A,m_4-n} + r_{A,m_1-n}^* t_{A,m_4-n} \right), \tag{C.13}
\end{aligned}$$

$$\begin{aligned}
\lambda^{(2)} = & \left( t_{A,m_3-m}^* t_{A,m_2-m} + r_{A,m_3-m}^* r_{A,m_2-m} \right) \\
& \times \left( t_{A,m_1-n}^* t_{A,m_4-n} + r_{A,m_1-n}^* r_{A,m_4-n} \right), \tag{C.14}
\end{aligned}$$

$$\begin{aligned}
\lambda^{(3)} = & \left( t_{A,m_3-m}^* t_{A,m_2-m} + r_{A,m_3-m}^* r_{A,m_2-m} \right) \\
& \times \left( t_{A,m_1-n}^* r_{A,m_4-n} + r_{A,m_1-n}^* t_{A,m_4-n} \right). \tag{C.15}
\end{aligned}$$

Notice that, each sideband contribution of the flux-independent and the flux-dependent parts of the current correlations is given by the product of the transmission probability and the energy dependent parts. Due to the conservation law

of the shot noise [61], the auto-correlations in lead 3 are found as  $P_{33}^{(0)} = -P_{34}^{(0)}$ ,

$$P_{33}^{(\Phi)} = -P_{34}^{(\Phi)} \quad \text{and} \quad P_{33}^{(2\Phi)} = -P_{34}^{(2\Phi)}, \text{ i.e. } P_{33} = -P_{34}.$$

*The low temperature condition*— Turning to the low temperature condition  $k_B T \ll \hbar\omega$ , Eqs. (C.2) and (C.7) are respectively simplified as

$$P_{34}^{(0)} = \frac{e^2 \omega}{2\pi} \sum_{n,m,p,m_1 \dots m_4} |m-n| T_{34;n,m,p,m_1 \dots m_4}^{(0)}, \quad (\text{C.16})$$

and

$$P_{34}^{(j\Phi)} = \frac{4e^2 E_c}{j\hbar} \sum_{n,m,p,m_1 \dots m_4} T_{34;n,m,p,m_1 \dots m_4}^{(j\Phi)} \times \left| \sin\left(\frac{j(m-n)\hbar\omega}{2E_c}\right) \right|, \quad (\text{C.17})$$

with  $j=1, 2$ . The variations of the flux-independent part  $P_{34}^{(0)}$  and the flux-dependent parts  $P_{34}^{(\Phi)}$  and  $P_{34}^{(2\Phi)}$  of the current correlation are plotted as a function of the frequency in the up panel of Fig. 3.5. The parameters are chosen as  $L_L = 10\mu\text{m}$ ,  $L_R = 5\mu\text{m}$ ,  $v_D = 10^5 \text{ s/m}$ ,  $k_\mu = 10^8/\text{m}$ ,  $V_s = 2k_\mu$ ,  $V_A = V_B = 0.01k_\mu$  and  $\phi_B - \phi_A \equiv \phi = 3.2$ . The weak pump condition  $V_A, V_B \ll V_s$  is considered for simplicity. As the frequency increasing, the flux-independent part  $P_{34}^{(0)}$  shows a proportion to the frequency with the small oscillations. The variations follow  $-\omega[xf(\omega) + y]$  with the coefficients  $y > x$  and a harmonic function  $f(\omega)$  formed by  $\sin(\omega\tau_j)$  and  $\cos(\omega\tau_j)$ ,  $j = L, R$ . In the other hand, the flux-dependent parts  $P_{34}^{(\Phi)}$  and  $P_{34}^{(2\Phi)}$  just show the oscillations with the invariant amplitudes. The sum of those parts is a negative value revealing the nature of fermions [38]. In high frequency regime  $\hbar\omega \gg E_c$ , the flux-independent part of shot noise becomes the dominative contributions. The period of the oscillations is found as the common multiple of two frequency scales  $[2\pi/\tau_L, 2\pi/\tau_R](\hbar/E_c) \simeq 6.28$  resulted from the existence of the phases  $\omega\tau_L$  and  $\omega\tau_R$ . The down panel of Fig. 3.5 shows the variations of the currents  $I_3$  in lead 3 with respective to the frequency. Contrast to the current correlation, as increasing the frequency the currents  $I_3$  fluctuate up and down

around zero with the amplitude proportional to the frequency and vary approximately with the form  $\omega f'(\omega)$ . As the discussion above, the frequency comes into play as an additional pumping phase which alters the sign of the currents.  $I_4 = -I_3$  is given from the current conservation. The different behaviors of the current correlations and the currents with respect to the frequency give rise to the regimes in which although the pumped currents become zero the shot noise still exists. Similar results were found in one parameter pump [11], where the created noise is due to the time-dependent excitation while the electron currents and the hole currents are canceled to each other.

The cross correlations  $P_{34}$  varying with two tunable phases  $\phi$  and  $\Phi/\Phi_0$  are shown in Fig. 3.6(a) and Fig. 3.6(b), which are respectively taken into account under the non-adiabatic ( $\omega = 15\text{GHz}$ ) and the adiabatic ( $\omega = 1.43\text{GHz}$ ) situations. Other parameters are the same as Fig. 3.5. In both situations, the cross correlations show some valley structures with the negative values. However, contrary to the non-adiabatic situation, the noiseless regimes are found in the maximum of the red areas of the adiabatic situation, indicated by the symbols of the triangles at parameters  $\phi = 0$ ,  $\Phi/\Phi_0 = 0.075$  and  $\phi = 0.99\pi$ ,  $\Phi/\Phi_0 = 0.58$ . We note that here the currents do not vanish.

Taking the analytical expressions as  $\omega \rightarrow 0$ , we get

$$P_{34}^{(0)} = -\frac{e^2\omega(1+a^2+a^4)b^2}{\pi(1+a^2)^4} + O(\omega^3), \quad (\text{C.18})$$

$$P_{34}^{(\Phi)} = -\frac{e^2\omega \cos\phi \cos(\psi_{LR})b^2}{\pi(1+a^2)^2} + O(\omega^2) \quad (\text{C.19})$$

and

$$P_{34}^{(2\Phi)} = -\frac{e^2\omega a^2 \cos(2\psi_{LR})b^2}{\pi(1+a^2)^4} + O(\omega^3), \quad (\text{C.20})$$

where  $a = V_{s,A}/k_\mu = V_{s,B}/k_\mu$ ,  $b = 2V_A/k_\mu = 2V_B/k_\mu$ . As the condition  $\phi=0$  and  $\Phi/\Phi_0 = 0.075$  of Fig. 3.6(b), the phases show  $\cos(\psi_{LR} = \pi) = -1$  and  $\cos(2\psi_{LR} = 2\pi) = 1$  in our choosing parameters. Thus, from Eqs. (C.18)-(C.20) we get  $P_{34} = P_{34}^{(0)} + P_{34}^{(\Phi)} + P_{34}^{(2\Phi)} = 0$ . Similar results are found for the condition  $\phi = 0.99\pi$ ,  $\Phi/\Phi_0 = 0.58$  of Fig. 3.6(b). The higher orders of  $P_{34}^{(0)}$  and  $P_{34}^{(2\Phi)}$  are in order  $\omega^3$ , while that of  $P_{34}^{(\Phi)}$  is in order  $\omega^2$ . Therefore, for the non-adiabatic regime the cancellation between the flux-independent and the flux-dependent parts would not occur. The noiseless regime is only given in the adiabatic regime.

In the other hand, along the transverse transections in Fig. 3.6(a) [Fig. 3.6(b)], the cross correlations vary with the phase  $\phi$ . The cross correlations in the adiabatic condition vary approximately with a simple form  $\cos\phi$ , while the cross correlations in the non-adiabatic condition vary without a simple relation with the phases  $\phi$ . From Eqs. (C.18)-(C.20), in the adiabatic limit the flux-independent part  $P_{34}^{(0)}$  and the  $h/2e$  contribution  $P_{34}^{(2\Phi)}$  are reduced as phase  $\phi$  independent functions, while the  $h/e$  contribution shows the dependence of the  $\cos\phi$  variation. Thus, the current correlations  $P_{34}$  vary as a function of  $\cos\phi$ . However, in the non-adiabatic regime, the more complicate phase  $\phi$  dependence is involved and has no such simple form.

Furthermore, in the adiabatic limit the current correlations vary linearly with the frequency at the low temperature condition, shown in the solid line of Fig. 3.7(a). However, the current correlations at the low frequency condition, i.e.  $\hbar\omega \ll k_B T \ll E_c$  (the second inequality gives no thermal effects), behavior quadratically as increasing frequency, shown in the solid line of Fig. 3.7(a). Notice



that, the dash line is fifty times the original value. Other parameters are the same as Fig. 3.5. In the following the analysis is performed in the low frequency condition.

*The low frequency condition*— At the condition:  $\hbar\omega \ll k_B T$ , Eqs. (C.2) and (C.7) are respectively simplified as

$$P_{34}^{(0)} = \frac{e^2}{h} \frac{(\hbar\omega)^2}{6k_B T} \sum_{n,m,p,m_1 \cdots m_4} (m-n)^2 \times T_{34}^{(0)}(n,m,p,m_1 \cdots m_4) \quad (\text{C.21})$$

and

$$P_{34}^{(j\Phi)} = \frac{e^2}{h} (\hbar\omega)^2 \tilde{g}(k_B T, E_c/j) \sum_{n,m,p,m_1 \cdots m_4} (m-n)^2 \times T_{34}^{(j\Phi)}(n,m,p,m_1 \cdots m_4) \quad (\text{C.22})$$

with

$$\tilde{g}(k_B T, E_c/j) = \frac{\pi}{3E_c/j} \operatorname{csc} h\left(\frac{\pi k_B T}{E_c/j}\right) \left[ 1 + \left(\frac{k_B T}{E_c/j}\right)^2 \right], \quad (\text{C.23})$$

$j = 1, 2$ .

Using Eqs. (C.21)-(C.23), the variations of the flux-independent and the flux-dependent parts of the current correlations are shown as a function of the temperature in Fig. 3.7(b). Choose  $\phi = 0.5$  and other parameters the same as those for Fig. 3.5. As increasing the temperature, the  $h/2e$  contributions show the most rapid decrease than other contributions and approach zero around  $k_B T/E_c \sim 1$ . From Eq. (C.23), the decay rate follows  $\exp(-2\pi k_B T/E_c) [1 + (2k_B T/E_c)^2]$ . The  $h/e$  contributions vanish around  $k_B T/E_c \sim 2$  and follow the decay rate  $\exp(-\pi k_B T/E_c) [1 + (k_B T/E_c)^2]$ . However, the flux-independent part of the current correlation shows the very slowly suppression by the temperature effects. Up to the scales  $k_B T/E_c \sim 4$ , the flux-independent part still survives. From Eq. (C.21), the

suppression rate is inversely proportional to the temperature. Contrary to the current correlations, the pump currents would not be totally suppressed by the temperature.

Similar to the low temperature condition, the noiseless regime is found here. As the condition without thermal effects  $k_B T \ll E_c$ , the similar variations of the current correlations subject to the phases  $\phi$  and  $\Phi/\Phi_0$  could be found, however, with a smaller order. The conditions for the noiseless regimes are also found at the same parameters. At  $\phi = 0$ , the current correlations varying with the magnetic phases  $\Phi/\Phi_0$  are shown in Fig. 3.7(c) subject to different temperatures. As  $k_B T = 0.1 E_c$  the solid line approaches to zero around  $\Phi/\Phi_0 = 0.075$ . As temperature increases, the noiseless regime found is removed. The inset of Fig. 3.7(c) enlarges the transition between the noiseless regime and the noisy regime. Otherwise, the amplitudes of the current correlations are suppressed as the temperature increases.

Performing the limit  $\omega \rightarrow 0$  on Eqs. (C.21)-(C.23), we get

$$P_{34}^{(0)} = -\frac{e^2(\hbar\omega)^2 b^2(1+a^2+a^4)}{3\hbar k_B T(1+a^2)^4} + O(\omega^3), \quad (C.24)$$

$$P_{34}^{(\Phi)} = -\frac{e^2(\hbar\omega)^2 b^2 \cos\phi \cos\psi_{LR}}{h(1+a^2)^2} \tilde{g}(k_B T, E_c) + O(\omega^3) \quad (C.25)$$

and

$$P_{34}^{(2\Phi)} = -\frac{e^2(\hbar\omega)^2 a^2 b^2 \cos(2\psi_{LR})}{h(1+a^2)^4} \tilde{g}(k_B T, E_c/2) + O(\omega^3). \quad (C.26)$$

As  $k_B T \ll E_c$ , the energy dependent function is simplified as  $\tilde{g}(k_B T, E_c/2) \simeq (3k_B T)^{-1}$ . Three parts of the currents correlation have the same trend with the temperature. At  $\Phi/\Phi_0 = 0.075$  the magnetic phases are  $\cos(\psi_{LR} = \pi) = -1$  and  $\cos(2\psi_{LR} = 2\pi) = 1$  in our choosing parameters. Thus, as  $\phi = 0$  the relation between Eqs. (C.24)-(C.26) gives

$P_{34}^{(0)} + P_{34}^{(\Phi)} + P_{34}^{(2\Phi)} = 0$  . However, as increasing the temperature, the  $h/e$  and  $h/2e$  contributions reveal the different decay rates. Thus, the summation of three ingredients of the current correlation would not be zero.

The variations of the current correlations are plotted with the phase  $\phi$  at  $\Phi/\Phi_0 = 0.25$  subject to different temperatures. Other parameters are chosen as those in Fig. 3.5. Similar to the adiabatic variations of the low temperature condition, the  $\cos\phi$  behavior of the current correlation is found. However, the larger temperatures become, the smaller amplitudes of the current correlations are found. From Eqs. (C.24)-(C.26), the dependence of  $\cos\phi$  appears only in the  $h/e$  contribution. Thus, the smeared rate of the amplitudes is with the form  $\exp(-\pi k_B T/E_c) [1 + (k_B T/E_c)^2]$ . The temperature shift of the  $\cos\phi$  oscillations depends on the mixed temperature decaying rates of the flux-dependent and the flux-independent parts. Note that, at the low frequency regime the order of the shot noise may be too small and hard to be detected by the measuring equipment. Although the visible signal could be found by increasing the pump amplitude, the specific variations would not be shown. We hope in the near future those interesting phenomena could be observed.

*Summary*— The characteristics of shot noise in pump-driven Mach-Zehnder interferometers (MZI) are investigated at the low temperature and the low frequency conditions. At the low temperature condition the shot noise grows negatively with some small oscillations with increasing the frequency. The negative values of the shot noise shows the nature of fermion. The period in frequency of the shot noise is found as a common multiple of the frequency  $2\pi/\tau_L$  and  $2\pi/\tau_R$ . Contrary to the shot noise, the currents vary with the frequency up and down around zero. Thus, some regimes show the occurrence of the noise while with zero currents. Tuning the

additional phase  $\phi$  and the magnetic phase  $\Phi/\Phi_0$ , the shot noises show some valley structures in the adiabatic and the non-adiabatic conditions. Contrary to the non-adiabatic consideration, the noiseless regimes are found in the adiabatic consideration. The variations of the shot noises with the additional phases  $\phi$  become simply as a function of  $\cos\phi$  in the adiabatic condition. In the non-adiabatic condition, the complicate phase dependence is involved. In the other hand, at the low frequency condition, the temperature smears one flux-independent part and two flux-dependent parts of the shot noise with different decay rates. Contrary to the currents, the shot noise are totally suppressed. The noiseless regimes and the  $\cos\phi$  variations of the shot noise are also found at the low frequency condition. However, as the temperature increasing the noiseless regimes are removed and the  $\cos\phi$  variations of the shot noise are suppressed.



## References

- [1] M. Switkes, C. M. Marcus, K. Campman, and A. C. Gossard, “An Adiabatic Quantum Electron Pump,” *Science*, vol. 283, pp. 1905–1908, Mar. 1999.
- [2] P. W. Brouwer, “Scattering approach to parametric pumping,” *Phys. Rev. B*, vol. 58, pp. R10135–R10138, Oct. 1998.
- [3] D. J. Thouless, “Quantization of particle transport,” *Phys. Rev. B*, vol. 27, pp. 6083–6087, May 1983.
- [4] M. Büttiker, H. Thomas, and A. Prêtre, “Current partition in multiprobe conductors in the presence of slowly oscillating external potentials,” *Z. Phys. B: Condens. Matter*, vol. 94, pp. 133–137, Mar. 1994.
- [5] B. Spivak, F. Zhou, and M. T. Beal Monod, “Mesoscopic mechanisms of the photovoltaic effect and microwave absorption in granular metals,” *Phys. Rev. B*, vol. 51, pp. 13226–13230, May 1995.
- [6] F. Zhou, B. Spivak, and B. Altshuler, “Mesoscopic Mechanism of Adiabatic Charge Transport,” *Phys. Rev. Lett.*, vol. 82, pp. 608–611, Jan. 1999.
- [7] T. A. Shutenko, I. L. Aleiner, and B. L. Altshuler, “Mesoscopic fluctuations of adiabatic charge pumping in quantum dots,” *Phys. Rev. B*, vol. 61, pp. 10366–10375, Apr. 2000.
- [8] J. E. Avron, A. Elgart, G. M. Graf, and L. Sadun, “Geometry, statistics, and asymptotics of quantum pumps,” *Phys. Rev. B*, vol. 62, pp. R10618–R10621, Oct. 2000.
- [9] M. G. Vavilov, V. Ambegaokar, and I. L. Aleiner, “Charge pumping and photovoltaic effect in open quantum dots,” *Phys. Rev. B*, vol. 63, pp. 195313–195324, Apr. 2001.
- [10] B. Wang, J. Wang, and H. Guo, “Parametric pumping at finite frequency,” *Phys. Rev. B*, vol. 65, pp. 073306–073309, Jan. 2002.

- [11] M. Moskalets and M. Büttiker, “Dissipation and noise in adiabatic quantum pumps,” *Phys. Rev. B*, vol. 66, pp. 035306–035314, Jul. 2002.
- [12] M. L. Polianski and P. W. Brouwer, “Scattering matrix ensemble for time-dependent transport through a chaotic quantum dot,” *J. Phys. A: Math. Gen.*, vol. 36, pp. 3215–3236, Mar. 2003.
- [13] J. E. Avron, A. Elgart, G. M. Graf, and L. Sadun, “Transport and Dissipation in Quantum Pumps,” *J. Stat. Phys.*, vol. 116, pp. 425–473, Aug. 2004.
- [14] M. Martinez-Mares, C. H. Lewenkopf, and E. R. Mucciolo, “Statistical fluctuations of pumping and rectification currents in quantum dots,” *Phys. Rev. B*, vol. 69, pp. 085301–085312, Feb. 2004.
- [15] H.-Q. Zhou, U. Lundin, S. Y. Cho, and R. H. McKenzie, “Measuring geometric phases of scattering states in nanoscale electronic devices,” *Phys. Rev. B*, vol. 69, pp. 113308–113311, Mar. 2004.
- [16] D. Shin and J. Hong, “Electron transport in the Aharonov-Bohm pump,” *Phys. Rev. B*, vol. 70, pp. 073301–073304, Aug. 2004.
- [17] S.W. Chung, C.S. Tang, C.S. Chu, and C.Y. Chang, “Finger-gate array quantum pumps: Pumping characteristics and mechanisms,” *Phys. Rev. B*, vol. 70, pp. 085315–085321, Aug. 2004.
- [18] M. Governale, F. Taddei, R. Fazio and F.W.J. Hekking, “Adiabatic Pumping in a Superconductor-Normal-Superconductor Weak Link,” *Phys. Rev. Lett.*, vol. 95, pp. 256801–256804, Dec. 2005.
- [19] D. Cohen, T. Kottos, and H. Schanz, “Quantum pumping: The charge transported due to a translation of a scatterer,” *Phys. Rev. E*, vol. 71, pp. 035202(R)–035205(R), Mar. 2005.
- [20] C. Benjamin, “Detecting a true quantum pump effect,” *Eur. Phys. J. B*, vol. 52, pp. 403–410, Jul. 2006.

- [21] P. W. Brouwer, “Rectification of displacement currents in an adiabatic electron pump,” *Phys. Rev. B*, vol. 63, pp. 121303(R)–121304(R), Mar. 2001.
- [22] L. DiCarlo, C.M. Marcus, and J.S. Harris, Jr, “Photocurrent, Rectification, and Magnetic Field Symmetry of Induced Current through Quantum Dots,” *Phys. Rev. Lett.*, vol. 91, pp. 246804–246807, Dec. 2003.
- [23] R. Citro and F. Romeo, “Pumping in a mesoscopic ring with Aharonov-Casher effect,” *Phys. Rev. B*, vol. 73, pp. 233304–233307, Jun. 2006.
- [24] S.K. Kim, K.K. Das, and A. Mizel, “Adiabatic quantum pumping in an Aharonov-Bohm loop and in a Si-like nanowire: interference in real space and in k-space,” cond-mat/0609601, Sep. 2006.
- [25] P. Samuelsson and M. Büttiker, “Dynamic generation of orbital quasiparticle entanglement in mesoscopic conductors,” *Phys. Rev. B*, vol. 71, pp. 245317–245321, Jun. 2005.
- [26] M. Moskalets and M. Büttiker, “Floquet scattering theory of quantum pumps,” *Phys. Rev. B*, vol. 66, pp. 205320–205339, Nov. 2002.
- [27] M. Moskalets and M. Büttiker, “Adiabatic quantum pump in the presence of external ac voltages,” *Phys. Rev. B*, vol. 69, pp. 205316–205327, May 2004.
- [28] S.W. Kim, “Floquet scattering in parametric electron pumps,” *Phys. Rev. B*, vol. 66, pp. 235304–235309, Dec. 2002.
- [29] M. Büttiker, “Scattering theory of current and intensity noise correlations in conductors and wave guides,” *Phys. Rev. B*, vol. 46, pp. 12485–12507, Nov. 1992.
- [30] M. Moskalets and M. Büttiker, “Magnetic-field symmetry of pump currents of adiabatically driven mesoscopic structures,” *Phys. Rev. B*, vol. 72, pp. 035324–035334, Jul. 2005.
- [31] V. S.-W. Chung, P. Samuelsson, and M. Büttiker, “Visibility of current and shot

- noise in electrical Mach-Zehnder and Hanbury Brown Twiss interferometers,” *Phys. Rev. B*, vol. 72, pp. 125320–125332, Sep. 2005.
- [32] H. A. Fertig, “Semiclassical description of a two-dimensional electron in a strong magnetic field and an external potential,” *Phys. Rev. B*, vol. 38, pp. 996–1015, Jul. 1988.
- [33] M. Büttiker and M. Moskalets, “Scattering Theory of Dynamic Electrical Transport,” *Lecture Notes in Physics*, vol. 690, pp. 33-44, Sep. 2006.
- [34] T. Christen and M. Büttiker, “Gauge-invariant nonlinear electric transport in mesoscopic conductors,” *Europhys. Lett.*, vol. 35, pp. 523–528, Sep. 1996.
- [35] M. H. Pedersen and M. Büttiker, “Scattering theory of photon-assisted electron transport,” *Phys. Rev. B*, vol. 58, pp. 12993–13006, Nov. 1998.
- [36] M. Büttiker, “Role of quantum coherence in series resistors,” *Phys. Rev. B*, vol. 33, pp. 3020–3026, Mar. 1986.
- [37] M. Büttiker, “Coherent and sequential tunneling in series barriers,” *IBM J. Res. Dev.*, vol. 32, pp. 63–75, Jan. 1988.
- [38] Ya. M. Blanter and M. Büttiker, “Shot noise in mesoscopic conductors,” *Phys. Rep.*, vol. 336, pp. 1–166, Sep. 2000.
- [39] C. Texier and M. Büttiker, “Effect of incoherent scattering on shot noise correlations in the quantum Hall regime,” *Phys. Rev. B*, vol. 62, pp. 7454–7458, Sep. 2000.
- [40] F. Marquardt and C. Bruder, “Influence of Dephasing on Shot Noise in an Electronic Mach-Zehnder Interferometer,” *Phys. Rev. Lett.*, vol. 92, pp. 56805–56808, Feb. 2004.
- [41] F. Marquardt and C. Bruder, “Effects of dephasing on shot noise in an electronic Mach-Zehnder interferometer,” *Phys. Rev. B*, vol. 70, pp. 125305–125320, Sep. 2004.



- [42] S. Oberholzer, E. Bieri, C. Schönenberger, M. Giovannini, and J. Faist, “Positive Cross Correlations in a Normal-Conducting Fermionic Beam Splitter,” *Phys. Rev. Lett.*, vol. 96, pp. 46804–46807, Feb. 2006.
- [43] M. Moskalets and M. Büttiker, “Effect of inelastic scattering on parametric pumping,” *Phys. Rev. B*, vol. 64, pp. 201305(R)–201308(R), Oct. 2001.
- [44] J.N.H.J. Cremers and P.W. Brouwer, “Dephasing in a quantum pump,” *Phys. Rev. B*, vol. 65, pp. 115333–115339, Mar. 2002.
- [45] M. L. Polianski, P. Samuelsson, and M. Büttiker, “Shot noise of photon-excited electron-hole pairs in open quantum dots,” *Phys. Rev. B*, vol. 72, pp. 161302(R)–161305(R), Oct. 2005.
- [46] S. Pilgram, P. Samuelsson, H. Förster, and M. Büttiker, “Full-Counting Statistics for Voltage and Dephasing Probes,” *Phys. Rev. Lett.*, vol. 97, pp. 066801–066804, Aug. 2006.
- [47] H. Förster, P. Samuelsson, S. Pilgram, and M. Büttiker, “Voltage and dephasing probes: a full counting statistics discussion,” *Phys. Rev. B*, vol. 75, p.p. 035340-035356, Jan. 2007.
- [48] M.L. Polianski, and P.W. Brouwer, “Pumped current and voltage for an adiabatic quantum pump,” *Phys. Rev. B*, vol. 64, pp. 075304–075309, Jul. 2001.
- [49] Y. Ji, Y. Chung, D. Sprinzak, M. Heiblum, D. Mahalu, and H. Shtrikman, “An electronic Mach–Zehnder interferometer,” *Nature*, vol. 422, pp. 415–418, Mar. 2003.
- [50] I. Neder, M. Heiblum, Y. Levinson, D. Mahalu, and V. Umansky, “Unexpected Behavior in a Two-Path Electron Interferometer,” *Phys. Rev. Lett.*, vol. 96, pp. 016804–016807, Jan. 2006.
- [51] L. V. Litvin, H.-P. Tranitz, W. Wegscheider, and C. Strunk, “Decoherence and single electron charging in an electronic Mach-Zehnder interferometer,” *Phys.*

- Rev. B*, vol. 75, pp. 033315–033318, Jan. 2007.
- [52] P. Samuelsson, E.V. Sukhorukov and M. Büttiker, “Two-Particle Aharonov-Bohm Effect and Entanglement in the Electronic Hanbury Brown–Twiss Setup,” *Phys. Rev. Lett.*, vol. 92, pp. 026805–026809, Jan. 2004.
- [53] C.W.J. Beenakker, C. Emary, M. Kindermann, and J.L. van Velsen, “Proposal for Production and Detection of Entangled Electron-Hole Pairs in a Degenerate Electron Gas,” *Phys. Rev. Lett.*, vol. 91, pp. 147901–147904, Oct. 2003.
- [54] T. M. Stace, C. H. W. Barnes, and G. J. Milburn, “Mesoscopic One-Way Channels for Quantum State Transfer via the Quantum Hall Effect,” *Phys. Rev. Lett.*, vol. 93, pp. 126804–126807, Sep. 2004.
- [55] C.W.J. Beenakker, M. Titov, and B. Trauzettel, “Optimal Spin-Entangled Electron-Hole Pair Pump,” *Phys. Rev. Lett.*, vol. 94, pp. 186804–186807, May 2005.
- [56] K. K. Das, S. Kim, and A. Mizel, “Controlled Flow of Spin-Entangled Electrons via Adiabatic Quantum Pumping,” *Phys. Rev. Lett.*, vol. 97, pp. 096602–096605, Aug. 2006.
- [57] A. V. Lebedev, G. B. Lesovik, and G. Blatter, “Generating spin-entangled electron pairs in normal conductors using voltage pulses,” *Phys. Rev. B*, vol. 72, pp. 245314–245321, Dec. 2005.
- [58] M. Moskalets and M. Büttiker, “Multiparticle correlations of an oscillating scatterer,” *Phys. Rev. B*, vol. 73, pp. 125315–125320, Mar. 2006.
- [59] G. Platero and R. Aguado, “Photon-assisted transport in semiconductor nanostructures,” *Phys. Rep.*, vol. 395, pp. 1-157, May 2004.
- [60] P. F. Bagwell and R. K. Lake, “Resonances in transmission through an oscillating barrier,” *Phys. Rev. B*, vol. 46, pp.15329-15336, Aug. 1992.
- [61] M. Moskalets and M. Büttiker, “Floquet scattering theory for current and heat

noise in large amplitude adiabatic pumps”, *Phys. Rev. B*, vol. **70**, pp. 245305-245319, Dec. 2004.

- [67] Preden Roulleau, F. Portier, D. C. Glattli, P. Roche G. Gaini, U. Gennser, D. Maily,” High visibility in an electronic Mach-Zehnder interferometer with random phase fluctuations,” cond-mat\0704.0746, April, 2007.



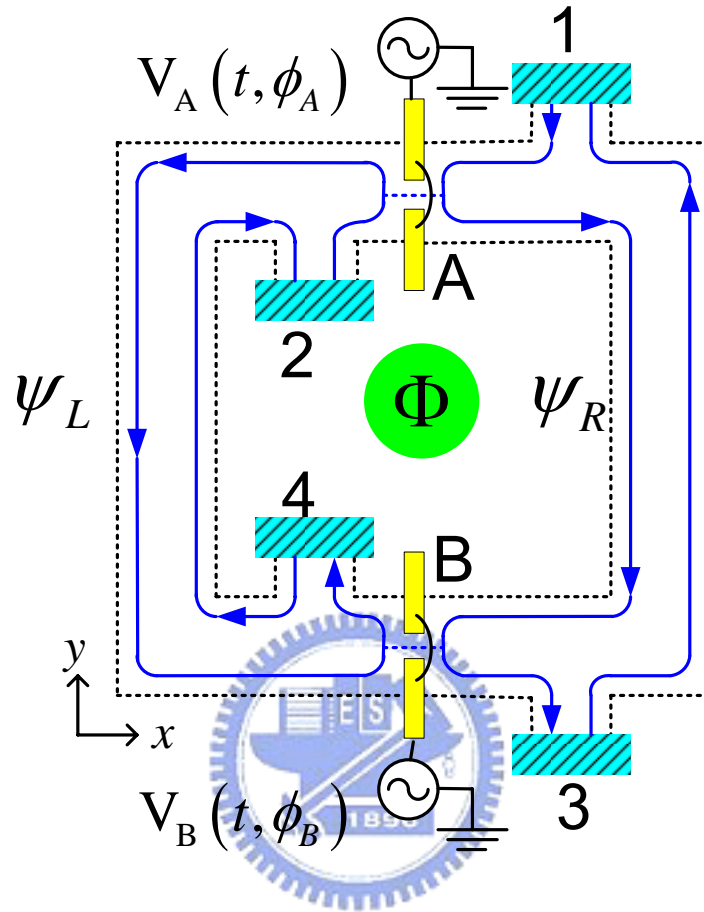


Fig. 3.1 The pump driven MZI implemented in a conductor in the quantum Hall regime, supporting a single, unidirectional edge state. The conductor is connected to four reservoirs  $\alpha = 1$  to  $4$  kept at the same potential. Two electrostatic split gates, at  $A$  and  $B$ , are acting as QPCs. The corresponding gate potentials  $V_A(t, \phi_A)$  and  $V_B(t, \phi_B)$ , with  $\phi_A$  and  $\phi_B$  the pumping phases, vary periodically in time. The time dependent potentials give rise to scattering in both real and energy space and are driving the pump current. An Aharonov-Bohm flux  $\Phi$  threads the MZI.

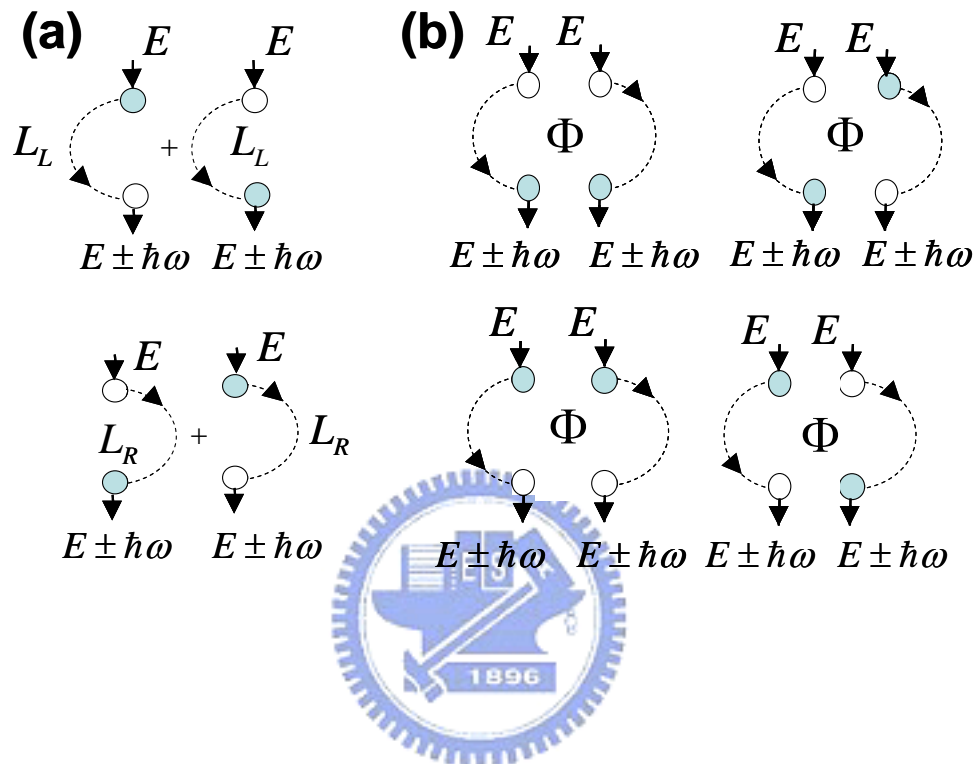


Fig. 3.2 Two qualitatively different types of first order photon-assisted interference processes contributing to the current: (a) along the same spatial paths L or R and (b) along the different spatial paths L and R. The paths in (b) are sensitive to the enclosed flux  $\Phi$ . Filled balls indicate inelastic scattering, the electrons pick up or lose one quantum of energy  $\hbar\omega$ , while empty balls indicate elastic scattering.

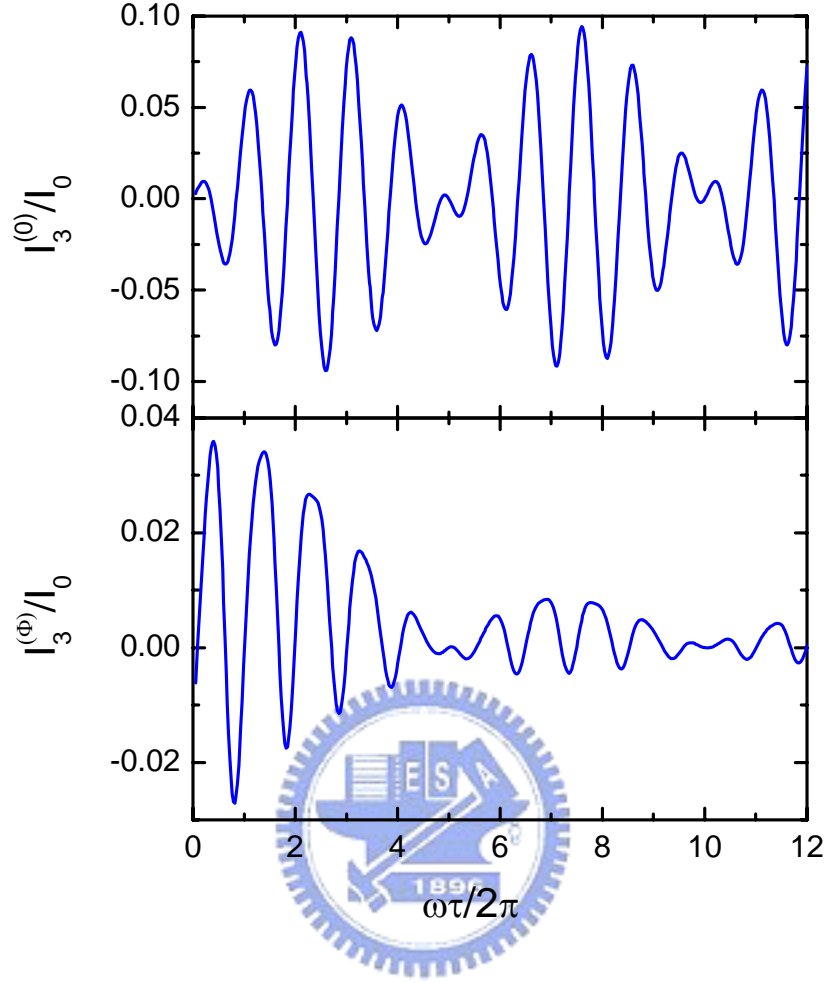


Fig. 3.3 The flux independent current  $I_3^{(0)}$  (upper panel) and the flux dependent current  $I_3^{(\Phi)}$  (lower panel) as a function of pump frequency. Guided by the experiments in Ref. [50], [51], we have taken an asymmetry,  $\tau = 5\hbar/E_c$ , and symmetric static beam splitters,  $a_A = a_B = 1$ . The other parameters are  $b_A = 0.4, b_B = 1.3$  (strong pumping),  $\phi_A = 0$ ,  $\phi_B = 0.8\pi$  and  $\psi_{LR} = 0.8\pi$ .

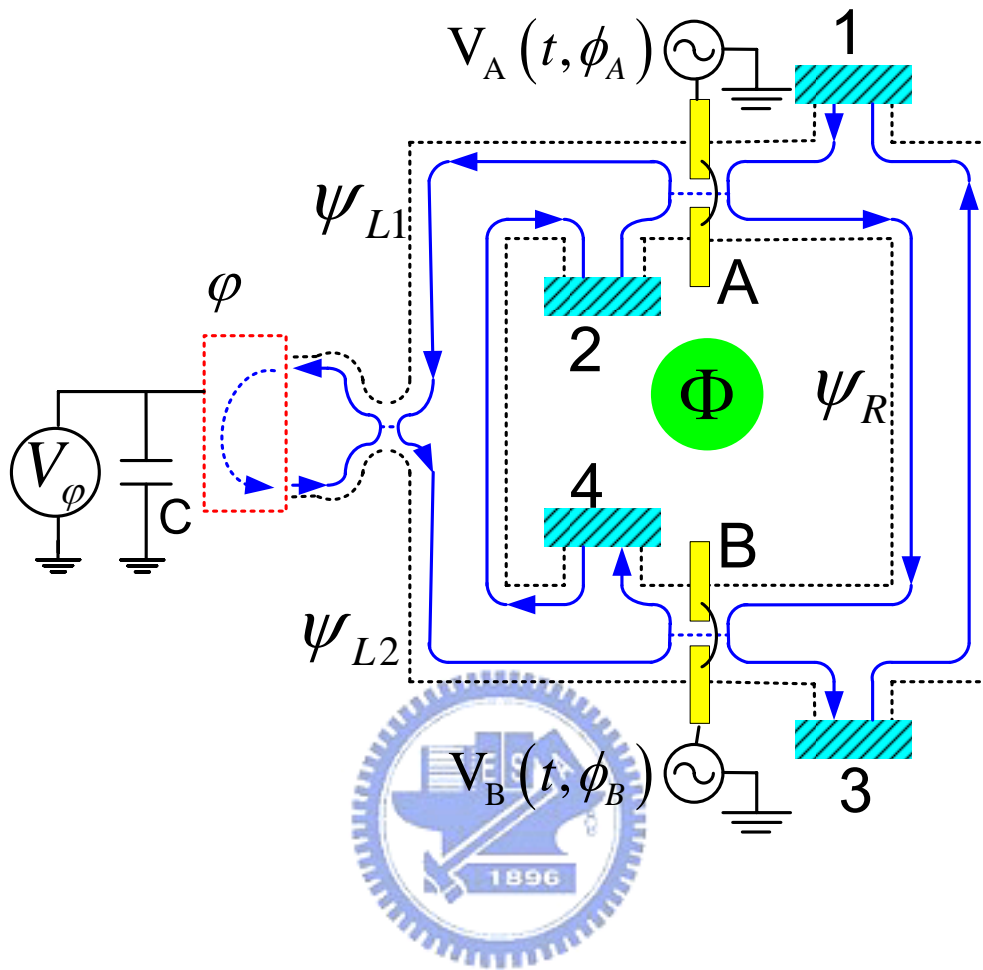


Fig. 3.4 The pump driven MZI of Fig. 3.1 with the left arm connected with strength  $\epsilon$  to a voltage probe  $\phi$ . The dynamics of the potential  $V_\phi$  of the probe is governed by the charge relaxation time (see text).

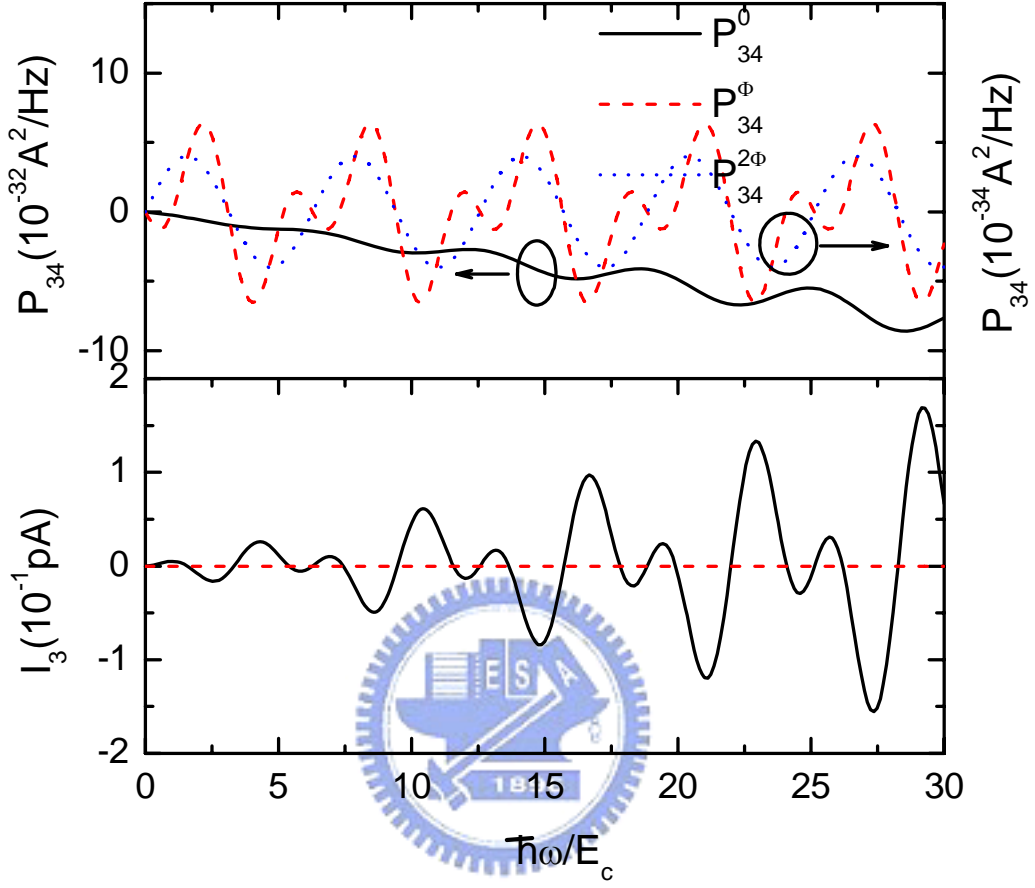


Fig. 3.5 At the low temperature condition  $k_B T \ll \hbar\omega$ , the variations of the flux-independent part  $P_{34}^{(0)}$  and the flux-dependent parts  $P_{34}^{(\Phi)}$ ,  $P_{34}^{(2\Phi)}$  of the shot noises (the up panel) and the currents (the down panel) are plotted with respective to the pumping frequency. The parameters are shown in the text.



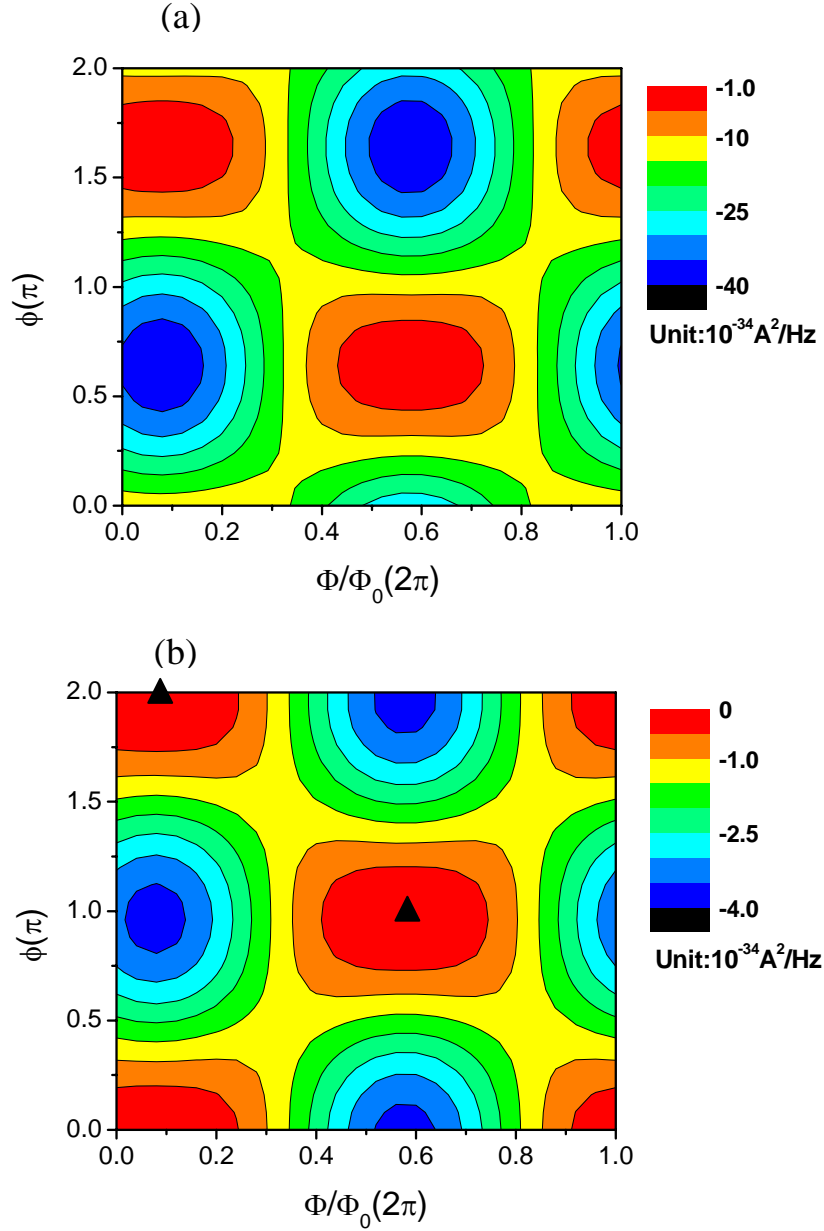


Fig. 3.6 At the low temperature condition  $k_B T \ll \hbar \omega$ , the shot noises  $P_{34}$  are shown as a function of the phase differences  $\phi = \phi_B - \phi_A$  and the magnetic phases  $\Phi/\Phi_0$  subject to the frequencies (a)  $\omega = 15 \text{ GHz}$  and (b)  $\omega = 1.43 \text{ GHz}$ . Contrary to the non-adiabatic, large frequency condition, the noiseless regimes (denoted by triangle) are found at the adiabatic, low frequency condition.

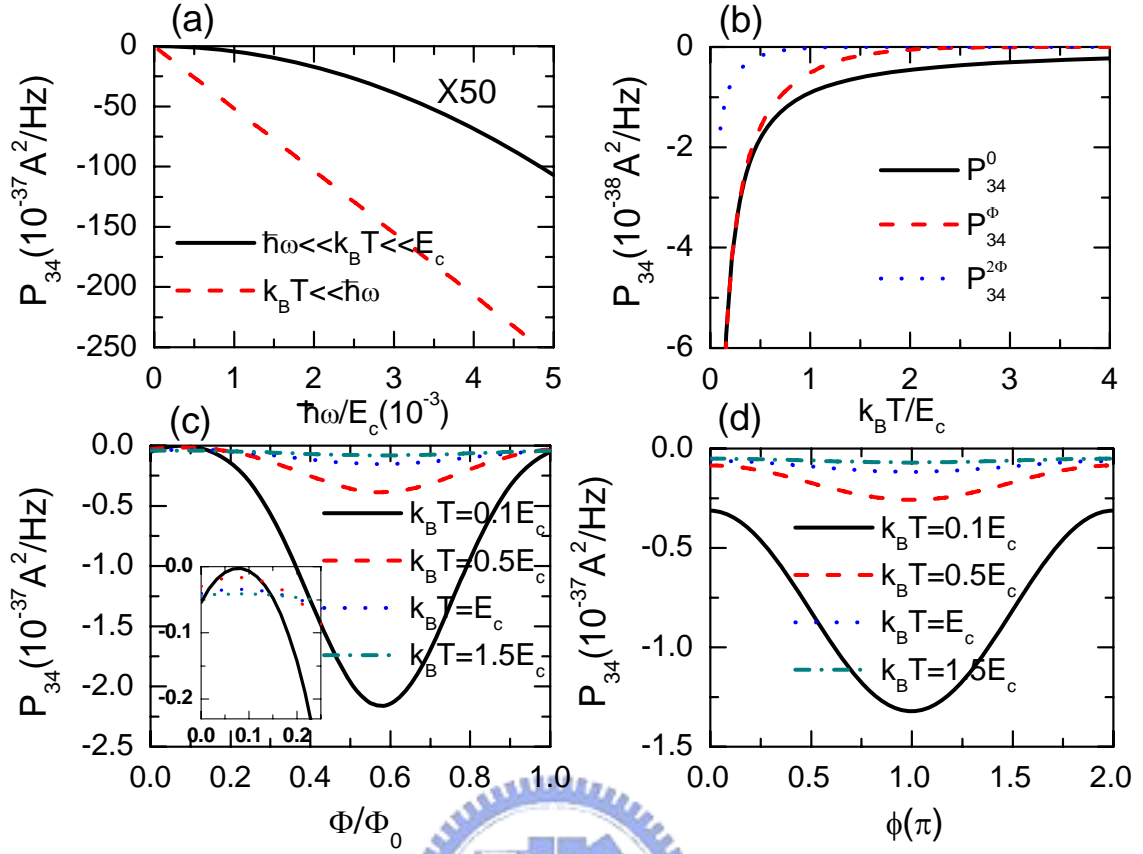


Fig. 3.7 (a) In the adiabatic limit, the current correlations vary with the frequency at the conditions:  $k_B T \ll \hbar\omega$  and  $\hbar\omega \ll k_B T \ll E_c$  (the second inequality ensures no thermal effects). At the low frequency condition  $\hbar\omega \ll k_B T$ , we find that (b) the decaying of three parts of current correlations  $P_{34}^{(0)}$ ,  $P_{34}^{(\Phi)}$  and  $P_{34}^{(2\Phi)}$  with respect to the temperature; (c) contrary to fig. 3(b), at  $\phi = 0$  and  $\Phi/\Phi_0 = 0.75$  the temperature suppresses the amplitudes of the current correlations and removes the noiseless regime, enlarged in the inset; (d) contrary to fig. 3(b) along  $\Phi/\Phi_0 = 0.25$ , the cosine behaviors of the current correlations are smeared as increasing temperature. Other parameters are shown in the text.

## Chapter 4

# Finger-gate array quantum pumps: pumping characteristics and mechanisms

### 4.1 Introduction of potential array pumping

Quantum charge pumping (QCP) has become an active field, [1-21] since the experiment has been reported by Switkes *et al.* [4]. The configuration of the experiment was that a quantum dot patterned by some metal gates on the two dimensional electron gases was modulated slowly by two electrostatic gates. Two gates are ac biased by the same frequency but differed by a tunable phase difference. DC response across the source and drain electrodes is the signature of the QCP. The further intensive studies of QCP were explored in various systems: quantum dots, [6-8] double-barrier quantum wells, [9] pumped voltage, [12] noiseless AQP, [13] heat current, [14] incoherent processes, [15, 16] quantum rings, [19, 20] and interacting wires. [21]

Original proposal of QCP, in the adiabatic regime, was due to Thouless. [1] He considered the current generated by a slowly varying traveling wave in an isolated one-dimensional system. The number of electrons transported per period was found to be quantized if the Fermi energy lies in a gap of the spectrum of the instantaneous Hamiltonian. Latter, Niu proposed variational one-dimensional periodic potentials for the adiabatic quantum pumping (AQP) and pointed out the importance of the quantized charge pumping in utilizing it for a direct-current standard. [2]

Surface acoustic waves (SAW) were alternate experimental efforts in generating AQP. [22-26] An interdigitated transducer located deep on an end-region of a narrow channel produced the SAW propagating to the other end-region of the narrow channel. A wave of electrostatic potential was induced inside the channel. The trapped electrons in the minima of the potentials transport along the narrow channel. Both Mott-Hubbard electron-electron repulsion in each such trap and the adiabaticity in the transport were needed to give rise to the quantization of the pumped current. [23] As such, the channel has to be operated in the pinch-off regime. [24]

In this chapter, we propose to study yet another experimental configuration for QCP in a narrow channel. The potential waves are generated by a FGA pair, which consists of  $N$  finger gates (FG's) in each FGA, shown in Fig. 4.1. One cell of a FGA pair comprises two FG's. Each FGA is modulated by ac potentials and with the same frequency. A phase difference  $\phi$  is kept between two FGAs. As the number of FG's  $N > 2$ , the time-dependent Bragg reflections become the dominant mechanisms of QCP, no longer solely the processes of the photon-assisted interferences.

## 4.2 FGA pair model

The potential  $V(x, t)$  in a narrow constriction induced by a FGA pair is represented by

$$V(x, t) = \sum_{i=1}^N V_{1i}(x) \cos(\Omega t) + V_{2i}(x) \cos(\Omega t + \phi), \quad (4.1)$$

where  $N$  is the number of FG's per FGA. We assume that the ac biased FG's in  $i$ -th cell are localized, respectively, at positions  $x_i$  and  $x_i + \delta x_i$ , namely that  $V_{1i}(x) = V_1 \delta(x - x_i)$  and  $V_{2i}(x) = V_2 \delta(x - x_i - \delta x)$  with a relative phase

difference  $\phi$ . These FG's of two FGAs are evenly spaced, with a pitch  $d$ , and are located at  $x_i = (i-1)d$  for one FGA and  $x_i + \delta x$  for the other. The relative shift between the FGA pair is  $\delta x = \alpha d$ , where  $0 < \alpha < 1$ . In the following, we consider the case of the same modulation amplitude  $V_1 = V_2 = V_0$ . Depending on the choice of the values for  $\phi$  and  $\alpha$ ,  $V(x, t)$  will be either predominantly of a propagating or a standing wave type. A main form of waves can be found from taking the lowest order Fourier component of  $V(x, t)$ , given by

$$V_1 = \frac{2V_0}{d} \{ \cos Kx \cos \Omega t + \cos[K(x - \delta x)] \cos(\Omega t + \phi) \}, \quad (4.2)$$

where  $K = 2\pi/d$ . For our purposes in this chapter, an optimal choice is  $\phi = \pi/2$  and  $\alpha = 1/4$ , in which  $V(x, t)$  is a predominant left-going wave.

The Hamiltonian of the system is  $H = H_y + H_x(t)$  in a dimensionless form, where  $H_y = -\partial^2/\partial y^2 + \omega_y^2 y^2$  contains a transverse confinement, leading to subband energies  $\varepsilon_n = (2n+1)\omega_y$ . The time-dependent part of the Hamiltonian  $H_x(t)$  is of the form  $H_x(t) = -\partial^2/\partial x^2 + V(x, t)$ . Here the appropriate units of the Hamiltonian have been chosen similarly that in Ref. 27.

In the QCP system, the chemical potential  $\mu$  is the same in all reservoirs. Thus the pumped current, at zero temperature, can be expressed as [10]

$$I = -\frac{2e}{h} \int_0^\mu dE [T_{\rightarrow}(E) - T_{\leftarrow}(E)] \quad (4.3)$$

Here the total current transmission coefficients include the contributions by electrons which are incident at energy  $E$  of subband  $n$  and may absorb ( $|m| > 0$ ) or emit ( $-|m| < 0$ )  $m\Omega$  to energy  $E_m = E + m\Omega$  by the FG pumping potentials, given by

$$T_{\rightarrow(\leftarrow)}(E) = \sum_{n=0}^{N_s-1} \sum_{m=-\infty}^{\infty} T_{n\rightarrow(\leftarrow)}(E_m, E), \quad (4.4)$$

where  $N_s$  stands for the number of occupied subbands. The summations are over all the propagating modes of the transmitted electrons and include both the subband index  $n$  and the sideband index  $m$ . The subscripted arrow in the total current transmission coefficient indicates the propagating direction of electrons. These coefficients are calculated numerically by the Floquet scattering matrix method (shown in appendix A of chapter 3).

### 4.3 Numerical results

In this section, we present the numerical results for the pumping characteristics of either a single-FG pair ( $N = 1$ ) or a *finite* FGA pair ( $N > 2$ ). In these two cases that the pumping characteristics are due to different inelastic scattering processes. For definiteness, the unit scales in our numerical results are taken from the GaAs-Al<sub>x</sub>Ga<sub>1-x</sub>As based heterostructure. The values that we choose for our configuration parameters are  $\omega_y = 0.007$ , subband level spacing  $\Delta\varepsilon = 2\omega_y$  ( $\simeq 0.13$  meV),  $d = 40$  ( $\simeq 0.32$   $\mu$  m) and  $V_0 = 0.04$  ( $\simeq 28.7$  meV $\text{\AA}$ ). From the value of  $V_0$ , and the assumed FG width  $\sim 0.05$   $\mu$  m, the amplitude of the potential induced by a FG is  $\sim 0.057$  mV.

#### 4.3.1 Single FG pair case

In this subsection we investigate the pumping characteristics for the case of a single-FG pair. Figure 4.2 presents the dependence of the total current transmission coefficients on the incident electron energy  $E$ . We replace  $E$  by

$$X_E = \frac{E}{\Delta\varepsilon} + \frac{1}{2}, \quad (4.5)$$

whose integral value corresponds to the propagating subband in the narrow channel. The chosen pumping frequency is as  $\Omega = 0.6\Delta\varepsilon$  ( $\Omega/2\pi \simeq 18$  GHz) in Fig. 4.2(a) and  $\Omega = 0.1\Delta\varepsilon$  ( $\Omega/2\pi \simeq 3$  GHz) in Fig. 4.2(b). We select the phase  $\phi = \pi/2$  and the fractional constant  $\alpha = 1/4$ .

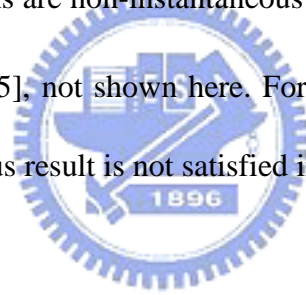
At integral values of  $X_E$ , the total current transmission coefficients  $T_{\rightarrow(\leftarrow)}(X_E)$  exhibit abrupt changes. This is due to the changes in the number of contributed propagating subbands in the narrow channel. Between integral values of  $X_E$ ,  $T_{\rightarrow(\leftarrow)}$  both show dip structures. The dip structures are located at  $X_{\text{dip}} = N_s + 0.6$  in Fig. 4.2(a) and at  $X_{\text{dip}} = N_s + 0.1$  in Fig. 4.2(b). These dip structure locations are the same for both  $T_{\rightarrow}$  and  $T_{\leftarrow}$ , and show resonant structures associated with inelastic scattering that causes an electron to jump into a quasibound state (QBS) just beneath a subband bottom. [28] The peak structures at  $X_E = N_s + 0.2$  in  $T_{\leftarrow}$  of Fig. 4.2(b) are  $2\Omega$  resonant structures.

In Fig. 4.2, we see that  $T_{\leftarrow}(X_E)$  does not equal to  $T_{\rightarrow}(X_E)$ , which allows the occurrence of the pumped current. Moreover, in our chosen parameters, between integral values of  $X_E$  we find  $T_{\leftarrow} > T_{\rightarrow}$  ( $T_{\leftarrow} < T_{\rightarrow}$ ) on the left (right) region of a dip structure. This has an important bearing on the dependence of the pumped current on chemical potentials, as is shown in Fig. 4.3. Along  $X_E$ , the pumped current rises on the left region of  $X_{\text{dip}}$  and then drops on the right region of  $X_{\text{dip}}$ , in accord with the relative changes in  $T_{\rightarrow}$  and  $T_{\leftarrow}$  about the same  $X_{\text{dip}}$ . Hence the peaks of the pumped current depend on the pumping frequency at

$$X_E^{(\text{peak})} = N_s + \frac{\Omega}{\Delta\varepsilon}, \quad (4.6)$$

assuring that the occurred positions of the maximum pumped currents could be predicted by the aforementioned resonant inelastic process. The variations of  $T_{\rightarrow}$  and  $T_{\leftarrow}$ , as a result of the pumped currents, are due to the photon-assisted interferences and change with system parameters, e.g. the pumping frequency and the length of each cell of a FGA pair. [29]

Besides the trend that the pumped current in Fig. 4.3 drops with the pumping frequency, we would like to remark on a more interesting result: the instantaneous and the non-instantaneous regimes can be found in the same curve. Since the instantaneous condition is given by  $\mu \gg \Omega$ , the curve for  $\Omega = 0.1\Delta\varepsilon$  in the regions  $N_s + \Omega/\Delta\varepsilon < X_\mu \leq N_s + 1$  corresponds to the instantaneous regimes, while the other  $X_\mu$  regions are non-instantaneous regimes. This has been checked within the Brouwer method [5], not shown here. For the higher pumping frequency,  $\Omega = 0.6\Delta\varepsilon$ , the instantaneous result is not satisfied in the entire  $X_\mu$  region.



### 4.3.2 Finite FGA case

In this subsection, we present the numerical results for the pumping characteristics of a *finite* FGA pair. QCP for two prominent tuning modes are considered. These are (i) tuning the electron density by the *back-gate* technique and (ii) tuning the channel width by *split-gate* technique.

#### 4.3.2.a Tuning back-gate

We present the numerical results for the pumping characteristics of a FGA pair with  $N = 4$  that is realized by the *back-gate technique*. The dependence of the total current transmission probability on  $X_E$  is shown in Fig. 4.4, in which the



pumping frequencies are (a)  $\Omega = 0.6\Delta\varepsilon$  and (b)  $\Omega = 0.1\Delta\varepsilon$ . The choices of the parameters  $d$ ,  $\phi$  and  $\alpha$  are the same as those in the previous subsection, but the latter two parameters give rise here to an equivalent left-going wave in the pumping potential  $V(x,t)$ .

The curves in Fig. 4.4 show additional structures, other than the dip structures that have been discussed in the last subsection. These additional structures are valley structures that occur at different  $X_E$  values for  $T_{\rightarrow}(X_E)$  and  $T_{\leftarrow}(X_E)$ . In a region between two integral values of  $X_E$ , the valley structure of  $T_{\rightarrow}(X_E)$  occurs at a lower  $X_E$  than that of  $T_{\leftarrow}(X_E)$ . This shows clearly the breaking of the transmission symmetry by the pumping potentials. Furthermore, the valleys are separated by  $\Delta X_E = \Omega/\Delta\varepsilon$ . This can be understood from resonant coupling conditions  $\varepsilon_k = \varepsilon_{k-K} - \Omega$  and  $\varepsilon_{k+K} = \varepsilon_k - \Omega$  for, respectively, the right-going and the left-going  $k$ . From these conditions, the valley locations are at

$$k_{\pm}^2 = \left[ \frac{K}{2} \left( 1 \mp \frac{\Omega}{K^2} \right) \right]^2, \quad (4.7)$$

where the upper sign is for positive, or right-going,  $k$ . These locations, expressed in terms of  $X_E$ , are given by

$$X_E = N_s + \frac{k_{\pm}^2}{\Delta\varepsilon}, \quad (4.8)$$

and are at  $X_E = 1.19, 1.79, 2.19, 2.79, 3.19$  and  $3.79$  for the case of Fig. 4.4(a), and  $X_E = 1.39, 1.49, 2.39, 2.49, 3.39$  and  $3.49$  for the case of Fig. 4.4(b). The matching between these numbers and our numerical results in Fig. 4.4 is remarkable. In addition, the energy gaps are opened up at these  $k_{\pm}^2$  locations, causing the drop in the transmission and the formation of the valley structures. [10] All these results assure us that the time-dependent Bragg's reflection is the dominant resonant inelastic scattering in our FGA pair structure.

On the other hand, the instantaneous condition is here given by  $\varepsilon_{\text{gap}} \gg \Omega$ , where  $\varepsilon_{\text{gap}}$  is the *effective* energy gap of the Hamiltonian. [2] Since  $\varepsilon_{\text{gap}}$  is given by the widths of the valley structures, the contributions of the valleys to the pumped current are non-instantaneous in Fig. 4.4(a) as a result of the well-separated valleys and instantaneous in Fig. 4.4(b) due to the overlap of the valleys.

In Fig. 4.5, we present the  $X_\mu$  dependence of the pumped current for the cases in Fig. 4.4. The pumped current peaks at the places that lie in the middle between a valley of  $T_\rightarrow(X_E)$  and the corresponding valley of  $T_\leftarrow(X_E)$ . The locations are around

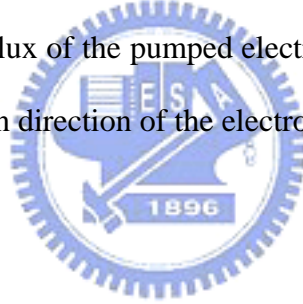
$$X_\mu = \mathcal{N}_S + \frac{K^2}{4\Delta\varepsilon} \left( 1 + \frac{\Omega^2}{K^4} \right), \quad (4.9)$$

which depends on both the pitch  $d$  and the pumping frequency  $\Omega$ . The peaks have flat tops for the solid curve, when  $\Omega = 0.6\Delta\varepsilon$ . Comparing with the total current transmission curves in Fig. 4.4(a), we see that the flat-topped peak profile is associated with the complete separation between the valleys of  $T_\rightarrow(X_E)$  and  $T_\leftarrow(X_E)$ . This is in the non-instantaneous regime. In contrast, for the case with the valleys overlapping, such as those in Fig. 4.4(b), the pumped current no longer peaks with a flat-top profile, as is shown by the dashed curve in Fig. 4.5. This is in the instantaneous regime. Meanwhile, their peak values are lowered. It is because the cancellation sets in when the valleys overlap. We note that the pumped currents are of order nA.

The robustness of the time-dependent Bragg reflection, on the other hand, is demonstrated most convincingly by the number of charge pumped per cycle at the maximum  $I_{\text{Max}}$  of the pumped current. In the dashed curve of Fig. 4.5, the pumped charge per cycle per spin state  $Q_P = (2\pi/\Omega)I_{\text{Max}}/2e = 0.495$ , where  $I_{\text{Max}} = 0.48$  nA and  $\Omega = 0.1\Delta\varepsilon \approx 3.03$  GHz. To get a unity, or quantized,

charge pumped per cycle per spin state, one can fix the pumping frequency  $\Omega = 0.1\Delta\varepsilon$ ,  $N = 4$ ,  $\phi = \pi/2$ , and  $d = 40$ , then tune the other pumping parameters as  $V_0 = 0.09$  and  $\alpha = 0.15$  to obtain  $Q_P = 0.992$  at  $X_\mu = 3.465$  (not shown here). In this frequency regime, the pumping would be expected to be adiabatic, according to Thouless [1] and Niu [2] when  $\varepsilon_{\text{gap}} \gg \Omega$ . However, in our case here, the energy gap is at best only partially opened, as we can see from the nonzero transmission in Fig. 4.4(b), because we have only  $N = 4$  FG pairs. Thus, our result shows that the condition of the occurrence of the AQP is less stringent than we would have expected originally. [2] In other words, the pumping effect of our FAG configuration is robust.

It is also worth pointing out that the pumped currents are positive in Fig. 4.5, showing that the net number flux of the pumped electrons is from right to left. This is consistent with the propagation direction of the electrostatic wave in  $V(x, t)$ . [10]



### 4.3.2.b Tuning split-gate

Thus far, we have explored the dependence of the FGA pair's QCP characteristics on electron energy by the use of the back-gate technique. Another way of tuning the QCP characteristics is via the modulation of the channel width (or subband level spacing  $\Delta\varepsilon$ ). This can be realized experimentally by the use of the so-called *split-gate technique*. Hence we present, in Fig. 4.6, the transverse confinement dependence of both the total current transmission probability and the pumped current. The transverse confinement is depicted by

$$X_N = \frac{\mu}{\Delta\varepsilon} + \frac{1}{2}, \quad (4.10)$$

which is related to the effective channel width and whose integral value corresponds to the number of propagating subbands in the channel. In this mode of tuning the QCP characteristics,  $\mu$  is fixed.

In Fig. 4.6(a), except for  $\mu$ , which is fixed at 0.049, and  $\omega_y$ , which varies with  $X_N$ , other parameters such as  $\Omega = 0.0084$ ,  $\phi = \pi/2$ , and  $\alpha = 1/4$  are the same as those in Fig. 4.4(a). The solid (dashed) curve is for  $T_{\rightarrow}$  ( $T_{\leftarrow}$ ). Both the features of the QBS and the time-dependent Bragg reflection are found. The expected locations of the QBS, given by the expression

$$X_N = \frac{1}{2} + \left(n + \frac{1}{2}\right) \frac{\mu}{\mu - \Omega}, \quad (4.11)$$

are at 1.1, 2.3 and 3.5, and they match the QBS locations in Fig. 4.6(a) perfectly. Here  $n$  is the subband index. The expected locations of the valleys, associated with the time-dependent Bragg reflection, are given by the expression

$$X_N = \frac{1}{2} + \left(n + \frac{1}{2}\right) \frac{\mu}{\mu - k_{\pm}^2}, \quad (4.12)$$

and thus they should be at  $X_N = 1.03, 2.1, 3.14$  for  $T_{\rightarrow}(X_N)$  and at  $X_N = 1.15, 2.4, 3.73$  for  $T_{\leftarrow}(X_N)$ . Again, they match the valley locations in Fig. 4.6(a) remarkably.

Besides, in Fig. 4.6(a) there are two additional valley structures, indicated by arrows, at which  $T_{\rightarrow}(X_N)$  and  $T_{\leftarrow}(X_N)$  fall one on the top of the other. These structures do not contribute to the pumped current, and they are due to the time-dependent Bragg reflection from the second order Fourier component of  $V(x, t)$ . The second Fourier component of  $V(x, t)$  is in the form of a standing wave, given by  $\cos(2Kx)[\cos\Omega t + \sin\Omega t]$ . Both of the additional valleys all appearing in  $T_{\rightarrow}(X_N)$  and  $T_{\leftarrow}(X_N)$  can be understood from the fact that more resonant coupling conditions come into play for the case of standing wave. The

resonant coupling conditions are  $\varepsilon_k = \varepsilon_{k\pm 2K} \pm \Omega$  and  $\varepsilon_k = \varepsilon_{k\pm 2K} \mp \Omega$ . As such, the valley locations are given by the expression

$$X_N = \frac{1}{2} \left[ 1 + \frac{\mu}{\mu - \varepsilon_{\pm}} \right] \quad (4.13)$$

for  $n = 0$  and  $\varepsilon_{\pm} = [K(1 \mp \Omega/(2K)^2)]^2$ . Accordingly, these  $2K$  time-dependent Bragg reflection valley locations are expected to be at 1.36 and 1.73, which coincide with the two additional valleys, indicated by arrows, in Fig. 4.6(a). We note, in passing, that contributions from higher Fourier components of  $V(x, t)$  diminishes gradually.

The  $X_N$  dependence of the pumped current for the case in Fig. 4.6(a) is represented by the solid curve in Fig. 4.6(b). The peaks have flat tops because the valleys in the corresponding  $T_{\rightarrow}(X_N)$ ,  $T_{\leftarrow}(X_N)$  are well separated. The pumped current for  $\Omega = 0.0014$ , the same frequency as in the case of Fig. 4.4(b), is depicted by the dotted curve in Fig. 4.6(b). The peaks are not flat-topped and the magnitudes are much smaller because the transmission valleys overlap. For comparison, we also present the case when parameter values differ slightly from that of the optimal choice. As is shown by the dashed curve in Fig. 4.6(b), where all parameters are the same as those for the solid curve except that  $\alpha$  is changed from  $1/4$  to  $1/5$ , the basic pumped current peaks, shown also in the solid curve, remain intact. This demonstrates the robustness of the QCP against the deviation in values of the configuration parameters from the optimal choice.

Interestingly, there are two additional features in the dashed curve of Fig. 4.6(b), namely, an additional pumped current peak at  $X_N = 1.5$ , and an increase in the peak value for the pumped current near  $X_N = 3.5$ . Both of these features found to arise from the second Fourier component of  $V(x, t)$  is supported by the outcome of our analysis performed upon the Fourier component of  $V(x, t)$ . This method of

analysis has thus far been successful in providing us insights on the pumping characteristics presented in this work. The  $m$ -th Fourier component of  $V(x, t)$ , apart from a constant factor, is given by the form

$$\begin{aligned} \mathcal{V}_m = \{ & [\cos(m\pi\alpha) - \sin(m\pi\alpha)] \cos[mKx' - \Omega t - \pi/4] \\ & + [\cos(m\pi\alpha) + \sin(m\pi\alpha)] \cos[mKx' + \Omega t + \pi/4]\}, \end{aligned} \quad (4.14)$$

where  $x' = x - \delta x/2$ .  $\mathcal{V}_m$  consists, in general, of waves propagating in both left and right directions. But when  $\alpha = 1/4$ , as we have discussed before,  $\mathcal{V}_1$  becomes a pure left-going wave and  $\mathcal{V}_2$  becomes a pure standing wave. The case of  $\alpha = 1/5$ , however, have both  $\mathcal{V}_1$  and  $\mathcal{V}_2$  consisting of waves in opposite propagation directions. Therefore, in contrast with the  $\alpha = 1/4$  result, additional contributions from the  $2K$  Bragg reflection are expected for the case  $\alpha = 1/5$ . This additional contribution should peak at the mid-point between two transmission valleys for the  $2K$  Bragg reflections, and the expression for  $X_N$  is given by

$$X_N = \frac{1}{2} + \left(n + \frac{1}{2}\right) \frac{\mu}{\mu - \varepsilon_M}, \quad (4.15)$$

where  $\varepsilon_M = K^2 + (\Omega/2K)^2$ . For the case of the dashed curve in Fig. 4.6(b), the values of  $X_N = 1.54$  and  $3.6$  are shown to match the locations of the additional features nicely. Finally, we can extract information of the sensitivity of the pumped current characteristics to  $\alpha$  by looking at the coefficients of the left-going and right-going waves in  $\mathcal{V}_m$ . For  $\alpha = 1/5$ , the coefficients of  $\mathcal{V}_1$  for, respectively, the right-going and the left-going waves are  $0.22$  and  $1.4$ . This shows that  $\mathcal{V}_1$  is still dominated by the left-going wave and thus explains the tiny modifications to the pumped current peaks at  $X_N = 1.1$ , and  $2.3$ . But for  $\mathcal{V}_2$ , the coefficients for, respectively, the right-going and the left-going waves are  $-0.95$  and  $1.57$ . This shows that  $\mathcal{V}_2$  deviates quite significantly from that of

a standing wave and so explains that the additional peaks from the  $2K$  Bragg reflections are quite large.

#### 4.4 Summary

It is interesting to note in passing that our proposal of the FGA pair configuration is different, in three aspects, from the voltage lead pattern proposed earlier by Niu. [2] First of all, the pumping mechanisms to which the configurations are catering are different. It is the mechanism of translating the Wannier functions in a given Bloch band in Ref. 2, while it is the mechanism of the time-dependent Bragg reflection in this work. The former mechanism is adiabatic by nature but the latter mechanism is shown, in this work, to hold in both the instantaneous and non-instantaneous regimes.

Second, the configurations are different in the number of sets of voltage leads invoked. A third set of voltage leads was instituted by Niu to fix the Fermi energy at the middle of the *instantaneous energy gap* in order to maintain the adiabaticity of the pumping. Since our interest here is on the general pumping characteristics, including, in particular, their dependence on the Fermi energy, it suffices us to consider a simpler configuration---the FGA pair configuration. Third, the number of voltage lead expected and needed in a voltage lead set is different. Our results demonstrate the resonant nature of the time-dependent Bragg reflection and the robust pumping characteristic---requiring only a FGA pair with small  $N$ . Hence the FGA pair configuration proposed in this work should be more accessible experimentally.

In conclusion, we have proposed a finger-gate array pair configuration for the generation of quantum charge pumping. Detail pumping characteristics have been

analyzed; the robustness of the time-dependent Bragg reflection in QCP has been demonstrated; the pumping mechanism has been understood.





## References

- [1] D. J. Thouless, “Quantization of particle transport,” *Phys. Rev. B*, vol. 27, pp. 6083–6087, May 1983.
- [2] Q. Niu, “Towards a quantum pump of electric charges,” *Phys. Rev. Lett.*, vol. 64, pp. 1812–1815, Apr. 1990.
- [3] F. Hekking and Yu. V. Nazarov, “Pauli pump for electrons,” *Phys. Rev. B*, vol. 44, pp. 9110–9113, Oct. 1991.
- [4] M. Switkes, C. M. Marcus, K. Campman, and A. C. Gossard, “An Adiabatic Quantum Electron Pump,” *Science*, vol. 283, pp. 1905–1908, Mar. 1999.
- [5] P. W. Brouwer, “Scattering approach to parametric pumping,” *Phys. Rev. B*, vol. 58, pp. R10135–R10138, Oct. 1998.
- [6] I. L. Aleiner and A. V. Andreev, “Adiabatic Charge Pumping in Almost Open Dots,” *Phys. Rev. Lett.*, vol. 81, pp. 1286–1289, Aug. 1998.
- [7] F. Zhou, B. Spivak, and B. Altshuler, “Mesoscopic Mechanism of Adiabatic Charge Transport,” *Phys. Rev. Lett.*, vol. 82, pp. 608–611, Jan. 1999.
- [8] O. Entin-Wohlman and A. Aharony, “Quantized adiabatic charge pumping and resonant transmission,” *Phys. Rev. B*, vol. 66, pp. 035329–035334, Jan. 2002.
- [9] Y. Wei, J. Wang, and H. Guo, “Resonance-assisted parametric electron pump,” *Phys. Rev. B*, vol. 62, pp. 9947–9950, Oct. 2000.
- [10] C. S. Tang and C. S. Chu, “Nonadiabatic quantum pumping in mesoscopic nanostructures,” *Solid State Commun.*, vol. 120, pp. 353–357, Nov. 2001.
- [11] S. Zhu and Z. D. Wang, “Charge pumping in a quantum wire driven by a series of local time-periodic potentials,” *Phys. Rev. B*, vol. 65, pp. 155313–155316, Mar. 2002.
- [12] M. L. Polianski and P. W. Brouwer, “Pumped current and voltage for an adiabatic quantum pump,” *Phys. Rev. B*, vol. 64, pp. 75304–75309, Jan. 2001.

- [13] J. E. Avron, A. Elgart, G. M. Graf, and L. Sadun, “Optimal Quantum Pumps,” *Phys. Rev. Lett.*, vol. 87, pp. 236601–236603, Nov. 2001.
- [14] B. Wang, and J. Wang, “Heat current in a parametric quantum pump,” *Phys. Rev. B*, vol. 66, pp. 125310–125313, Sep. 2002.
- [15] M. Moskalets and M. Büttiker, “Effect of inelastic scattering on parametric pumping,” *Phys. Rev. B*, vol. 64, pp. 201305(R)–201308(R), Oct. 2001.
- [16] M. Moskalets and M. Büttiker, “Dissipation and noise in adiabatic quantum pumps,” *Phys. Rev. B*, vol. 66, pp. 035306–035314, Jul. 2002.
- [17] S. W. Kim, “Magnetic-field inversion symmetry in quantum pumps with discrete symmetries under the Floquet formalism,” *Phys. Rev. B*, vol. 68, pp. 085312–085317, Aug. 2003; *ibid.* “Floquet scattering in parametric electron pumps,” vol. 66, pp. 235304–235309, Dec. 2002.
- [18] M. Moskalets and M. Büttiker, “Hidden quantum pump effects in quantum coherent rings,” *Phys. Rev. B*, vol. 68, pp. 075303–075310, Aug. 2003.
- [19] M. Moskalets and M. Büttiker, “Quantum pumping: Coherent rings versus open conductors,” *Phys. Rev. B*, vol. 68, pp. 161311(R)–161314(R), Oct. 2003.
- [20] D. Cohen, “Quantum pumping and dissipation: From closed to open systems,” *Phys. Rev. B*, vol. 68, pp. 201303(R)–201306(R), Nov. 2003.
- [21] P. Sharma and C. Chamon, “Adiabatic charge and spin transport in interacting quantum wires,” *Phys. Rev. B*, vol. 68, pp. 035321–035337, Jul. 2003
- [22] J. M. Shilton, V. I. Talyanskii, M. Pepper, D. A. Ritchie, J. E. F. Frost, C. J. B. Ford, C. G. Smith, and G. A. C. Jones, “High-frequency single-electron transport in a quasi-one-dimensional GaAs channel induced by surface acoustic waves,” *J. Phys.: Condens. Matter*, vol. 8, pp. L531–L540, Sep. 1996; J. M. Shilton, D. R. Mace, V. I. Talyanskii, Yu. Galperin, M. Y. Simmons, M. Pepper, and D. A.

- Ritchie, “On the acoustoelectric current in a one-dimensional channel,” *J. Phys.: Condens. Matter*, vol. 8, pp. L337–L344, Jun. 1996
- [23] V. I. Talyanskii, J. M. Shilton, M. Pepper, C. G. Smith, C. J. B. Ford, E. H. Linfield, D. A. Ritchie, and G. A. C. Jones, “Single-electron transport in a one-dimensional channel by high-frequency surface acoustic waves,” *Phys. Rev. B*, vol. 56, pp. 15180–15184, Dec. 1997.
- [24] Y. Levinson, O. Entin-Wohlman, P. Wölfle, “Acoustoelectric Current and Pumping in a Ballistic Quantum Point Contact,” *Phys. Rev. Lett.*, vol. 85, pp. 634–637, Jul. 2000.
- [25] O. Entin-Wohlman, Y. Levinson, P. Wölfle, “Acoustoelectric pumping through a ballistic point contact in the presence of magnetic fields,” *Phys. Rev. B*, vol. 64, pp. 195308–195314, Oct. 2001.
- [26] A. Aharony and O. Entin-Wohlman, “Quantized pumped charge due to surface acoustic waves in a one-dimensional channel,” *Phys. Rev. B*, vol. 65, pp. 241401(R)–241404(R), May 2002.
- [27] C. S. Tang, Y. H. Tan and C. S. Chu, “Transport spectroscopy in a time-modulated open quantum dot,” *Phys. Rev. B*, vol. 67, pp. 205324-205330, May 2003.
- [28] P. F. Bagwell and R. K. Lake, “Resonances in transmission through an oscillating barrier,” in *Phys. Rev. B*, vol. 46, pp. 15329- 15336, Dec.1992.
- [29] M. Büttiker and M. Moskalets, “Scattering Theory of Dynamic Electrical Transport,” *Lecture Notes in Physics*, vol. 690, pp. 33-44, Sep. 2006.

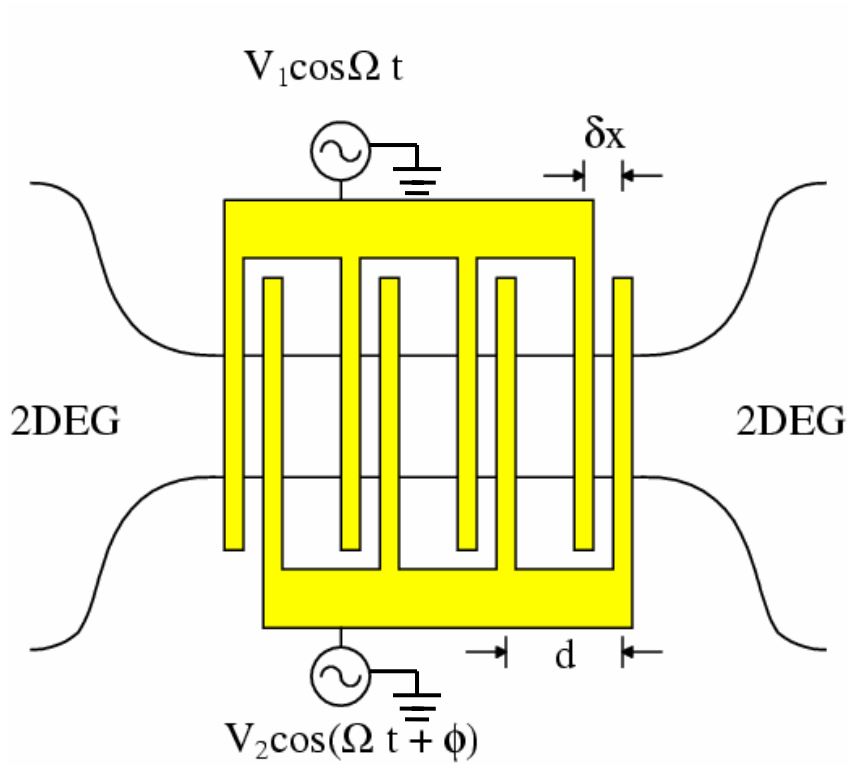


Fig. 4.1 Top view of the proposed system structure is for the case of FG number  $N = 4$ . A FGA pair locates on top of a narrow channel.  $\tilde{V}_i$  denotes the amplitude of the potential energy and  $\phi$  is the phase difference.

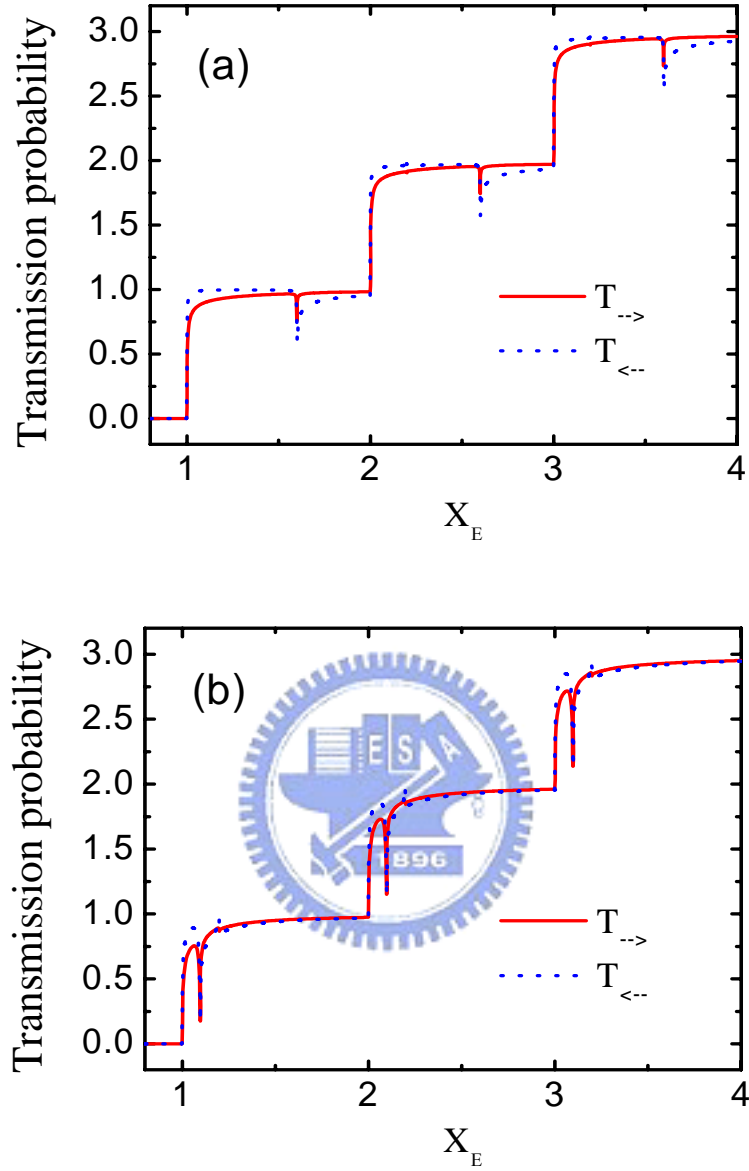


Fig. 4.2 Total current transmission probability versus  $X_E$  for a pair of FG at (a)  $\Omega = 0.6 \Delta \epsilon$  and (b)  $\Omega = 0.1 \Delta \epsilon$ . The transmissions of the right-going (left-going) electrons are represented by the solid (dotted) curve. The subband level spacing is  $\Delta \epsilon$ . Parameters  $\alpha = 1/4$  and  $\phi = \pi/2$  are chosen to meet the optimal condition.

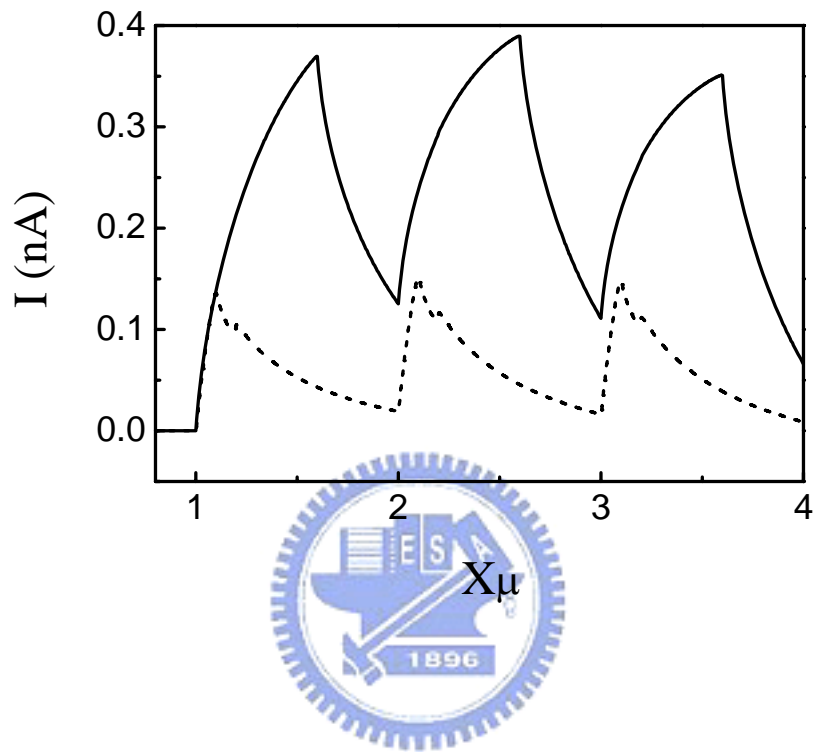


Fig. 4.3 The pumped currents versus  $X_\mu$  with the same parameters used in Fig. 4.2. The solid and dashed curves correspond, respectively, to  $\Omega = 0.6\Delta\varepsilon$  and  $\Omega = 0.1\Delta\varepsilon$ .

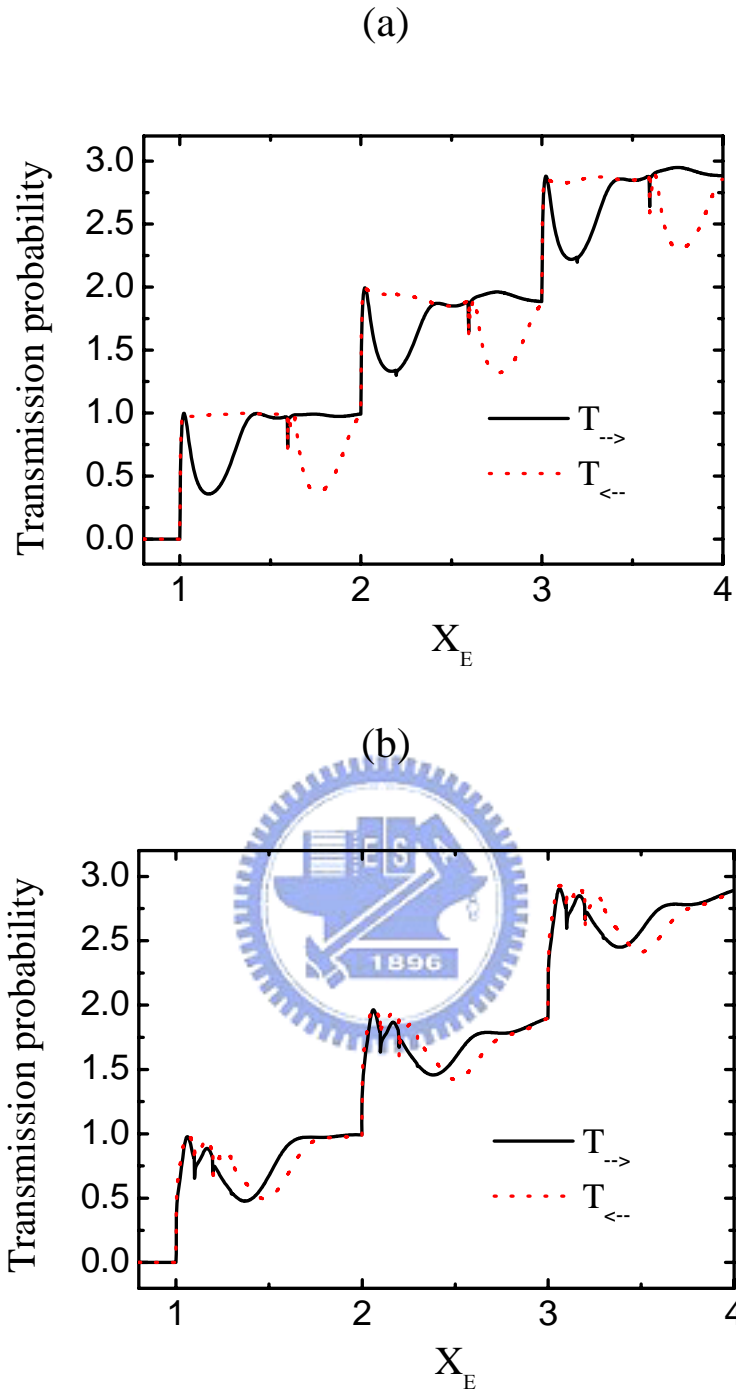


Fig. 4.4 Total current transmission probability versus  $X_E$  for  $N = 4$  at (a)  $\Omega = 0.6\Delta\varepsilon$  and (b)  $\Omega = 0.1\Delta\varepsilon$ . The transmissions of the right-going (left-going) electrons are represented by the solid (dotted) curve. The parameters  $\alpha = 1/4$  and  $\phi = \pi/2$ .

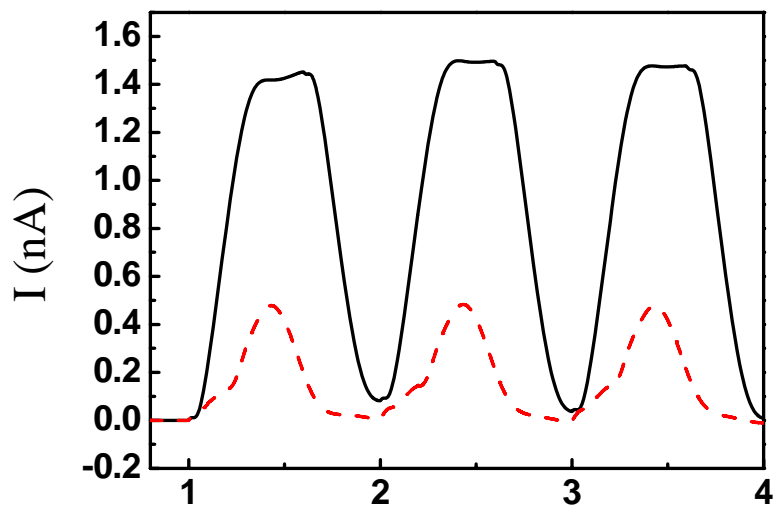


Fig. 4.5 Pumped current versus  $X_\mu$ . The choices of parameters are the same as in Fig. 4.4. The solid and dashed curves correspond, respectively, to  $\Omega = 0.6\Delta\varepsilon$  and  $\Omega = 0.1\Delta\varepsilon$ .



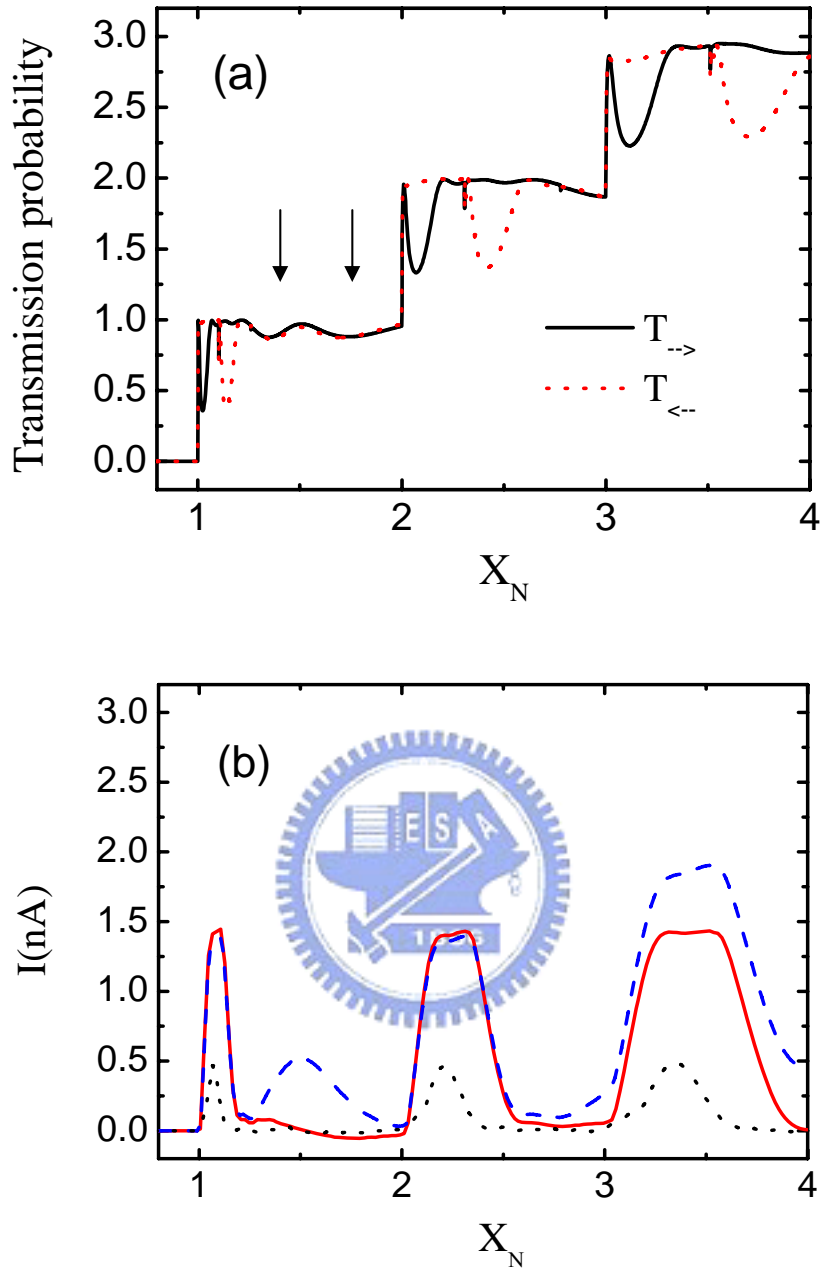


Fig. 4.6 The dependence on subband level spacing  $\Delta\varepsilon$  of (a) the total current transmission probability, and (b) the pumped current. The abscissa is depicted by Eq. (4.10) where  $\mu = 0.049$  and  $N = 4$ . Pumping frequency  $\Omega = 0.0084$  in all curves except for the dotted curve in (b), where  $\Omega = 0.0014$ . Parameters  $\phi = \pi/2$  and  $\alpha = 1/4$  for all curves except for the dashed curve in (b), where  $\alpha = 1/5$ . In (a), the solid (dashed) curve is for  $T_{\rightarrow}(X_N)$  [ $T_{\leftarrow}(X_N)$ ], and

contributions from the second Fourier component of  $V(x,t)$  are indicated by arrows.



## Chapter 5

### Conclusions

For the conclusion of this thesis, firstly in chapter 2, we investigate the visibility of the current and shot-noise correlations of electrical analogs of the optical Mach-Zehnder interferometer and the Hanbury Brown Twiss interferometer. The electrical analogs are discussed in conductors subject to high magnetic fields where electron motion is along edge states. The transport quantities are modulated with the help of an Aharonov-Bohm flux. We discuss the conductance (current) visibility and shot noise visibility as a function of temperature and applied voltage. Dephasing is introduced with the help of fictitious voltage probes. Comparison of these two interferometers is of interest since the Mach-Zehnder interferometer is an amplitude (single-particle) interferometer whereas the Hanbury Brown Twiss interferometer is an intensity (two-particle) interferometer. A direct comparison is only possible for the shot noise of the two interferometers. We find that the visibility of shot noise correlations of the Hanbury Brown Twiss interferometer as function of temperature, voltage or dephasing, is qualitatively similar to the visibility of the first harmonic of the shot noise correlation of the Mach-Zehnder interferometer. In contrast, the second harmonic of the shot noise visibility of the Mach-Zehnder interferometer decreases much more rapidly with increasing temperature, voltage or dephasing rate.

In chapter 3, we have investigated the characteristics of the currents in a pump-driven fermionic Mach-Zehnder interferometer. The system is implemented in a

conductor in the quantum Hall regime, with the two interferometer arms enclosing an Aharonov-Bohm flux  $\Phi$ . Two quantum point contacts with transparency modulated periodically in time drive the current and act as beam-splitters. The current has a flux dependent part  $I^{(\Phi)}$  as well as a flux independent part  $I^{(0)}$ . Both current parts show oscillations as a function of frequency on the two scales determined by the lengths of the interferometer arms. In the non-adiabatic, high frequency regime  $I^{(\Phi)}$  oscillates with a constant amplitude while the amplitude of the oscillations of  $I^{(0)}$  increases linearly with frequency. The flux independent part  $I^{(0)}$  is insensitive to temperature while the flux dependent part  $I^{(\Phi)}$  is exponentially suppressed with increasing temperature. We also find that for low amplitude, adiabatic pumping rectification effects are absent for semitransparent beam-splitters. Inelastic dephasing is introduced by coupling one of the interferometer arms to a voltage probe. For a long charge relaxation time of the voltage probe, giving a constant probe potential,  $I^{(\Phi)}$  and the part of  $I^{(0)}$  flowing in the arm connected to the probe are suppressed with increased coupling to the probe. For a short relaxation time, with the potential of the probe adjusting instantaneously to give zero time dependent current at the probe, only  $I^{(\Phi)}$  is suppressed by the coupling to the probe.

Otherwise, the characteristics of the shot noise in pump-driven electronic Mach-Zehnder interferometers have been also investigated. The low temperature and the low frequency conditions are explored. Both conditions reveal the noiseless regimes and the  $\cos\phi$  variations of the shot noise in the adiabatic consideration. Contrary to the low temperature condition, at the low frequency condition increasing

the temperature causes the remove of the noiseless regimes and the suppression of the  $\cos\phi$  variations. Furthermore, at the low temperature condition the shot noises show the negative growing with small oscillations as the frequency increases, while currents change up and down around zero. The different frequency dependent behaviors lead to some noise regimes with the vanishing currents.

In chapter 4, we study the pumping effects, in both the instantaneous and non-instantaneous regimes, of a pair of *finite* finger-gate array (FGA) on a narrow channel. Connection between the pumping characteristics and associated mechanisms is established. The pumping potential is generated by ac biasing the FGA pair. For a pair of finger gates (FG's) ( $N = 1$ ), the pumping mechanism is due to the photon-assisted interferences. For a pair of FGA with pair number  $N > 2$ , the dominant pumping mechanism becomes that of the time-dependent Bragg reflection. The contribution of the time-dependent Bragg reflection to the pumping is enabled by breaking the symmetry in the electron transmission when the pumping potential is of a predominant propagating type. This propagating wave condition can be achieved both by an appropriate choice of the FGA pair configuration and by the monitoring of a phase difference  $\phi$  between the ac biased in the FGA pair. The robustness of such a pumping mechanism is demonstrated by considering a FGA pair with only pair number  $N = 4$ .

## 簡 歷

姓名： 鐘淑維 (Shu-Wei Vanessa Chung)

出生日期：民國六十六年十一月二十二日(1977.11.22)

住址：407 台中市西屯區西屯路二段 255 號 3F-3

學歷：

國立交通大學電子物理學系  
民國 85 年 9 月 - 民國 89 年 6 月

國立交通大學材料科學與工程所碩士班  
民國 89 年 9 月 - 民國 90 年 6 月

國立交通大學電子工程研究所博士班  
民國 90 年 9 月 - 民國 96 年 3 月



經歷：

研究生海外學習計畫(千里馬計畫)於瑞士 M. Büttiker  
教授之實驗室

民國 93 年 5 月-民國 94 年 5 月

論文題目：

量子幫浦效應、雜訊分析及電子失相行為於低維度傳輸系統

Topics in the Low Dimensional Systems: Effects of Quantum  
Pumping, Shot Noise and Decoherence

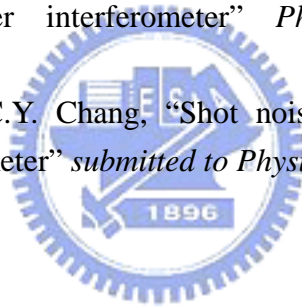
# Publication List

## International conference:

1. **S.-W. V. Chung** and C. Y. Chang, “Electronic Mach-Zehnder interferometers with quantum pump effects”, *the 4<sup>th</sup> international nanotech symposium & exhibition in Korea*, pp. 920-923, 2006.

## International Journals:

1. **S.W. Chung**, C.S. Tang, C.S. Chu and C.Y. Chang, “Finger-gate array quantum pumps: pumping characteristics and mechanisms” *Phys. Rev. B*, vol. 70, pp. 085315-085321, 2004.
2. **V. S.-W. Chung**, P. Samuelsson and M. Büttiker, “Visibility of current and shot noise in electrical Mach-Zehnder and Hanbury Brown Twiss interferometers” *Phys. Rev. B*, vol. 72, pp. 125320-125332, 2005.
3. **S.-W. V. Chung**, M. Moskalets and P. Samuelsson, “Quantum pump driven fermionic Mach-Zehnder interferometer” *Phys. Rev. B*, vol. 75, pp. 115332-115341, 2007.
4. **S.-W. V. Chung** and C.Y. Chang, “Shot noise in a quantum pump driven Mach-Zehnder interferometer” *submitted to Physica E*.



# Publication List

(畢業點數: 7點)

## International conference:

1. (1點會議論文集) **S.-W. V. Chung** and C. Y. Chang, “Electronic Mach-Zehnder interferometers with quantum pump effects”, *the 4<sup>th</sup> international nanotech symposium & exhibition in Korea*, pp. 920-923, 2006.

## International Journals:

1. (3點長文) **S.W. Chung**, C.S. Tang, C.S. Chu and C.Y. Chang, “Finger-gate array quantum pumps: pumping characteristics and mechanisms” *Phys. Rev. B*, vol. 70, pp. 085315-085321, 2004.
2. (3點長文) **V. S.-W. Chung**, P. Samuelsson and M. Büttiker, “Visibility of current and shot noise in electrical Mach-Zehnder and Hanbury Brown Twiss interferometers” *Phys. Rev. B*, vol. 72, pp. 125320-125332, 2005.
3. **S.-W. V. Chung**, M. Moskalets and P. Samuelsson, “Quantum pump driven fermionic Mach-Zehnder interferometer” *Phys. Rev. B*, vol. 75, pp. 115332-115341, 2007.
4. **S.-W. V. Chung** and C.Y. Chang, “Shot noise in a quantum pump driven Mach-Zehnder interferometer” *submitted to Physica E*.